Effect of an Impervious Core Constructed into a Large Earth Dam on the Quantity of Seepage

Ressol R. Shakir

Civil Engineering Department

College of Engineering

Thi-Qar University

Abstract

Impervious core is used in zoned earth dam to reduce the quantity of seepage through the body of the dam and to relief part of risk of piping and erosion in the downstream side. This paper presents cases study of the effect of core permeability, thickness and location on the flow through large earth dam. Finite element method was used to solve the problem of flow of incompressible fluid which is governed by Laplace equation. A considerable range of shell permeability to core permeability was used. The study has shown that quantity of seepage was reduced as ratio of shell to core permeability increases. The reduction in seepage continues to a limited value of core permeability after which the effect decreases. Doubling the core base thickness reduces the quantity of seepage highly and inclination of core towards upstream side slightly increases the quantity of seepage.

Keywords: Earth dam; Finite element; free surface; core; seepage.

تأثير لب مانع للتسرب منشأ في سد ترابي كبير على كمية النضوح

المستخلص

يستعمل اللب المانع من التسرب في السدود الترابية لتقليل كمية التسرب خلال جسم السد و لإزالة جزء من مشكلة التآكل في الجهة الثانية من السد. يقدم هذا المقال دراسة حالات تأثير نفاذية اللب وسمكه وموقعه على النضوح خلال سد ترابي كبير. تم استخدام طريقة العناصر المحددة لحل مسالة نضوح مائع غير قابل للانضغاط والذي يحكم بمعادلة لابلاس. تم استخدام مدى واسع من نفاذية جوانب السد إلى قيم نفاذية اللب. أوضحت الدراسة تناقص كمية التسرب كلما ازدادت نسبة نفاذية جوانب السد الى نفاذية اللب. يستمر التناقص في التسرب الى حد معين من نفاذية اللب بعدها يكون التأثير قليلا. وجد بان مضاعفة سمك اللب يقلل كمية النضوح بشكل كبير كما وجد بان انحراف اللب باتجاه جهة مقدم السد يزيد وبشكل قليل كمية الجريان.

1. Introduction

Excessive seepage forces may cause instability of soil mass in earth dam at the exit or exposed face in a form of piping and heave if they exceed the accepted limit. To eliminate this risk three process should be followed through design stage to control the seepage: preventing piping and heave, reducing seepage and draining the water [1]. Reducing the seepage through dam section may be achieved by using impervious membrane on the upstream or impervious cores. Design of impervious cores may consider several parameters such as thickness, slope, location of core weather it is installed vertically or installed towards upstream side and the permeability of construction materials.

A main requirement of core is that it should provide the necessary degree of imperviousness, and should deformable to withstand differential settlement without cracking. The imperviousness, hydraulic gradient and cracking may be influenced by thickness of core, for example thin cores may associate with high seepage gradient while thick core may associate with low hydraulic gradient [2]. Although the effect of core thickness on some elements of earth dams has been studied by some researchers [3, 4,5, 6], lack of information about the effect of thickness on seepage through earth dam such as free surface, surface seepage and quantity of seepage still keep on.

Free surface was calculated by two methods fixed mesh [7,8]and adaptive mesh [9,10].In the adaptive mesh algorithm, the free surface requires implementation of Darcy's law by finite element and procedure to add-on mesh deformation. Adaptive mesh is simpler more than the fixed mesh [11]. Indicating the location of free surface has a great attention in determining the exit point of flow at the downstream side. Therefore it may be affected by location of the core whether it is constructed vertically or inclined towards upstream side. The researches on this aspect are few and studying the effect of location of core on the quantity of seepage will increase the information on controlling the seepage through the dam.

This research adopts a finite element model to solve the unconfined flow through large earth dam. After verifying the model with available solution for a typical problem, a core with different thickness and location are investigated. The main object of this research is to study the flow through earth dam with different core permeability, core thickness and core location by using finite element method with adaptive mesh method. It also objects to (1) quantify the quantity of seepage and located the free surface; (2) investigate two core locations and (3) study the effect of core permeability on the quantity of seepage.

2. Finite element model

Unconfined flow through earth dam is assumed to be governed by Darcy's law in which the velocity correlated to head between any two points in the flow media

$$v = -k \ \ grad(h) \tag{1}$$

where v is the velocity, k is the permeability, h is the head and pressure. Using conservation of water leads to the following partial differential equation assuming steady state flow

$$div(v) = 0.0 \tag{2}$$

$$k\nabla^2 h = 0.0 \tag{3}$$

The partial differential equation is available in common procedures produced by Smith and Griffiths [10]. The degree of freedom is the pressure which can be implemented through programming the finite element to compute the quantity of seepage and to locate the free surface.

3. Verification the model

The computer program of flow in two dimension (program 7.3) [10]based on finite element method outputs the pressure value, inflow and outflow at every point in the mesh and also locates the free surface. The characteristics of the problem solved herein as an example for verification purposes are a flow through a rectangular dam with 10m height, 5m width, 10mupstream head and 2m downstream head. The media of flow was divided into 50 elements: 10 elements in y direction and 5 elements in x direction. Figure shows the mesh of the verified problem that uses a rectangular quadrilateral element with four nodes.

The computer program results are plotted in a mesh form in which every node represents the pressure head Figure (2). Free surface was represented by a solid line and the numerical solution results obtained by other researchers were also presented. The free surface starts from the top point at the right hand side and ends at a point at extreme left side where head pressure approximately equals 6.5 m. This result approximately agrees with results found in the previous researches [12,8, 13]. In spite of low tail- water height (2 m) the elevation of the exit point of the free surfacewas6.5 m. This value is approximately the same value (6.2 m) obtained by Polubarinova-Kochina [14].

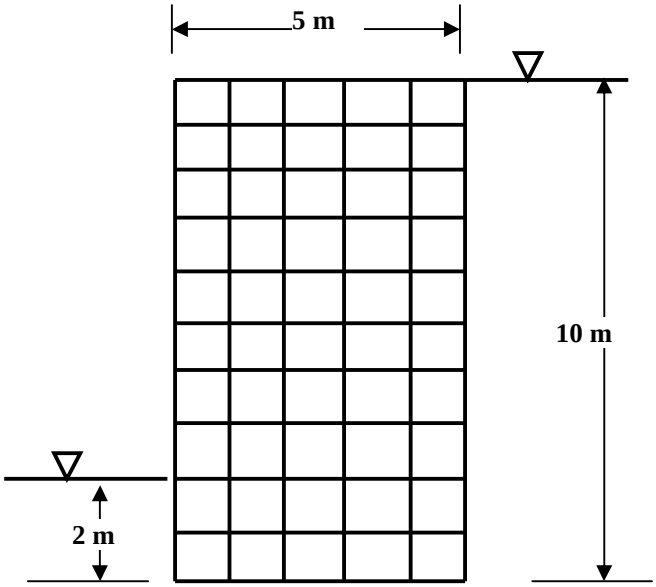

Figure (1). Mesh of the verified problem.

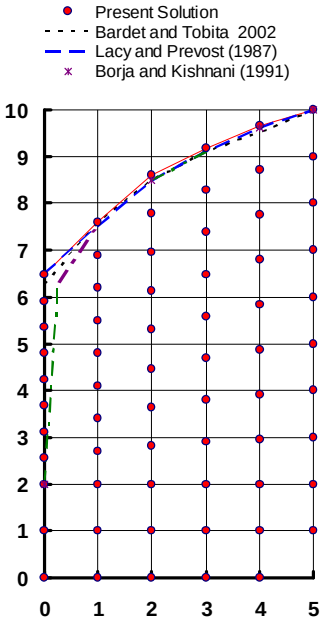

Figure (2).Comparison of free surface in a rectangular dam with the previous solutions.

4. Earth dam problem

The cases study represents free surface flow through earth dam with slopes at the two sides. The base of the dam was 400 m and the crest width was 20 m Figure (3). Upstream pressure head was 100 m and tail-water was changed with each problem. Total elements used to simulate the problem were 400 elements 40 in x direction and 10 in y direction. The shape of element was trapezoid with four nodes. The earth dam consists of shell at the upstream and downstream side and core between them. The results of the flow analysis of the dam are manifested by the permeability property. The dam is homogeneous when the permeability of whole media of dam is the same.

The two core locations studied were vertical core and core inclined towards upstream sides as will be shown in the next sections. The selection of cases was performed according to their practical advantages. For instance, the central core provides the most simple and economical choice and inclination towards upstream or downstream was to give stronger to the dam. In case of defects in the foundation along the axis of the dam, a sloping core type of dam may be indicated. The advantage of a sloping core is that it permits placement of rock fill in the large downstream portion of the dam ahead to the core, which is a major construction advantage[1].

Range of materials may be used for core while the shell has same materials for all cases. The study focused on studying the effect of core permeability. A set of permeability beginning from 0.00002 to 0.001 cm/s was selected representing different materials such as clay. Table (1) shows the values of permeability used in the case study. The ratio of core permeability to shell permeability k/kc is also presented in Table (1). The greatest ratio is one for homogeneous dam and no ratio less than one because it is not acceptable in dam design. For the case of no drainage the core material "Compacted clay and other fine-grained" core materials permeability is less than 0.0001 cm/sec, while clean gravel give permeability greater than 0.1 cm/sec .i.e. rapid draw down. Materials with permeability between 0.0001cm/s and 0.1 cm/s are categorized as semi-pervious material such as sand and sand-gravel mixer [1].

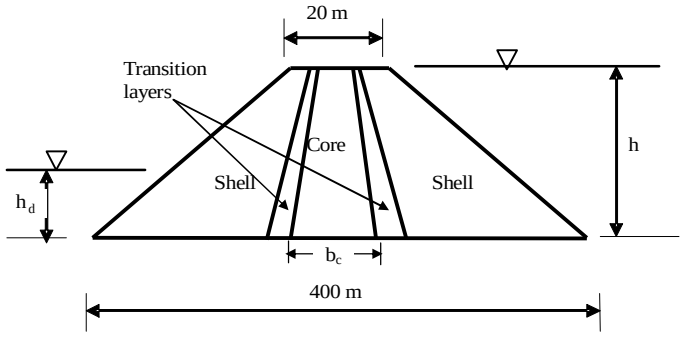

Figure (3).Schematic view of the dam problem (not to scale).

Table (1).Permeability of both shell and core that used in seepage reduction.

Item No.	K (cm/s)	k_c(cm/s)	k/k_c
1	0.001	0.00002	50.00
2	0.001	0.00003	33.33
3	0.001	0.00004	25.00
4	0.001	0.00006	16.67
5	0.001	0.0001	10.00
6	0.001	0.0002	5.00
7	0.001	0.0004	2.50
8	0.001	0.0006	1.67
9	0.001	0.0008	1.25
10	0.001	0.001	1.00

5. Vertical core

This section describes the earth dam problem and presents the discussion and analysis of the computer program results. The problem considered was a two dimensional flow through earth dam with central core. The general characteristics of the problem such as upstream head, crest width, downstream, upstream slop, and core base thickness are the same as aforementioned details. Symbols k and kc represent permeability of shell and permeability of core respectively. h_d, and h represent downstream and upstream head respectively. Two cases of core base thickness(b_c) were used 40m and 80m and the top width of the core was 8 m. The base core thicknesses were 0.4 h and 0.8 h which are commonly used in design of dams. Figure (4) shows the schematic view of the considered problem.

In all figures presented here the quantity of seepage (q) is normalized by both upstream head (h) and shell permeability (k). Figure (5) shows the relationship between normalized quantity of seepage (q/kh) and ratio of shell permeability to core permeability (k/k_c). They were mapped for four values of ratio h_d/h (0.1, 0.2, 0.3 , 0.4). As the ratio of k/k_c increases, q/kh decreases until it reaches 0.05861 $m^3/s/m$ at k/k_c =25 for the case of b_c=80m Table (2). After that the reduction in q/kh is 0.04620 which represents insignificant reduction. It is obviously noticed that k/k_c between 1-25shows high effect on the q/kh for case of b_c=80 m and b_c=40m and insignificant effect on q/kh for k/k_c>25, Figure(5). It also can be noticed that ratio of h_d/h has slight effect on q/kh.

Normalized quantity of seepage (q/kh) for the case of dam with core base thickness b_c= 40 is greater than q/kh for dam with core base thickness b_c=80 m Figure (5). Certainly when the core permeability is similar to shell permeability i.e. ks/k_c=1,the earth dam being homogeneous dam. As the ratio of permeability increases (k/k_c) i.e. the core permeability (k_c) decreases, the difference between the q/kh for the two cases of thickness will be appear clearly.

Figure (6) shows the relation between Q_r^n and k/k_c for four ratios of h_d/h (0.0, 0.1, 0.2, 0.3). Q_r^n is defined as the ratio of difference between q/kh for case of b_c=40 and that for case of b_c=80 to q/kh for case of b_c=40. It is mathematically expressed as follow:

$$Q_r^n\% = \frac{Q^n_{b_c=40} - Q^n_{b_c=80}}{Q^n_{b_c=40}} \times 100 \qquad (4)$$

Q_r^n increases linearly at low ratios of k/k_c ranged between 1 and 5.The curves show low raise in Q_r^n as k/k_c increases more than 5. Maximum Q_r^n is noticed at k/k_c=16.67 and reduction in Q_r^n is noticed at k/k_c>16.67. Maximum Q_r^n was 32% for case of h_d/h=0.0, 30.6 for h_d/h=

0.1, 32.7% for h_d/h= 0.2, and 31.4 for h_d/h= 0.3.Average value of $(Q_r^n)_{max}$ for the four cases of h_d/h was 31.7. Q_r^n at k/k_c=50 was 27% for case of h_d/h=0, 23.5%, for h_d/h= 0.1, 21.6% for h_d/h= 0.2, and 23.3% for h_d/h= 0.3. Average value of $(Q_r^n)_{max}$ for the four cases of h_d/h was 23.9. This means that thickness of core base has a great effect on the quantity of seepage depending essentially on the core permeability.

In addition to previous presented results, lines of seepage, free surface and surface of seepage were mapped for every case. Because of space limitation three meshes of computed free surface were presented Figure (7a,b,c). Free surface represents the upper stream line in flow domain where the pressure is atmospheric pressure. The free surface separates the saturated soil from that no flow occurs. The determination of locus of free surface is important since it can locate the surface of seepage i.e. the point of flow through downstream side. High variability in pressure is found through the core and the free surface fall down directly after the downstream face of core in the earth dam.

Referring again to Figure (7a)which shows the computed free surface for earth dam without core, one may see long surface of seepage (a). Changing the point of flow in the downstream sideis required to reduce the danger of erosion which may occur in this region. Thus the benefit of using core and the importance of study such problems are clear. From computed free surface Figure (7b and c) where b_c=40 m it is shown that surface of seepage (a)reduces from about 139 m for homogeneous dam to about 31.5 m and reduces to about 25.6 m for b_c=80 m. Figure (7c) shows the computed free surface for case of earth dam with core base b_c=40.0, Q= 6.34×10^{-3}m3/s/m and for b_c=80 m Q= 4.62×10-3 m^3/s/m.

Figure (8) shows the relation between normalized surface seepage (a/h) against (k/k_c) for case of b_c=40 and b_c=80 m. Normalized seepage surface, a/h, is equal 1.5 at k/k_c=1 which represents the seepage through homogeneous earth dam. This value is greater than that calculated from charts which have been presented by Gil boy [3]or from the equations that have been presented by Stello [6]. The difference may be attributed to some factors have not been included in charts or equations such as crest width, upstream head and large dam. The length of surface seepage, a/h, for the case of earth dam with core base b_c=40at k/k_c=33 is reduced to 0.25 for h_d/h=0.0. It is slightly greater than that for case of bc=80 m where a/h=0.2. It may be concluded that increasing the width of core is insignificant with respect to reducing surface of seepage. The toe drain size that can be used to drain the seepage depends on the determination of point of flow through downstream side. Using core with b_c=40 gives a=31.5 m at k/k_c=50 and a=52 m at k/k_c=16.6. Using core with b_c=80 m gives a= 25.6 m at

k/k_c =50 and a=41.5 m at k/k_c=16.6. The cost may determine increasing width of core or increasing the size of toe drain.

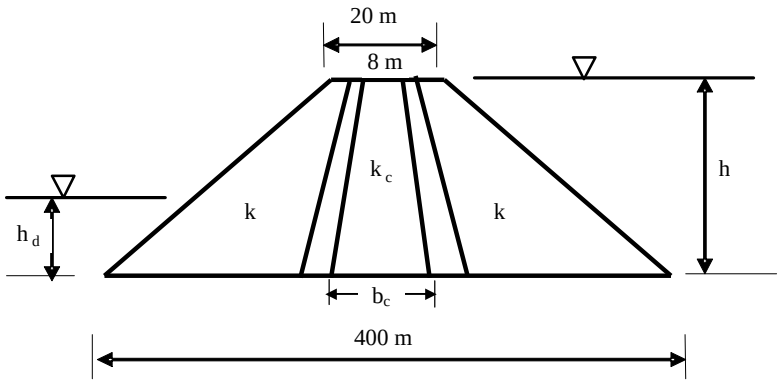

Figure (4). Schematic view of the earth dam problem.

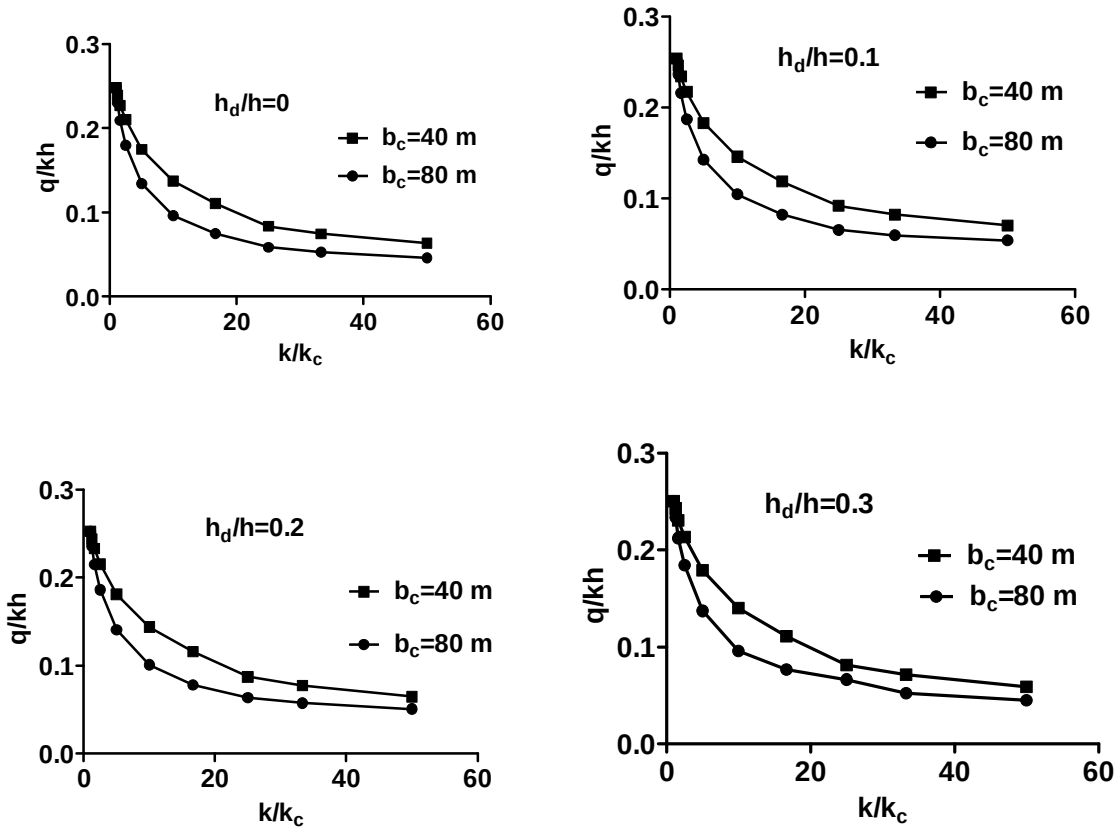

Figure (5).Normalized quantity of seepage (q/kh) versus normalized permeability (k/k_c) for ratio of downstream head to upstream head (h_d/h) 0,0.2, 0.2, 0.3.

Table (2). q/kh for vertical core with b_c=80 m and b_c=40 m.

k/k_c	q/kh							
	h_d/h=0.1		h_d/h=0.2		h_d/h=0.3		h_d/h=0.4	
	b_c=40 m	b_c=80 m	b_c=40 m	b_c=80 m	b_c=40 m	b_c=80 m	b_c=40 m	b_c=80 m
1	0.24840	0.24840	0.25370	0.25320	0.25250	0.25220	0.25080	0.25060
16.7	0.11030	0.07493	0.11860	0.08235	0.11570	0.07785	0.11100	0.07673
25	0.08358	0.05861	0.09186	0.06574	0.08706	0.06352	0.08147	0.06654
50	0.06343	0.04620	0.07039	0.05383	0.06458	0.05064	0.05904	0.04531

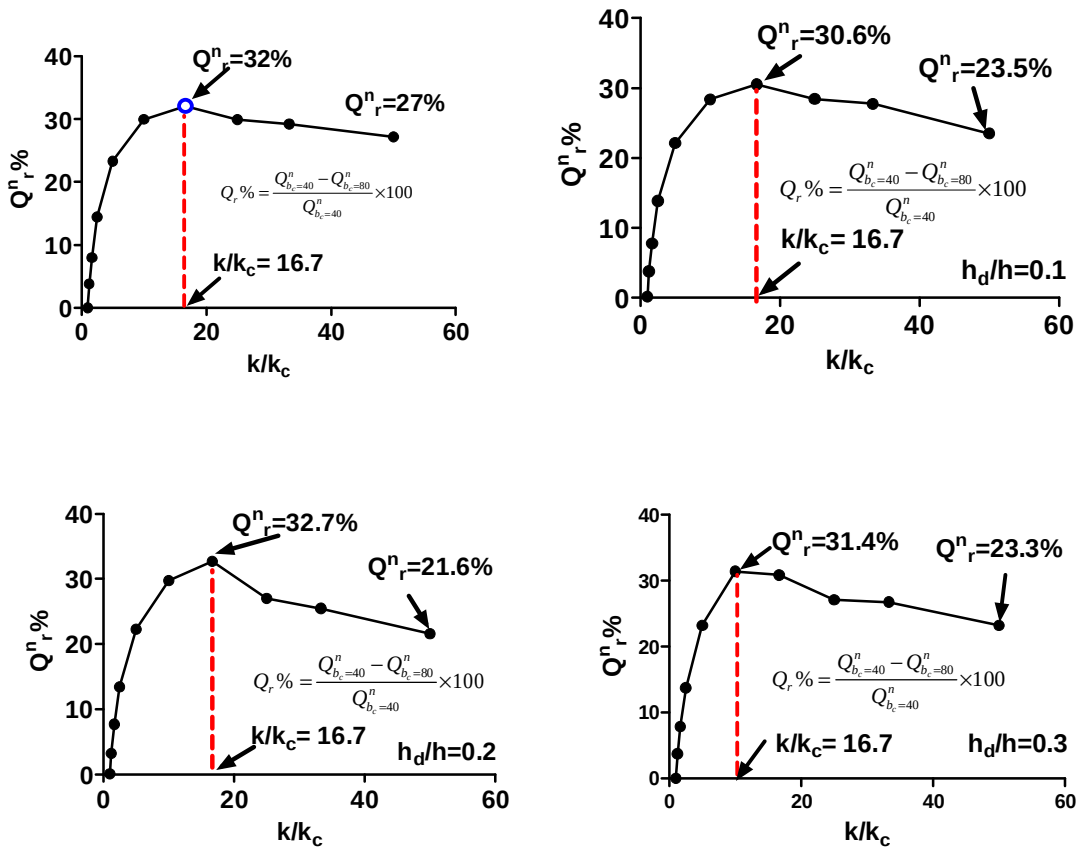

Figure (6). Relation between quantity reduction of seepage (Q_r%) versus normalized permeability (k/k_c) for downstream head ratio (h_d/h) 0,0.2, 0.2, 0.3.

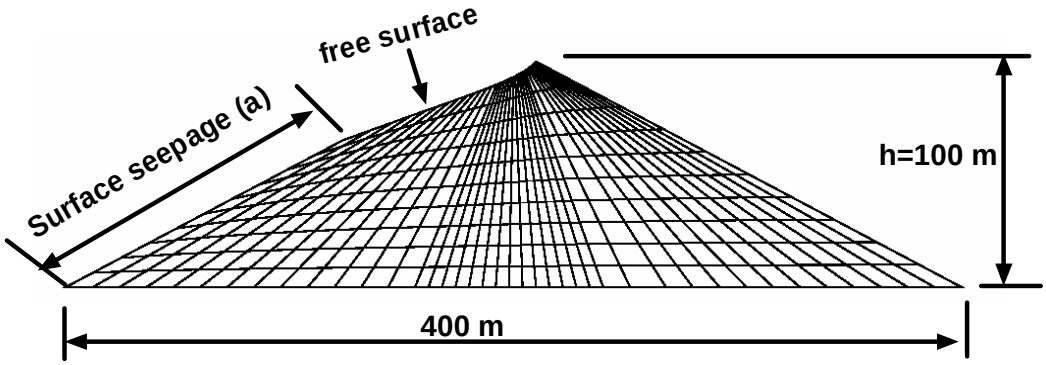

Figure (7a).Computed free surface for case of $k/k_c=1$. Q=0.02484 m^3/s, $h_d/h=0$. $b_c=40$.

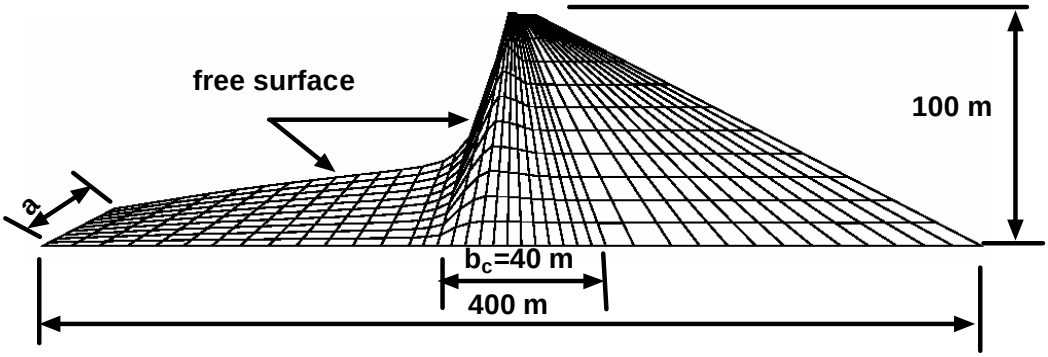

Figure (7b).Computed free surface for case of $k/k_c=50$. Q=6.34E-03 m^3/s, $h_d/h=0$.$b_c=40$m.

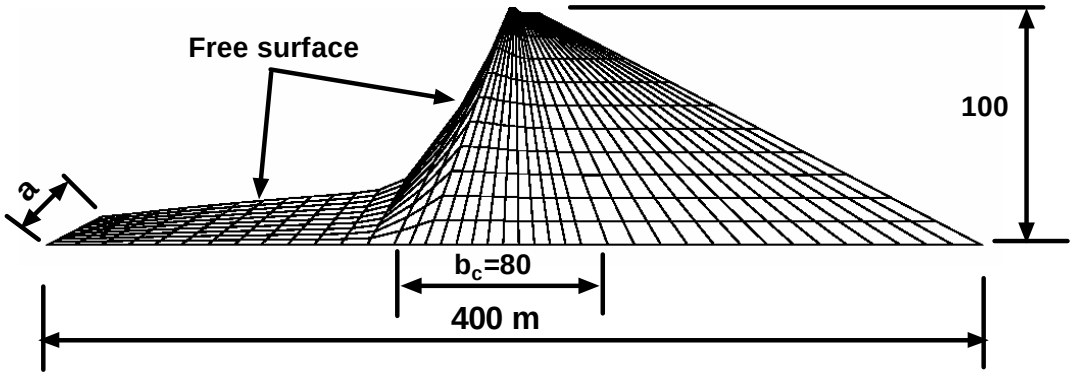

Figure (7c).Computed free surface for case of $k/k_c=50$. Q=4.62E-03m^3/s, $h_d/h=0$. $b_c=80$.

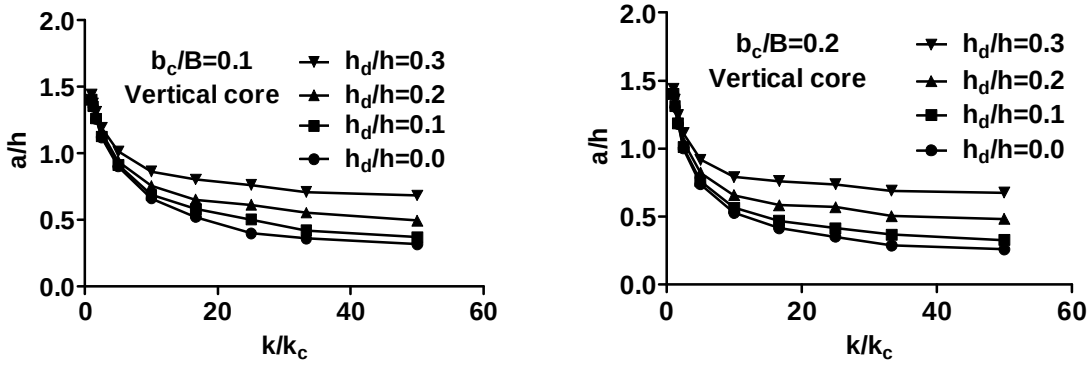

Figure (8).Normalized surface of seepage (a/h) versus normalized permeability (k/k_c) for two core base b_c=40 m, b_c=80 m for earth dam with vertical core.

6. Core inclined towards upstream side

The second application was an example of earth dam constructed with core inclined to the upstream side. Figure (9)shows a sketch demonstrates the problem of earth dam. Crest width was 20m and the base of dam was 400m. Symbol (h) refers to upstream head and symbol (h_d) refers to downstream head. The vertical core in the previous example was replaced by core inclined towards upstream side.

The relationships between normalized quantity of seepage (q/kh) and ratio of shell permeability to core permeability (k/k_c)are presented for h_d/h=0.0, 0.1, 0.2, and 0.3 Figure (10). As the ratio of k/k_c increases i.e. core permeability ,k_c , decreases, normalized quantity of seepage (q/kh) decreases but it fairly decreases when k/k_c being greater than 25. q/kh was 0.25 for all cases of h_d/h=0, 0.1, 0.2 and 0.3 at k/k_c=1 which represents case of homogeneous dam without any core. It was also noticed that q/kh equals 0.08 at k/k_c equal to 25. The object of using impervious core was achieved at k/k_c=25 and no need to use more impervious core since insignificant reduction in q/kh was obtained. The reduction in normalized quantity of seepage was 100 (0.25-0.08)/0.25=68% (Table 3).In addition to that it is obvious that h_d/h has insignificant effect on the q/kh at k/kc greater than 25 Figure (10).

Normalized quantity of seepage (q/kh) for the case of dam with core base b_c=40 m is greater than (q/kh) when b_c equals 80 m Figure (10). As the ratio of permeability increases i.e. The core permeability decreases the difference between the quantities of seepage for the two cases of thickness will be clear. The relation between q/kh at b_c=40 and the q/kh at bc=80 is mapped against the k/k_c Figure(11). Maximum difference between q/kh for case of b_c=40 and b_c=80 was at k/k_c=25, for cases of h_d/h=0 and h_d/h =0.1. For case of water-tail

ratio $h_d/h=0.2$ and $h_d/h=0.3$, maximum Q^n_r at $k/k_c=16.67$ was 44% and it was 41% for both cases of $h_d/h=0.2$ and $0.3.Q^n_r$ is reduced to about 35% as an average at $k/k_c=50\%$. The thickness has an effect at $k/k_c=16.67$ more than other ratios. Core base thickness b_c has an effect on the seepage in case of core inclined towards upstream greater than that of vertical core. For instance average $Q^n_r)_{max.}=43\%$ for case of core inclined towards upstream side and average $Q^n_r)_{max}=31\%$ for case of vertical core.

Figure 12a shows the computed free surface for dam without core. The surface seepage (a) is long and quantity of seepage is $Q=2.41\times10^{-2}m^3/s$. Using vertical core or inclined core reduces both the quantity of seepage and the surface seepage length Figure (12b, c). For case of $b_c=80$ m, quantity of seepage decreases more than previous case ($Q=4.54\times10^{-3}m^3/s$)and also show significance reduction in surface seepage Figure (12c). Figure (13) shows the effect of core on the length of surface seepage (a). It is clear that surface seepage line decreases as thickness of the core increases. Although using core materials with low permeability decrease the surface seepage line, the reduction is insignificant at $k/k_c>33$. Using core with $b_c=40$ m give a=40.9m at $k/k_c=50$ and a=72.4m at $k/k_c=16.6$. Using a core with $b_c=80$ m gives a= 27.2m at $k/k_c=50$ m and a=42.4m at $k/k_c=16.6$. The case of core base $b_c=40$ m gives greater value of (a) compared to case of the vertical core.

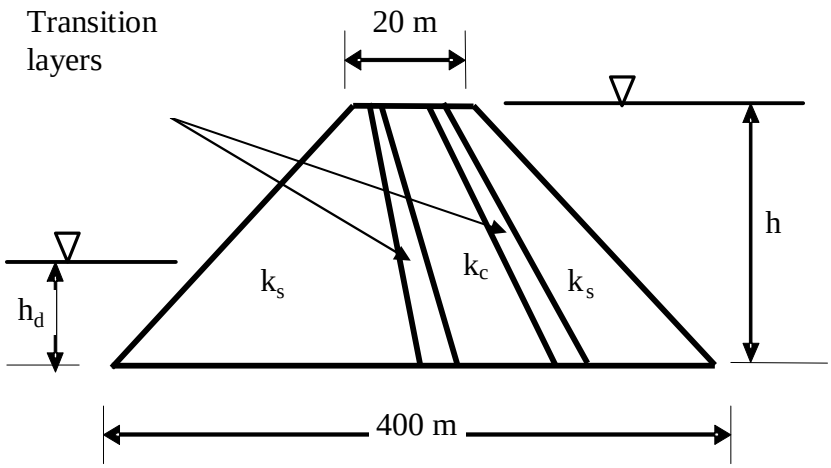

Figure (9). Sketch of dam with core inclined core to the upstream side.

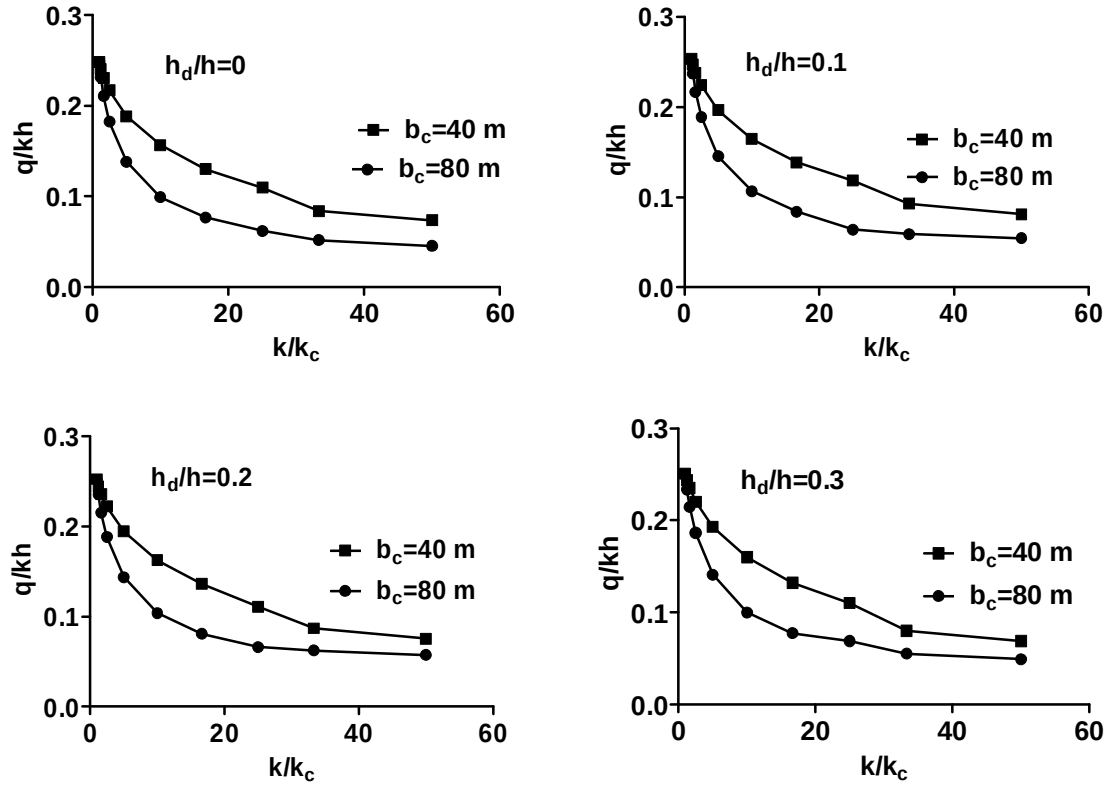

Figure (10) . Relation between normalized quantity of seepage (q/kh) versus normalized permeability (k/k_c) for downstream head (h_d/h) 0,0.2, 0.2, 0.3. (core inclined towards upstream side).

Table (3). Percent of reduction in q/kh for different k/k_c and b_c and for dam with vertical core and dam with inclined core.

	$(Q_{k/kc=1} - Q_{k/kc}) / Q_{k/kc=1}$ (Vertical Core)									
	h_d/h=0		0.1		0.2		0.3		Average	
k/k_c	b_c =40	b_c =80	b_c =40	b_c =80	b_c =40	b_c =80	b_c =40	b_c=80	b_c =40	b_c =80
16	69.83	55.60	67.48	53.25	69.13	54.18	69.38	55.74	68.95	54.69
25	74.46	76.41	72.25	74.04	74.42	74.81	76.46	73.44	74.39	74.67
50	81.40	74.46	78.74	72.25	79.91	74.42	81.91	76.46	80.49	74.40
$(Q_{k/kc=1} - Q_{k/kc}) / Q_{k/kc=1}$(Inclined Core)										
16	69.09	47.53	66.68	45.31	67.88	46.041	68.92	47.27	68.14	46.54
25	55.89	75.11	53.31	74.56	56.05	73.65	56.04	72.41	55.32	73.93
50	81.74	70.39	78.39	67.94	77.09	70.08	80.30	72.44	79.38	70.21

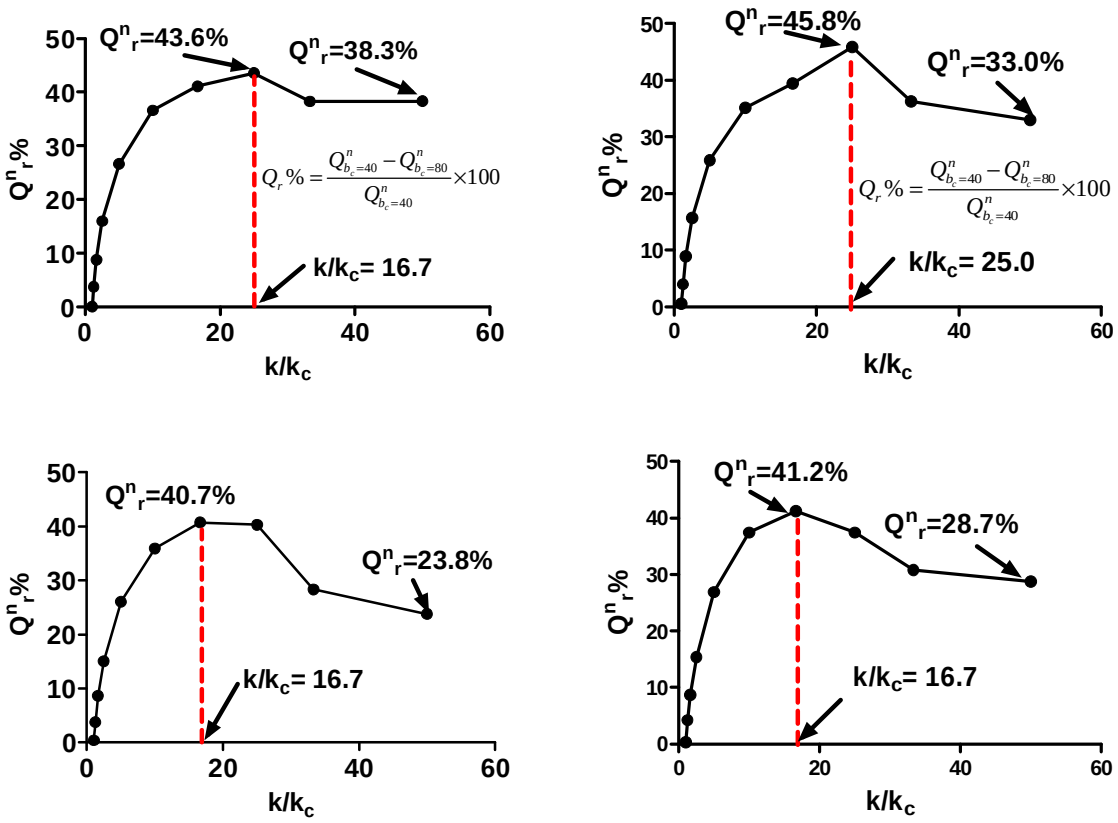

Figure (11). Relation between quantity reduction of seepage (Q_r%) versus normalized permeability (k/k_c) for downstream head ratio (h_d/h) 0,0.2, 0.2, 0.3. (core towards upstream side).

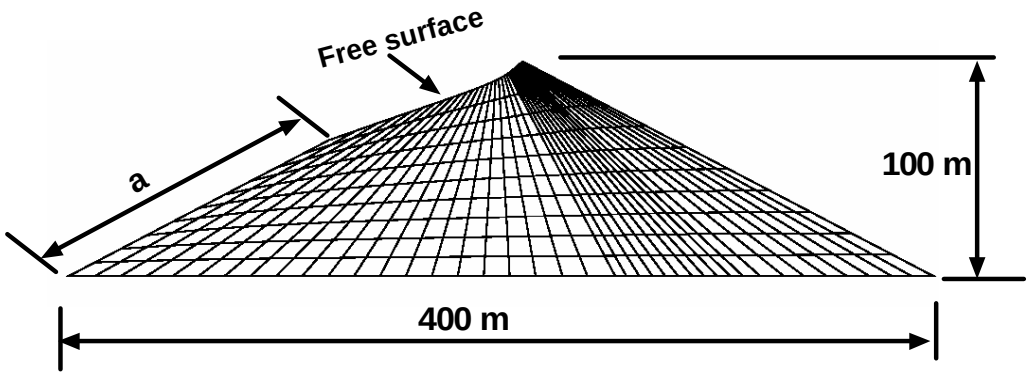

Figure (12a). Computed free surface for case of k/k_c=1.25. Q=2.41E-02m^3/s, h_d/h=0. b_c=40m.

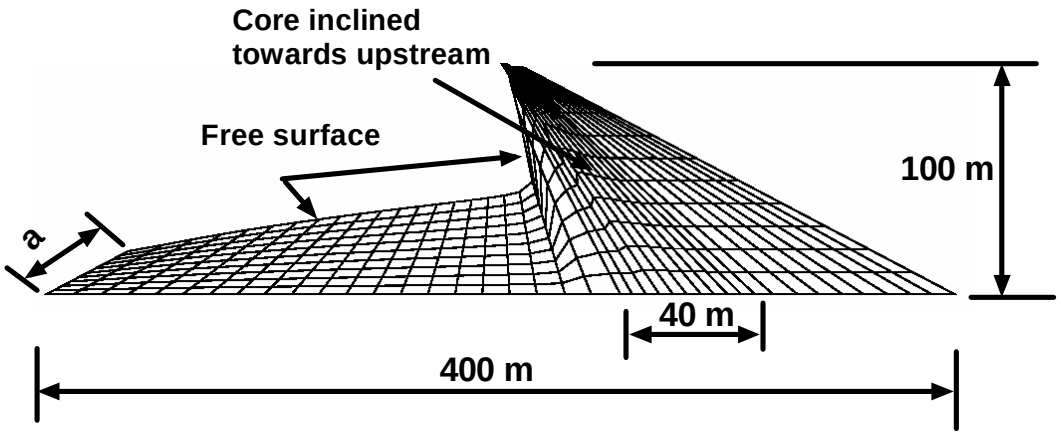

Figure (12b).Computed free surface for case of k/k_c=50. Q=1.91E-04 m^3/s, h_d/h=0.b_c=40m.

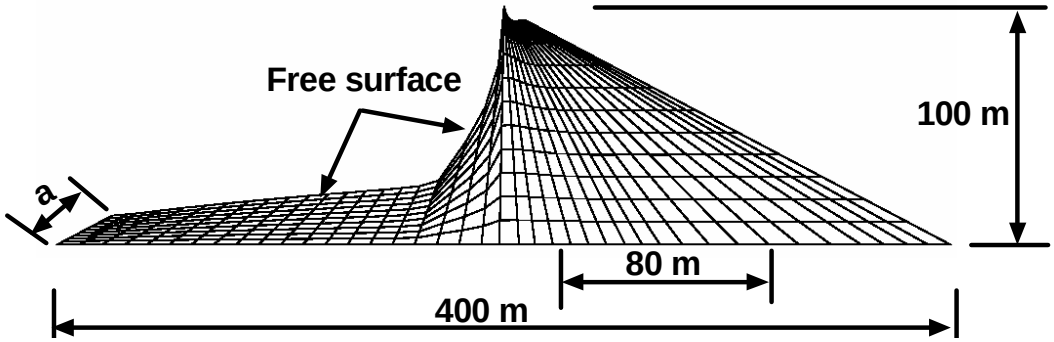

Figure (12c).Computed free surface for case of k/k_c=50. Q=4.54E-03m^3/s, h_d/h=0.b_c=80.

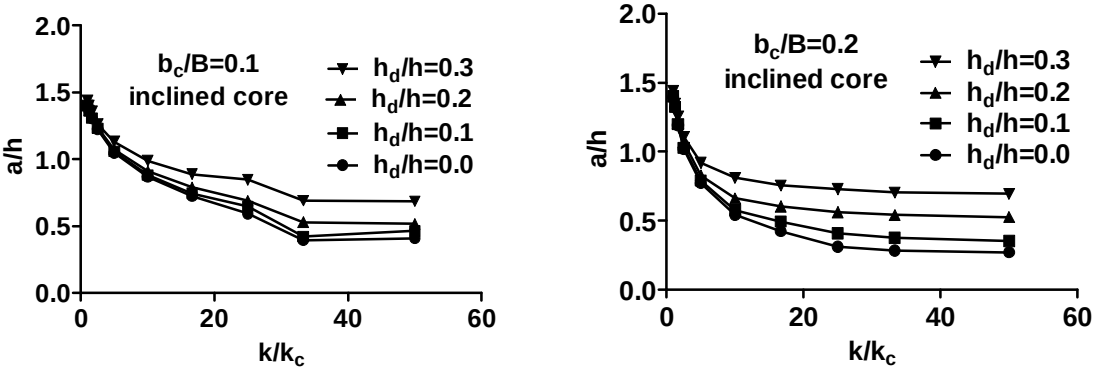

Figure (13).Normalized surface of seepage (a/h) versus normalized permeability (k/k_c) for two core base b_c=40 m, b_c=80 m, for earth dam with core inclined towards upstream side.

7. Conclusions

Finite element method was used to solve the Laplace equation and to locate the free surface. Verifying the results of the computer program of flow in two dimensional (p 7.3) [10]with available methods gives a good agreement. Two cases of core were studied: a vertical core and a core inclined towards the upstream side. The study demonstrated that the quantity of seepage reduces as core with low permeability is used. It was found that using vertical core with core base thickness, b_c=40m, and with permeability 6% of shell permeability decreases the normalized quantity of seepage (q/kh) to 0.45 that obtained from flow through homogeneous dam and using vertical core with permeability 2% i.e. k/k_c=50 of shell permeability decreases the normalized quantity of seepage (q/kh) to 0.25 that obtained for homogeneous dam.

The core base thickness also affects the quantity of seepage. It was found that doubling the base width decreases the quantity of seepage to about 68-76 %.The location of the cores lightly influences the quantity of seepage. It was found that using core inclined towards upstream increases the quantity of seepage 13%.

8. References

[1] Sharma H. D. ,1992, "Embankment Dam." Published by Raju Primlani for Oxford and IBH publishing.

[2] Maksimoric M. ,1973, "Optimum Position of Central Clay Core of a Rock Fill Dam in Seepage and Hydraulic Fracture." th ICOLD, Madride, Vol 3, Q, 42, R-44.

[3] Gilboy G., 1933, "Hydraulic Fill Dams." Proc., Intern, Comm, Large Dams. Stockholm.

[4] Goharnejad H., Noury M., Noorzad A., Shamsaie A. and Goharnejad A., (2010). "The Effect of Clay Blanket Thickness to Prevent Seepage in Dam Reservoir." Res. J. Environ. Sciences, 4: 558-565.

[5] Shehata, A.K., 2006, "Design of Downstream Blanket for Overflow Spillway Founded On Complex Formations." J. Applied Sci. Res., 2: 1217-1227.

[6] Stello, M. W. ,1987, "Seepage Chart for Homogeneous and Zoned Embankments." ASCE Journal, Vol, 107, No.Gt5, MAY pp.996~1012, 1987.

[7] Bathe K. J., and Khoshgoftaar M. R. ,1979, "Finite Element Free Surface Seepage Analysis Without Mesh Iteration." International Journal for Numerical and AnalyticalMethods in Geomechanics, 3:13–22.

[8] Lacy S. J., and Prevost J. H. ,1987, "Flow Through Porous Media: A Procedure for Locating the Free Surface" International Journal for Numerical and Analytical Methods in Geomechanics , 11:585–601.

[9] Cividini A., and Gioda G. ,1990, "On the Variable Mesh Finite Element Analysis of Unconfined Seepage Problems." Geotechnique, 40(3), 523–526.
[10] Smith and Griffiths ,1998, "Programming the Finite Element Method." John Wiley& Sons Canada; 3rd Edition (January 1998).
[11] Fenton, G.A. and Griffiths, D.V. ,1996, "Statistics of Free Surface Flow Through Stochastic Earthdam " , ASCE J. Geotech. Eng., **122**(6), 427–436.
[12] Bardet J. P., and Tobita T. ,2002, "A Practical Method for Solving Free Surface Seepage Problems." Comp. Geotechn., 29, 451–475.
[13] Borja R. I., Kishnani S. S. ,1991, "On the Solution of Elliptic Free-Boundary Problems Via Newton's Method." Computer Methods in Applied Mechanics and Engineering, 88:341–61.
[14] Polubarinova-Kochina, P. Ya., 1952, "Theory of the Motion of Ground Water" Gostekhizdat, Moscow.

9.Nomenclature

List of symbols and variables

Symbol or variable	definition
A	Surface seepage
b_c	Core width
k	Permeability
kc	Permeability of core
h	Upstream head
Q	Quantity of seepage
hd	Downstream head
Q^n	q/kh
$Q^n_{bc = 40}$	q/kh for case of core width = 40 m
$Q^n_{bc = 80}$	q/kh for case of core width = 80 m
$Q_r^n\%$	$Q_r^n\% = \frac{Q^n_{b_c=40} - Q^n_{b_c=80}}{Q^n_{b_c=40}} \times 1($

New Method of Obtaining a Multilayer Anodized Film on 7075-T6 Al-Alloy Surface

Sámi I.J.AL-Rubaiey

Department of Production Engineering and Metallurgy,

University of Technology, Baghdad.

Abstract

It is well known that the anodized thin layer formed on Al-alloys surface are characterized with porosity of nanometric dimensions whatever acid or alkaline solutions are used. In this study, an attempt was made for the first time to develop a new method for obtaining anodized multilayer film by reinforcing the anodized oxide coating with incorporating nanosized graphite in the layer structure during anodizing process by means of anodizing Al- Alloy type 7075 T-6 in an electrolyte composed of water solution of chromic acid and graphite . This leads to obtain a multilayer anodized film having good thickness and high micro hardness properties. Nanosized particles of graphite have been formed into anodic oxide layer. The influence of anodizing process parameters (voltage and current density) on the thickness micro hardness and chemical composition of a multilayer oxide film are determined.

المستخلص

تتميز طبقة الانودة على سطوح سبائك الألمنيوم بشكل عام بظهور مساميات صغيرة الحجم سواء أجريت عملية الانودة في محاليل حامضية أو محاليل قاعدية .

أجريت في هذا البحث (ولأول مرة) محاولة تطوير طريقة جديدة تتلخص بالحصول على انودة متعدد الطبقات بإدخال جزيئات متناهية الصغر من الكرافيت في طبقات الانودة وذلك بإجراء عملية انودة لسبائك الألمنيوم من نوع 7075-T6 في محلول الكتروليتي يتكون من محلول مائي من حامض الكروميك وجزيئات صغيرة جدا من الكرافيت . أثبتت نتائج البحث تغلغل جزيئات الكرافيت في طبقات الانودة مما أدت إلى زيادة صلادتها وبسمك جيد. كما تضمن البحث حساب تأثيرات متغيرات عملية الانودة من الفولتية والتيار على كل من التركيب الكيميائي وسمك وصلادة طبقات الانودة.

1. Introduction

Anodizing or anodizing is an electrolytic passivation used to increase the thickness of the natural oxide layer on the surface of metals and alloys parts. The process is called anodizing because the object to be anodized is electrically positive part or anode, which is immersed in an electrolytic bath. Direct current is then applied and hydrolysis takes place releasing a high concentration of oxygen in a uniform manner[1,2] .

Anodizing can only be applied to metals and alloys which produces an insulating film under the anodizing conditions. This process is widely used and acceptable for the treatment of aluminum and its alloys. The oxygen reacts with the aluminum anode to form a greatly thickened, hard, and porous film of aluminum oxide[2]. Anodizing process increases corrosion resistance, surface hardness and wear resistance.

Anodizing process for aluminum & its alloys is electrochemical process by which Al or Al alloys are treated electrolytically in bath containing solutions of sulphuric acid, chromic acid or a mixture of sulphuric acid and oxalic acid to produce a uniform oxide coating on the surface. The sulphuric acid processes are most generally used for the production of decorative, protective and hard wear resistant coatings[3]. The chromic acid process is often employed, where a high resistance to corrosion is required with a minimum loss of metal section and the protection is the major consideration. The Military and aircraft assemblies are particular areas for this type of anodizing[4]. The sulphuric acid/oxalic acid solution is an anodizing solution which enables relatively "high temperatures" to be used. The properties of the anodized coating will vary with alloy composition, anodizing process employed and process time. Anodizing process changes the microscopic texture of the surface and changes the crystal structure of the metal near the surface[5]. Anodized aluminum alloys are multi-step process in which the Anodized layer is built up from the base of the film but the acids used for the anodic oxidation processes have a solvent action on the aluminum oxide film. Therefore, porous cell structure is formed; in anodic films which needs to be sealed. Sealing is a process used to close the porosity by treated the anodized articles by immersing them in boiling deionized water, salt solutions or in low pressure steam. The alumina of the anodized layer converts to aluminum monohydroxide $Al_2O_3.H_2O$, which enables to close the porous structure[6-8].

It is well known that the anodized thin layer is formed on the surface of aluminum characterizes with porosity whatever acid or alkaline solutions are used. Anodized oxide films on Al-alloys surface are characterized by relatively arrays of uniform pores of nanometric

dimensions. In this study, an attempt was made for the first time to develop a new method for obtaining anodized multilayer by reinforcing the anodized oxide coating with incorporating nanosized graphite in the layer structure during anodizing process. This leads to obtain a multilayer with good thickness and high micro hardness properties for 7075T6Al-alloys.

2. The Experiment

The samples used were 7075-T6 Al alloy in the form of plates of 3 mm thickness. The anodizing process of Al-Alloys 7075 T-6 was processed by removing all foreign materials from the surface area to be anodized. Abrade areas using a gray abrasive pad until a uniform abraded surface were obtained. Solvent was used to clean the area to be anodized using 5% KOH and a 10 % HNO_3 solutions.

The surfaces prepared were subject to electrolytic oxidation by the direct current method. The electrolysis was conducted in an electrolytic plastic tank of the dimensions: (20 X 20 X 15) cm with round edges. Pipes made of 7075 T-6 Al-alloy was used as the anode with 50 mm length , 81 mm diameter and 3 mm thickness. Table 1 lists the chemical composition for used & standard 7075 T6 Al-alloys. A stainless steel rod of the 1/ 5^{th} of the anode area was used as the cathode. Electrodes were immersed to the depth of 3 cm from the tank bottom. Anodization was carried out in an the electrolytes solution of 10% chromic acid (CrO3) {100 g/ L} with an addition of 0.5% loose hexagonal graphite which grain size are less than 50-53 micron and had high purity of 99.9%.

During the anodizing process, the electrolyte was stirred in one direction with a mechanical stirrer at the constant speed of 150 r.p.m. This stirring speed enabled obtaining a homogeneous graphite suspension throughout the electrolyte volume. Graphitization was conducted during the electrolysis, producing a multilayer achieved by incorporating graphite into oxide structure. The anodizing process was conducted during a constant time period of 1 hr. at the current density of 2 or 3 A/dm^2 and at room temperature.

After completion of the anodizing process, the samples were rinsed for 1 hr. in the distilled water in order to remove remaining electrolyte. The samples, then sealed by immersion into a bath of boiling water to close the pores in a multilayer aluminum oxide. The thickness of all layers was measured with a Fischer's Dualscope thickness gauge. The analysis of the composition of the multilayer was performed using an X- ray diffractometer type a Philips PW3710 by using $\lambda_{Cu-k\alpha}$= 1.54 Å. Microhardness was determined by using a Hanemann micro hardness tester.

Operating conditions that may affect the anodizing process (electrolyte compos ion, voltage and current density) on the anodizing processing time, film thickness and its microhardness are studied in this work.

3. Results and discussion

Figure (1) illustrates the relations between the anodizing voltage and the anodizing time for Al_2O_3 layer and for Al_2O_3 + graphite. The value of anodizing voltage was varying with a growing oxide layer. At the beginning of the process, the voltage increased to a certain maximum value, called critical voltage; next it decreased slightly and having reached a certain minimum, then increased again. The reasons for this phenomenon are processes taking place during the oxide coating's formation[5-8]. The value of voltage was found proportional to the current density.

Table (2) shows that the current density and the electrolyte composition have a direct influence on the layer thickness during the anodizing process. Since anodizing is a balance between the chemical dissolution and the oxide formation processes, in the initial stage of anodizing, the total thickness of the composite coating was slightly decreased under a low current density due to a low deposition rate. It is assumed that the dissolution rate was greater than the deposition rate in this stage. The thickness of the anodic film then increased with the operating time.

Thickness of Al_2O_3 formed at room temperature amounted to 33 µm at current density of 2 A/dm and 45.5 µm at 3A/dm^2, while thickness of Al_2O_3 + graphite a multilayer amounted to 30.5 µm at 2 A/dm^2 current density and 41 µm at 3 A/dm^2. This means that, the thickness of Al_2O_3 were was by 5-10%higher than those of a multilayer, which results from a better access of the electrolyte ions to the oxidized material.

Proper current density for a given application is dependent on the purpose of the coating. The higher the current density, the faster the coating is applied. Too high of a current density, however, resulted in overheating of the work area and soft, thin coatings. On the other hand a low current density needs a long anodizing time.

Table (2) also shows that, microhardness of oxide layer formed on Al alloys depends on the conditions of the anodizing process, decreasing upon increasing the surface porosity. All layers formed in the electrolyte containing graphite have higher microhardness than those formed in the basic electrolyte. The difference in microhardness between the Al_2O_3 coatings and the Al_2O_3 + graphite coatings varies between 150 and 500 MPa respectively, depending

on the current conditions. The layers had higher microhardness during anodizing at current density of 2 A/dm^2 than that at current density of 3 A/dm$^{2.}$ These results imply the filling of the aluminum oxide fibrous structure results in its enhanced hardness. From the difference in size of graphite grains and oxide nanopores it results that the mechanism of obtaining a composite layer consists in simultaneous building in of graphite into the structure of oxide layer during the formation[6].

An examination conducted on the substrate and the anodized layers using XRD reveal the presence of Al and graphite. Figure (2) shows the diffract s of loose graphite belongs to the polytypic 2H. The basic reflex 002, whose value a mounts to 3.367 Aº & the intensity I=100. Figure (3) is dominated by two intense peaks 1.435 Aº belong to the substrate, whereas the reflex 3.361 Aº belongs to graphite , with the number of counts amounting to 116 counts/s, which indicates the largest amount of graphite in the Al_2O_3 layer among the investigated surfaces when the anodizing processes were done at 2 and 3 A/dm^2 respectively.

4. Conclusions

The developed technology enables obtaining a multilayer of aluminum oxide and graphite during one technological process. The largest amount of graphite in the Al_2O_3 layer was obtained at the current density of 3 A/dm^2 Al_2O_3 + graphite a multilayer film having a smaller thickness(30.5 to 41 µm) but higher microhardness (4600 to 5010) , when compared to the film obtaining after anodizing without graphite in the same condition, which have 33-45.5 µm thickness and 4500- 4900 micro hardness.

5. References

[1] Chang C.H., Jeng M.C. , Su C.U. & Chang C.L., " An Investigation of Thermal Sprayed Aluminum/Hard Anodic Composite Coating on Wear and Corrosion Resistant Performance ", Thin Solid Films 517 (2009) 5265–5269.

[2] Lyndon B. Johnson Space Center, May 2003, " Process Specification for the Anodizing of Aluminum Alloys" , PRC-5006 Rev. C. National Aeronautics' and Space Administration (NASA), Houston, Texas.

[3] SIFCO Industries Inc. , 2009,"Anodizing Instruction Manual Section Edition".

[4] Henely V.F.,1982," Anodic Oxidation of Aluminum and Its Alloys" ,Pregamon Press Ltd.

[5] Zhang S., Wang F. , Zhang M. , 2007," Effects of electrolytes on properties of anodic coatings formed on AZ91HP Magnesium alloy", Trans. Nonferrous Met. Soc. China 17 pp.785-788.

[6] Rama K. L. , Sudha P. A. Nitip W. and Sundarajan G. ,February 2007,"Kinetic and Properties of Micro Arc Oxidation Coatings Deposited on Commercial Al- Alloys", Metallurgical and Materials Transactions A370- Vol. 38A, , pp 370-378.

[7] Mikael F. ,Patrik M. ,Peter W.,Nilsson,2007," Method of forming a multilayer structure" United States Patent application title , Origin : Washington , DC US , IPC8 Class : AC25D500 FI, USPC Class: 205223. Date of patent.

[8] Kwanhee L. , Hyuneok S. , Yongjoong C., Janghyuk K. and Jinwoung J.,2007,"Organic electroluminescent device employing multilayered anode" , United States Patent , Patent No. US 7,190,111 B2, Date of patent.

Table (1).The chemical composition of used Al-alloy compared with its standard composition .

Element	Zn	Mg	Cu	Cr	Fe	Si	Mn	Ti	Al
wt% Measured	5.62	2.65	1.3	0.17	0.34	0.085	0.40	0.022	Balance
wt% Standard	5.1-6.1	2.1-2.9	1.2-2.0	0.18-0.35	0.5 Max.	0.4 Max.	0.3 Max.	0.2 Max.	Balance

Table (2).The influence of electrolyte composition & current density on the thickness & micro hardness on an anodized film.

Electrolyte Composition	Current Density(A/dm^2)	Thickness of film (μm)	Micro hardness of film
Without Graphite	2	33	4500
	3	45.5	4900
With Graphite	2	30.5	4600
	3	41	5010

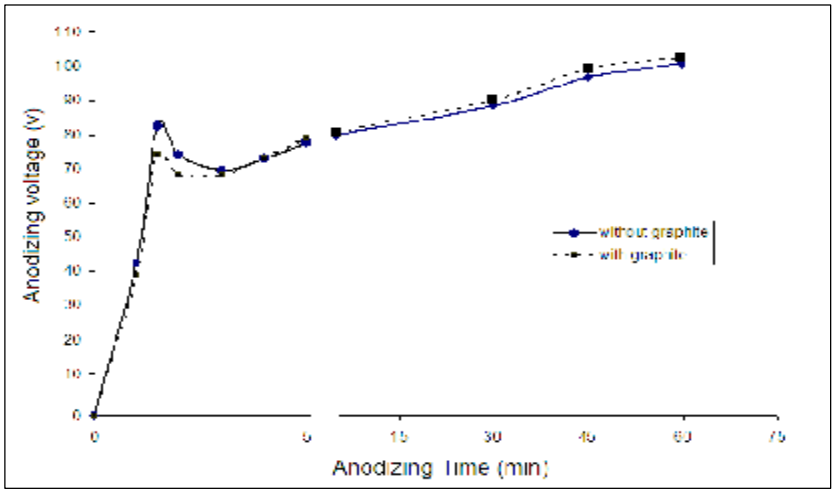

Figure(1- a)

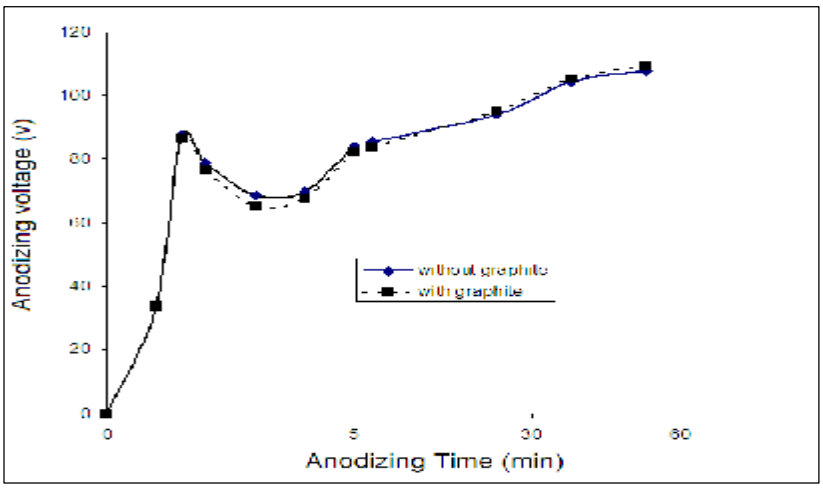

Figure(1- b)

Figure (1). The relations between anodizing voltage and time of process depended on the electrolyte composition. A) at 2 A/dm^2 , b) 3A/dm^2.

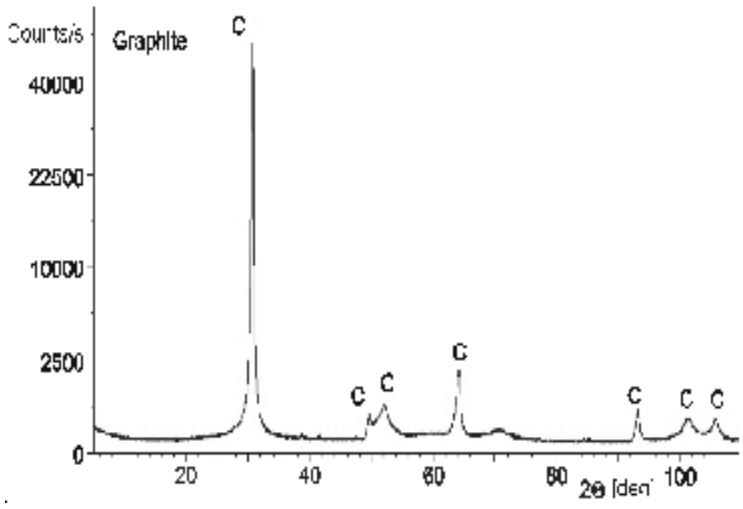

Figure (2) . XRD of graphite.

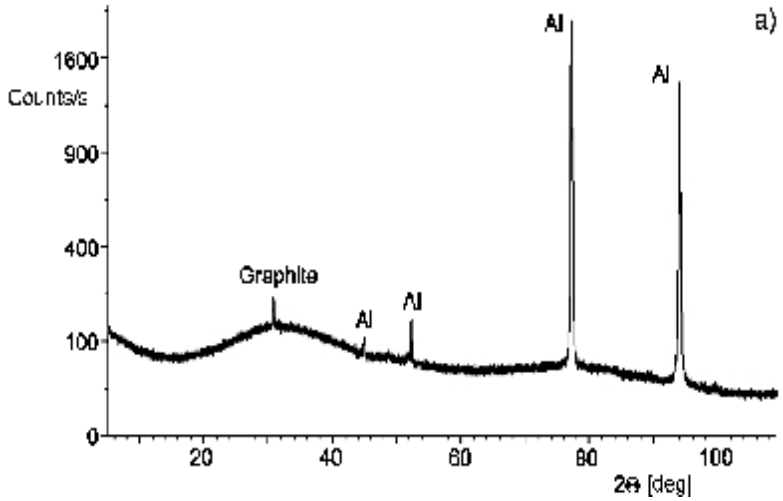

Figure(3-a)

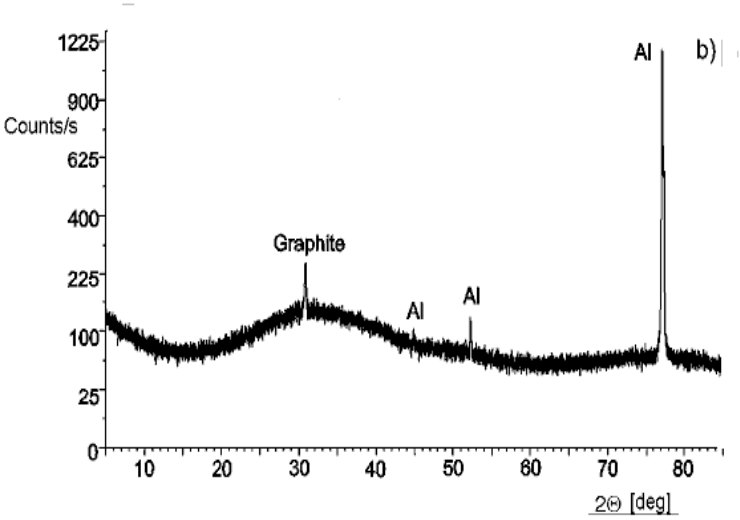

Figure(3-b)

Figure (3) . XRD of the a multilayer film on anodized 7075-T6 Al-alloy. a) at current density 2 A/dm^2,b) at current density 3 A/dm^2.

Analytical Study of Combined Convection Heat Transfer for Flow in a Horizontal Annulus

Ahmed .J. Shkarah
Mechanical Eng. Dept.
College of Engineering
Thi-Qar University

Mushtaq .I. Hasan
Mechanical Eng. Dept.
College of Engineering
Thi-Qar University

Iqbal .K. Eraebee
Civil Eng. Dept.
College of Engineering
Thi-Qar University

Abstract

In this paper a numerical investigation is made to study the axially symmetric, laminar air flow in the entrance region of an annulus by solving the two dimensional governing equations of motion (continuity, momentum & energy) using implicit finite difference method and the Gauss elimination technique. A STAR CCM + program is used. The results obtained for velocity and temperature profile revealed that, the secondary flow created by natural convection have a significant effect on the heat transfer process. A comparison has been made for results which show a good agreement.

Keywords: numerical combined convection; thermally developing flow; finite difference; horizontal annulus.

المستخلص

في هذا البحث تم دراسة عملية انتقال الحرارة خلال انبوبي متحدي المركز في منطقة الدخول عددياً من خلال حل معادلات الحركة (معادلة الاستمرارية ، معادلة الزخم ومعادلة الطاقة) ثنائية الابعاد باستخدام طريقة الفروقات المحددة وطريقة كاوس للحذف باستخدام برنامج (STAR CCM). النتائج التي تم الحصول عليها فيما يخص السرعة ودرجة الحرارة تشير إلى أن الجريان الثانوي المتولد بواسطة الحمل الحر له تأثير مهم على عملية انتقال الحرارة . تم مقارنة النتائج ووجد أن هناك تقارب جيد.

1. Introduction

Convection heat transfer is one of the important heat transfer modes, this process is classified into three distinct types (natural, forced and mixed) convection. The interaction of the natural and forced convection currents can be very complex and difficult because it depends not only on all the parameters determining both forced and free convection relative to

one another but sometimes also on a large number of interacting parameters including the relative direction of the natural and forced convection to each other, the arrangement of the geometry, the velocity profile at annulus entrance and the heating surface boundary conditions [2].Laminar flow combined convection heat transfer in annulus is encountered in a wide variety because of special importance in many industrial engineering applications. The following examples can be cited: heating or cooling of double pipe heat exchangers for viscous liquids, heat exchangers for gas flows [2], cooling of electronic equipment, compact heat exchangers [3], and the cooling core of nuclear reactors [4]. The full understanding of the prevailing velocity and temperature fields, as well as, the pressure drop and heat transfer coefficient, is necessary for the proper design. In addition, to estimate the magnitude of the thermal shock that any one of the preceding systems wall will suffer [5, 6, 7].

Therefore, considering the secondary flow motion continues along the annulus, where as in the uniform inner wall temperature boundary condition, the secondary flow motion develops to a maximum intensity and then diminishes to zero as the temperature difference continuously decreases [8, 9, and 10].

2. Mathematical modeling

2.1. Governing equations

The governing equations of motion are developed on the following assumptions:

Fully developed velocity profile at the entrance of the test section, Steady state laminar and upward flow, Constant wall heat flux at annulus inner tube, constants fluid properties except the density in the buoyancy term and viscous dissipation is neglected.

The following Non dimensional differential equations represent conservation of continuity, momentum (Navier Stockes equations in both axial and radial directions) and energy equation [1] & [4].

Continuity equation:

$$\frac{\partial U}{\partial X} + \frac{V}{R} + \frac{\partial V}{\partial R} = 0 \qquad (1)$$

Momentum equation in axial direction:

$$V\frac{\partial U}{\partial R} + U\frac{\partial U}{\partial X} = -\frac{\partial P}{\partial X} + \frac{1}{Re^{2}}\{G.Cc_{4} + T[Cc_{5} + Cc_{6}T]\}$$
$$+ \frac{1}{Re}\left\{[Cc_{1} + T(Cc_{2} + Cc_{3}T)]\left[\frac{\partial^{2}U}{\partial X^{2}} + \frac{1}{R}\frac{\partial U}{\partial R} + \frac{\partial^{2}U}{\partial R^{2}}\right]\right\} +$$

$$\frac{1}{Re}\left\{[Cc_2 + 2Cc_3 T]\left[2\frac{\partial T}{\partial X}.\frac{\partial U}{\partial X} + \frac{\partial T}{\partial R}\left(\frac{\partial V}{\partial X} + \frac{\partial U}{\partial R}\right)\right]\right\} \quad (2)$$

Momentum equation in radial direction:

$$V\frac{\partial V}{\partial R} + U\frac{\partial V}{\partial X} = -\frac{\partial P}{\partial R} + \frac{1}{Re}[Cc_1 + T(Cc_2 + Cc_3 T)]$$
$$*\left[\frac{\partial^2 V}{\partial X^2} + \frac{1}{R}\frac{\partial V}{\partial R} - \frac{V}{R^2} + \frac{\partial^2 V}{\partial R^2}\right] + \frac{1}{Re}[Cc_2 + 2Cc_3 T]*$$
$$\left\{\left[2\frac{\partial T}{\partial R}.\frac{\partial V}{\partial R} + \frac{\partial T}{\partial X}\left(\frac{\partial V}{\partial X} + \frac{\partial U}{\partial R}\right)\right]\right\} \quad (3)$$

Energy equation:

$$V\frac{\partial T}{\partial R} + U\frac{\partial T}{\partial X} = \frac{1}{Re.Pr}\left(\frac{\partial^2 T}{\partial X^2} + \frac{1}{R}\frac{\partial T}{\partial R} + \frac{\partial^2 T}{\partial R^2}\right) \quad (4)$$

Integral continuity equation:

$$\frac{1}{2}(1 - N^2) = \int_N^1 R\ U\ \P R \quad (5)$$

The viscosity and density variation with temperature are taken to be [11, 12, and 13]:

$$\mu = \mu_i(C_1 + C_2 t - C_3 t^2) \quad (6)$$

$$\rho = \rho_i(C_4 - C_5 t + C_6 t^2) \quad (7)$$

Where C_1, C_2… C6 are constants.

Where the following dimensionless parameters are used:

$$U = \frac{u}{u_i}\ ,\quad V = \frac{v}{u_i}\ ,\quad R = \frac{r}{r_2}\ ,\quad X = \frac{x}{r_2}\ ,\quad p = \frac{p - p_i}{\rho_i u_i^2}\ ,\quad T = GC_5(t - t_i)\ ,\quad N = \frac{r_1}{r_2}$$

Viscosity and density variation, equations (6, 7) in dimensionless form becomes:

$$\mu = \mu_i(Cc_1 + Cc_2 T - Cc_3 T^2) \quad (8)$$

$$\rho = \rho_i(Cc_4 - (Cc_5/G)T + (Cc_6/G)T^2) \quad (9)$$

Where:

$$Cc_1 = C_1 + C_2 t_i - C_3 t_i^2\ ,\quad Cc_2 = (1/G.C_5)(C_2 - 2C_{3i})\ ,\quad Cc_3 = -C_3/G^2.C_5^2$$
$$Cc_4 = (C_4 - C_5 t_i + C_6 t_i^2)\ ,\quad Cc_5 = (2C_6 t_i/C_5) - 1\ ,\quad Cc_6 = C_6/G.C_5^2$$

The boundary conditions in dimensionless form are:

at x = 0 $U = \frac{2}{M}\left(1 - R^2 + B\ln(R)\right), B = \left(\frac{R^2 - 1}{\ln(R)}\right), M = 1 + \frac{1}{N^2} - B$, V = 0, P = 0,T = 0

at R=N (for all x) ,U=0 ,V=0 , $q = k\left(\frac{\partial T}{\partial R}\right)_{R=N}\left(\frac{\nu^2}{r_2^4 C_5 g}\right)$ = constant inner wall heat flux. at R=1 (for all x) ,U=0 ,V=0

3. Numerical solution

In thermal entrance region, the problem of air flow with constant physical properties except the density in buoyancy term is that the energy equation (4) is coupled with the continuity and momentum equations (1 - 3). This leads to say that the problem may be divided into two parts. The equation of energy can be solved to determine the temperature profile after which the continuity equation and momentum equation can be solved to determine the hydrodynamic characteristics of the entry length by using the temperature profile previously obtained from thermal calculations. In the following numerical approximation method, the energy equation will be solved by a direct implicit technique and the hydrodynamic part of the problem will be solved by means of extension to the linearized implicit finite difference technique. A rectangular grid was used with suffices n and m for the axial and radial directions, respectively. A uniform radial spacing was used, but the marching procedure permitted a doubling of the axial step size at arbitrary location and any number of times. Basically, the unknown solution grid point is defined by suffix (n+1,m) and the finite difference method is used to give sets of linear equations for the variable U, V, P and T at the unknown axial position "n+1". Where the product of two unknowns occurs, linearity in the set of equations is achieved by putting one unknown of its value at the previous known step "n".

The boundary conditions in finite difference form become:

1. Entry condition: $U1_{,m} = 2\left(1 - \frac{(m-1)^2}{S^2}\right)$, $V_{1,m} = 0$, $P_{1,m} = 0$, $T_{1,m} = 0$
2. Wall flow condition: $U_{n,M+1} = 0$, $V_{n,M+1} = 0$
3. Wall thermal condition: $T_{n,H+1} = T_{n,H} + \frac{q\, r_1^4\, C_5\, g}{\nu^2\, S\, k}$

4. Computational method and simulation program

In the present theoretical work a computational model is used to study the effect of various parameters such as the heat flux and the Reynolds number on the velocity and temperature profiles and on the heat transfer coefficient in a horizontal annulus. The procedure used to solve the above equation was as follows:

Equation (4) (for temperature) was written for each radial position at first axial step. This gives a set of M-1 equations for the unknowns T's that were solved by Gauss elimination method. Then equations (1 - 3) with integral continuity equation (4) were similarly written and solved for the unknowns U, V and P and these gave equations for U, V, and P unknowns. The known values of T, U, V and P where then used as input data to solve the next axial step.

The introduction of second derivative of velocity and temperature in the axial direction means that three axial positions were involved in the finite difference approximation, two positions (suffices " n-1" and " n") were known and one (suffice "n+1") was unknown. After solution of a given step, the old values at " n" and "n+1" became the new values at "n-1" and "n" respectively and old " n-1" data redundant, and we use STAR CCM+ package for solving problem. Knowing the temperature profiles from the numerical solution of energy, the mixing cup temperature and the local Nusselt number at any cross section can be calculated. The mixing cup temperature at any cross section is defined by:

$$t_m = \frac{\int_{r_1}^{r_2} turdr}{\int_{r_1}^{r_2} urdr} \tag{10}$$

or, in dimensionless form:

$$T_m = \frac{\int_{N}^{1} TURdR}{\int_{N}^{1} URdR} \tag{11}$$

The local Nusselt number at any cross section is defined by:

$$Nu_x = \frac{qD}{k(t_{sx} - t_{mx})} \tag{12}$$

or, in dimensionless form: $$Nu_x = \frac{\left(\frac{\partial T}{\partial R}\right)_{R=N}}{T_{sx} - T_{mx}} \quad (13)$$

Where:

T_{sx}= Dimensionless local inner tube surface temperature.

T_{mx}= Dimensionless local mixing cup temperature.

5. Results and discussion

The numerical study has been conducted mainly to study combined convection heat transfer to assisting airflow in a heated horizontal annulus. The temperature profile, velocity profile, variation of the inner tube surface temperature, and local Nusselt number along the annulus has been investigated.

5.1. Temperature profile

Generally, the variation of the surface temperature along the annulus inner tube may be affected by many parameters such as heat flux, flow velocity, the annulus inclination and the flow entrance situation.

The temperature distribution in the horizontal annulus for selected runs is plotted in Figures (1, 2). From this figure it can be seen at test section entrance the inner tube surface temperature gradually increases up to a specific axial position the temperature reaches a maximum value, after that the inner tube surface temperature decreases at annulus exit. Figure (1) shows the effect of Reynolds number on the inner tube surface temperature for heat flux (241 W/m^2). It is obvious that the increase of Re lead to reduce the inner tube surface temperature, as the heat flux is kept constant. It is necessary to mention that as heat flux increases the inner tube surface temperature increases because the free convection is the dominating factor in the heat transfer process. Figure (2) shows the variation of the surface temperature along the annulus inner tube for different heat flux, for Re=598 and for calming section length equal to 60 cm (L/D_h =13.95). This figure reveals that the inner tube surface temperature increases at annulus entrance reaching a maximum value after which the inner tube surface temperature decreases earlier for higher heat flux. This can be attributed to the development of the thermal boundary layer faster due to buoyancy effect as the heat flux increases for the same Reynolds number.

The inner tube surface temperature variation for the second calming section with length equal to 90 cm (L/D_h =20.93) for Re=598, shows a similar trend as mentioned above for (L/D_h =13.95).

5.2 Velocity profile

The velocity profiles along the horizontal annulus, for Re=1200 and for different rates of heat flux for inner wall, are shown in Figures (3 & 4), from these figures one can see that, for high (Re) number the profiles have revealed a small effect of buoyancy forces in all the profiles and show a profile similar to pure forced convection behavior. The maximum velocity occurs at dimensionless radial distance (R) equal to (17). Figure (5) shows the axial velocity profiles for Re=540 and for heat flux equal to 288 W/m^2. The profile at annulus entrance (x=0) computed and depicted for a fully developed pure forced convection.

5.3. Surface temperature

The inner tube surface temperature distribution along a horizontal annulus is shown in Figures (7 to 9). The inner tube surface temperature distribution along the annulus, for different heat flux and for constant Reynolds numbers (332 and 1128) is shown in Figures (6&7) respectively. The temperature variation for different Reynolds numbers and for constant heat flux (82.778 W/m^2 and 545 W/m^2) is shown in Figures (8&9) respectively. The figures show that the inner tube surface temperature increases as the heat flux increases for same Reynolds number. While the inner tube surface temperature decreases as the Reynolds numbers increase for same heat flux.

5.4. Local Nusselt number (Nu_x)

The variation of local Nusselt number (Nu_x) with dimensionless axial distance (Z^+), for horizontal position is shown in Figures (10 to 13) for selected runs. The general shape of these curves plotted on a semi logarithmic plot decreases, at annulus entrance until it reaches a minimum value after which (Nu_x) increases at annulus exit. It is clear that as Z^+ approaches zero the (Nu_x) must approach infinity since at Z^+ equal to zero, the boundary layer thickness is zero.

Figures (10&11) show the effect of the heat flux variation on (Nu_x) distribution for Re=598 and Re=1128 respectively. It is clear from these two figures that at the higher heat flux, the values of (Nu_x)were slightly higher than the values of lower heat flux. This may be attributed to the secondary flow superimposed on the forced flow effect increases as the heat flux increases leading to higher heat transfer coefficient. The smooth curve in each figure represents the theoretical pure forced convection (TPFC) based on constant property analysis of [10].

Figures (12&13) shows the effect of Reynolds number variation on (Nu_x)distribution with (Z^+), for heat flux (241 W/m^2) in Figure (12) and for high heat flux (545 W/m^2) in Figure (13). For constant heat flux, the (Nu_x) value gives higher results than the predicted pure forced convection value and moves toward the left of (TPFC) as Reynolds number increases. This situation reveals that the forced convection is dominant on the heat transfer process with little effect of buoyancy force for high Reynolds number. As the (Re) number reduced, the buoyancy effect expected to be higher which improves the heat transfer results.

It is necessary to mention that for horizontal annulus, the effect of secondary flow is high, hence at low Reynolds number and high heat flux, the situation makes the free convection predominant. Therefore, as the heat flux increases, the fluid near the inner tube wall becomes warmer and lighter than the bulk fluid in the annulus while the fluid near the outer tube (unheated) becomes heavier than the bulk fluid in the annulus. As a consequence, two upward currents flow along the inner tube circumference, and by continuity, the fluid near the inner surface of outer tube flows downward. This sets up an expected two longitudinal vortices, which are symmetrical about an inner tube. These vortices reduce the temperature difference between the inner tube surface and the air flow which lead to increase the growth of the thermal boundary layer along the annulus and causes an improvement in the heat transfer results. But at low heat flux and high Reynolds number the situation makes the forced

convection predominant and the vortices strength diminished which allow the forced flow to decrease the temperature difference between the inner tube surface and the air, hence the (Nu_x) values become higher.

The (Nu_x) distribution for the second calming section (L/D_h =20.93), and mentioned above when (L/D_h =13.95) in horizontal position, for the same Reynolds Reynolds number and same heat flux.

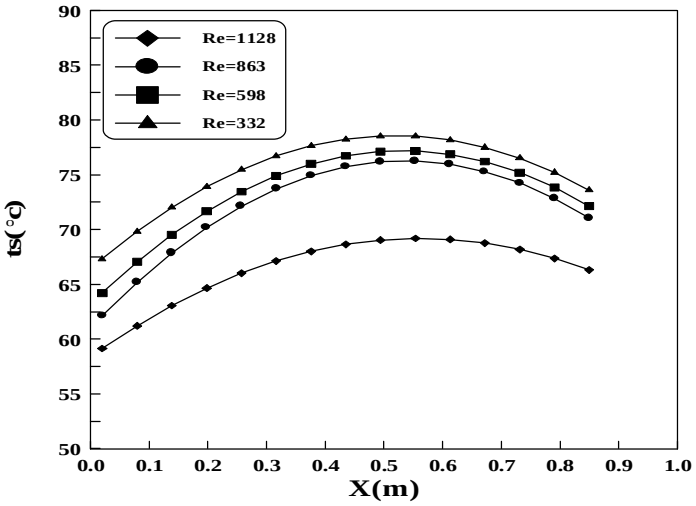

Figure (1). Variation of the inner tube surface temperature with the axial distance for q=241 W/m^2 , $L_{calm.}$=60, $q = 0^o$ (Horizontal).

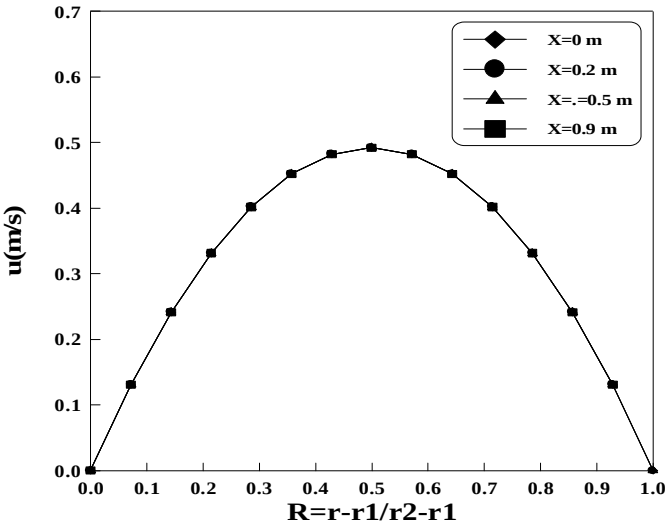

Figure(3). Developing velocity profiles along the annulus for q=0 w/m2 and Re=1200.

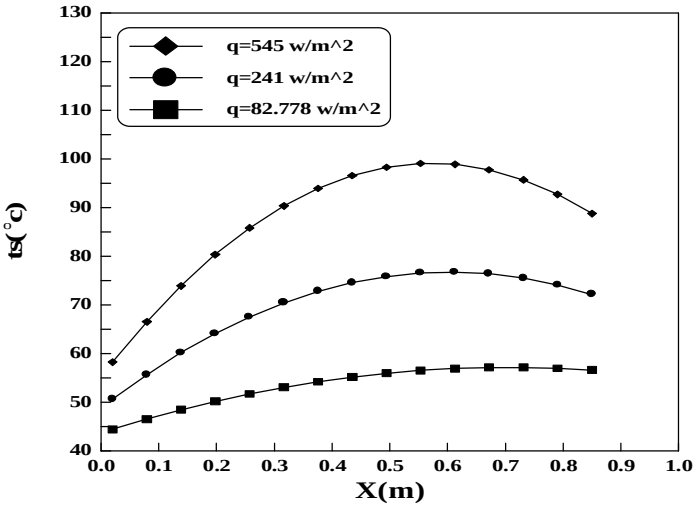

Figure(2). Variation of the inner tube surface temperature with the axial distance for Re=598, $L_{calm.}$=60 cm , $q = 0^o$ (Horizontal).

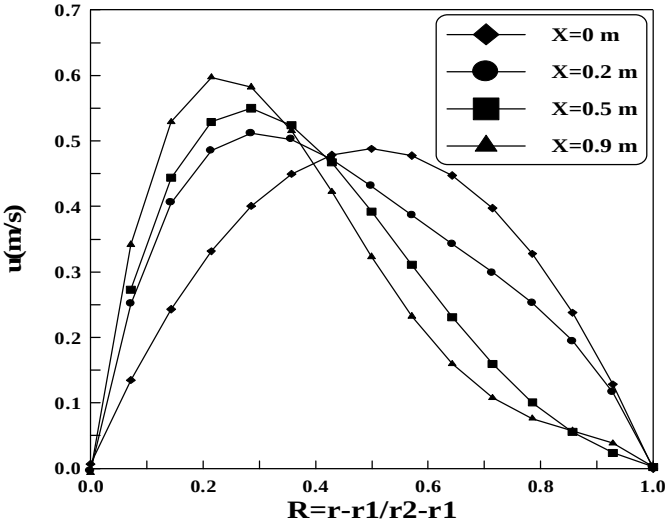

Figure (4). Developing velocity profiles along the annulus for q=90 w/m^2 and Re=1200.

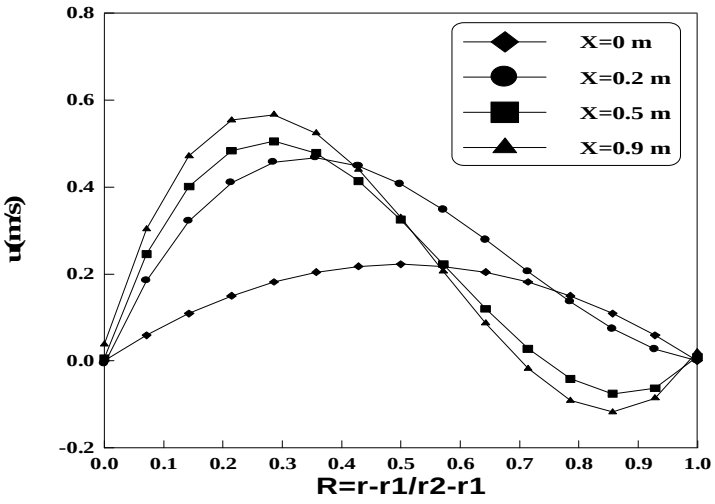

Figure (5). Developing velocity profiles along the annulus for q=288 w/m2and Re=540.

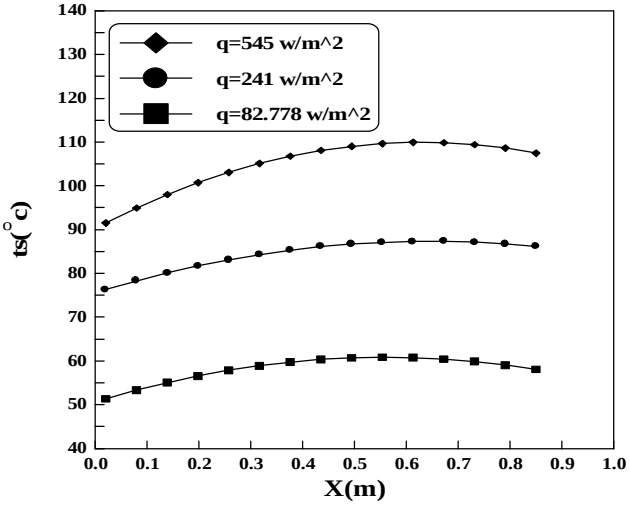

Figure(6). Variation of the inner tube surface temperature along the axial distance for Re = 332.

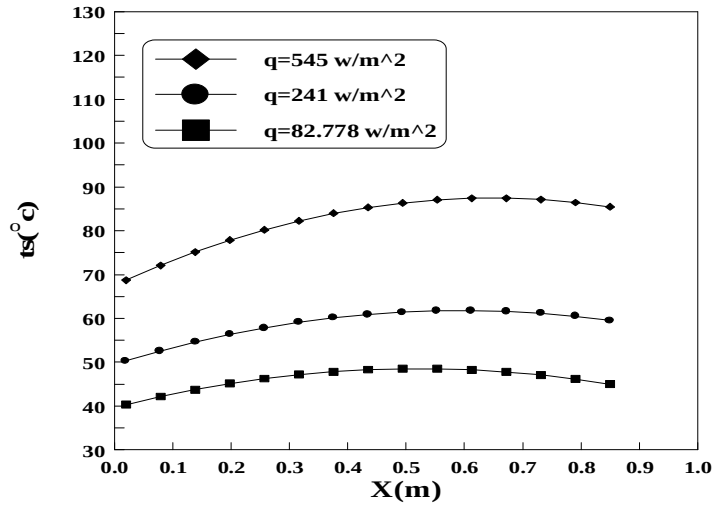

Figure (7). Variation of the inner tube surface temperature along the axial distance for Re=1128.

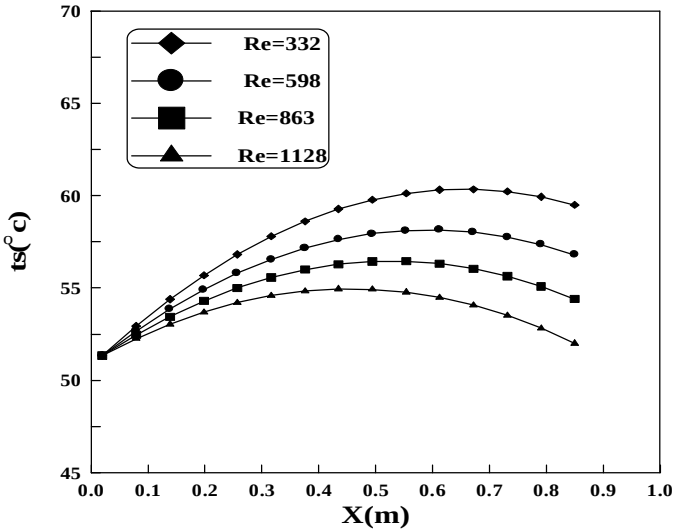

Figure (8) .Variation of the inner tube surface temperature along the axial distance for q= 82.77 w/m^2.

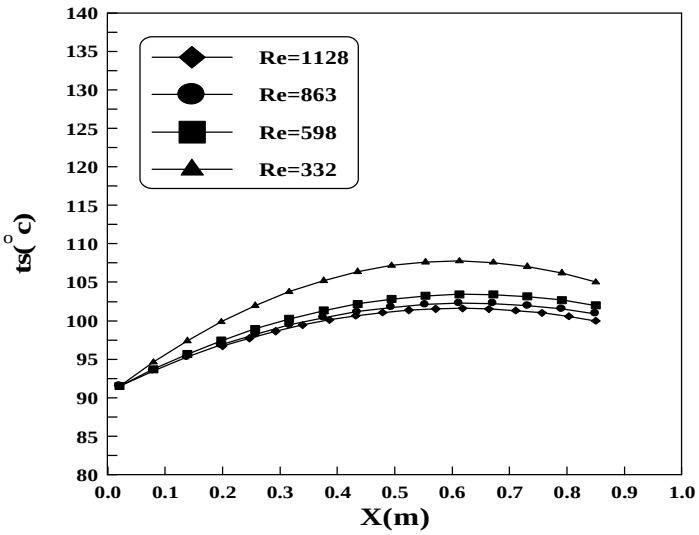

Figure (9) .Variation of the inner tube surface temperature along the axial distance for q=545 w/m^2.

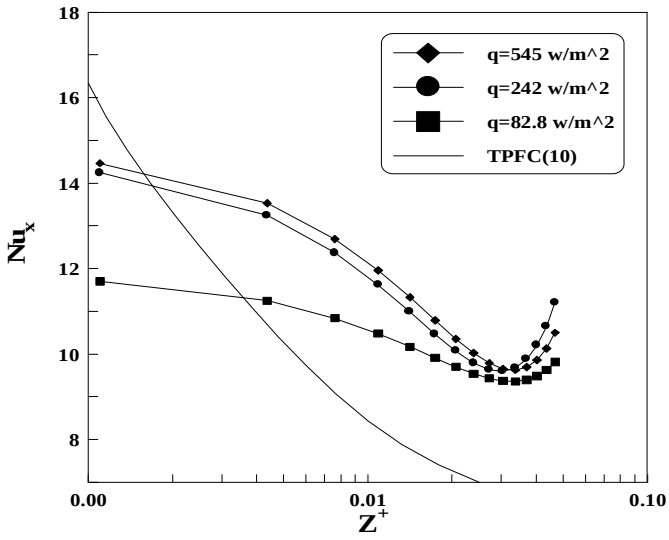

Figure (10). Variation of local Nusselt number with dimensionless axial distance for Re = 598, $L_{calm.}$ = 60 cm, q =0° (Horizontal).

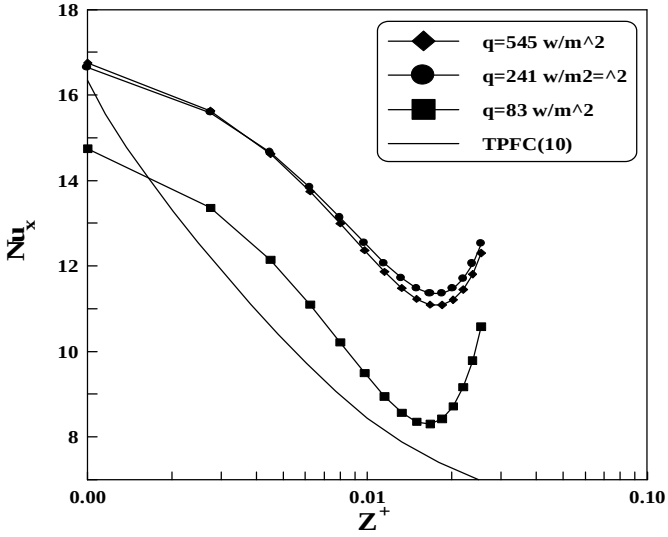

Figure (11). Variation of the local Nusselt number with dimensionless axial distance for Re = 1128, $L_{calm.}$= 60 cm, q =0° (Horizontal).

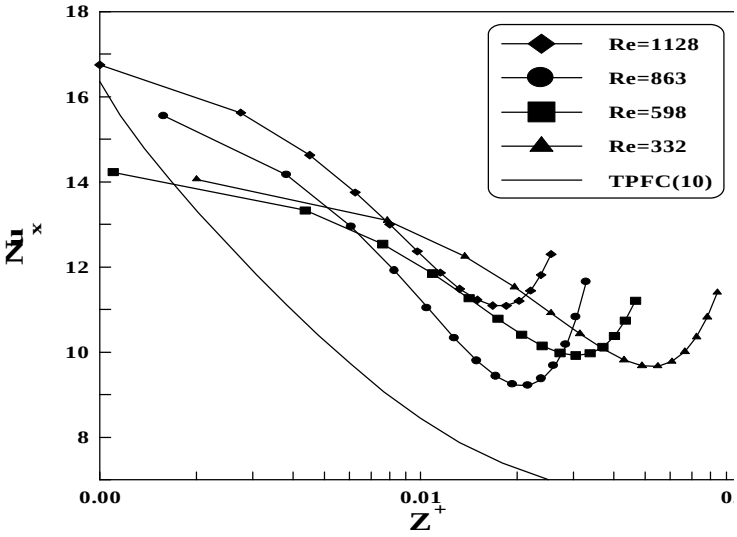

Figure (12). Variation of the local Nusselt number with dimensionless axial distance for q = 241 W/m^2, $L_{calm.}$ = 60 cm, q =0° (Horizontal).

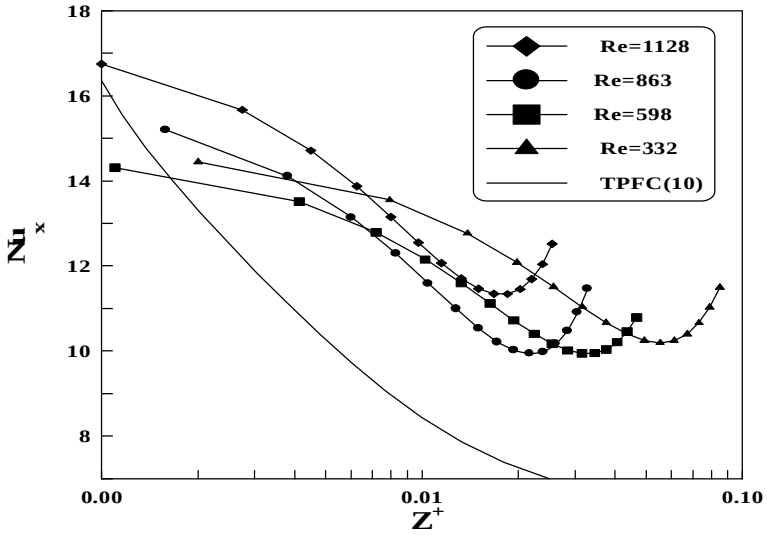

Figure (13). Variation of local Nusselt number with dimensionless axial distance for q = 545 W/m^2, $L_{calm.}$ = 60 cm ,q =0° (Horizontal).

6. Conclusions

From the results obtained, the follow conclusions can be drawn:

1. The temperature profile along the annulus shows a steep profile near the heated surface.
2. Near the annulus entrance the velocity profiles for different heat flux were found to be similar to those for pure forced convection behavior. But in the annulus downstream the velocity profiles were distorted and a high degree of central concavity appeared by the action of buoyancy forces.
3. For high (Re) number, the velocity profiles does not change with the increase of heat flux, from the pure forced convection trend and no effect of buoyancy forces. But in low (Re) number the velocity profiles change with the increase of the heat flux.
4. The central concavity of velocity profiles diminishes as (x) increases but does not vanish completely. The degree of central concavity decreases as (Re) number increases.
5. The variation of (Nu_x) with (Z^+),was affected by many factors summarized in the as, heat flux, buoyancy force, Reynolds number.

7. References

[1] Sha I., and Barnea Y., 1986, " Simple Analysis of Mixed Convection with Uniform Heat Flux ", Int.J. Heat Mass Transfer, Vol. 29, No.8,pp. 1139-1147.

[2] Cony J., and El-Shaarawi M., 1975, "Finite Different Analysis for Laminar Flow Heat Transfer in Concentric Annuli with Simultaneously Developing Hydrodynamic and Thermal Boundary Layers ", Int.J. For numerical methods in engineering, Vol. 9, pp.17-38.

[3] Chen Y., and Chung J.,1998, "Stability of Mixed Convection in a Differentially Heated Vertical Heated Vertical Channel ", J. of Heat Transfer, Trans. of ASME,Vol.120, pp. 127-132.

[4] Hashimoto K., Akino N., and Kawamura H., 1986, "Combined forced -Free Convection Heat Transfer to A Highly Heated Gas in a Vertical Annulus". Int.J.Heat Mass Transfer, Vol.29, No.1, pp. 145-151.

[5] Caampi M., Faggiani S., Grassi W., Incropera F.P., and Touni G., 1986, "Experimental Study of Mixed Convection in Horizontal Annuli for Low Reynolds Numbers ",Int. Heat Transfer Conference 8th, Vol. 3, pp. 1413-1418.

[6] Zysina-Molozhen, L.M., Safonov, L.p., Zabezhinskiy, L.D., and Fel'dberg, L.A., 1973, " Heat Transfer by Combined Forced and Natural Convection in an Annulus Formed by Tow Coaxial Cylinders ", Heat Transfer-Soviet Research, Vol.5, No.4.

[7] Bohne, D., and Obermeier, E., 1986, "Combined Free and Forced Convection in a Vertical and Inclined Cylinder Annulus ", Int. Heat transfer conference 8th oh, Vol.3, PP.1401-1406.

[8] Remash K. and Benjamin G., 1986, "Heat Transfer by Mixed Convection in a Vertical Flow Undergoing Transition ", Int.J Heat Mass Transfer, Vol.29, No. 8, pp. 1211 -1218.

[9] Worsoe-Schmidt, P.M., 1967, "Heat Transfer in the Thermal Entrance Region of Circular Tubes and Annular Passages with Fully Developed Laminar Flow", Int.J.Heat Mass Transfer, Vol. 10, pp. 541 - 551.

[10] Lundberg, R.E., Reynolds, W.C., and McCuen, P.A., 1962, "Heat Transfer in Annular Passages. General Formulation of the Problem for Arbitrarily Wall Temperature or Heat Fluxes ", J. Heat Mass Transfer, Vol. 6, pp. 438 – 439.

[11] Huets, J., and Petit, J.P., 1974, " Natural and Mixed Convection in Concentric Annulus Space-Experimental and Theoretical Results for Liquid Metals", Int. Heat Transfer conference 5th,Tokyo, Vol. 3, PP.169-172.

[12] Hanzawa, T., Sako, A., Endo, H., Kagwa, M., and Koto, K., 1986, " Combined Free and Forced Laminar Convective Heat Flux From Isothermally Heated Inner Tube in Vertical Concentric Annulus " J.Chem. Eng. Japan, Vol.97, pp.78-81.

[13] Sherwin, K., and Wallis, J.D., 1972, " Combined Natural and Forced Laminar Convection for Upflow Through Heated Vertical Concentric Annuli ", Thermodynamics and Fluid Mechanics Conference, Inst.Mechanical Engineers, pp.1-5.

8 . Nomenclature

Symbol		Description	Unit
C_1, C_4	=	Constants, eqs. (6)& (7)	--------
C_2,C_5	=	Constants, eqs. (6)& (7)	1/ $^{\circ}$C
C_3,C_6	=	Constants, eqs. (6)& (7)	1/ $^{\circ}C^2$
Cc_1,Cc_2,Cc_3	=	Constants, eq. (8)	--------
Cc_4,Cc_5 ,Cc_6	=	Constants, eq. (9)	--------
C_p	=	Specific heat at constant pressure	J/kg.$^{\circ}$C
D_h	=	Hydraulic diameter	M
G	=	Gravitational acceleration	m/s^2
H	=	Heat transfer coefficient	W/m^2.$^{\circ}$C
K	=	Thermal conductivity	W/m.$^{\circ}$C
L	=	Annulus length	m
M	=	Radial mesh point in the annular space	---------
N	=	Axial mesh point	---------
P	=	Dimensionless pressure at any cross section $= p - p_i / r u_m^2$	---------
R	=	Radial coordinate	m
r_1	=	Inner radius of inner tube	m
r_2	=	Outer radius of outer tube	

t_m	=	Mixingcup temperature over any cross section	$^{\circ}C$
T	=	Dimensionless temperature $= G.C_5(t - t_i)$	---------
T_A , T_B	=	Constants	---------
U	=	Axial velocity component	m/s
U_m	=	Axial mean velocity	m/s
V	=	Radial velocity component	m/s
V	=	Dimensionless radial velocity component $= v/u_m$	---------
X	=	Axial coordinate	m

Dimensionless Group

Re	=	Reynolds number	$= r.v.D/m$

Superscript

a	Air
i	Annulus entrance (inlet)
s	Surface
t	Total
w	Wall
x	Local

A New Technique for PAPR Reduction in OFDM System

Ahmed K. Abed

Electrical & Electronic Department

College of Engineering

Thi-Qar University

Algenaby1975@yahoo.com

Abstract

Orthogonal frequency division multiplexing (OFDM) is an attractive technique for modern wireless communication. One major drawback of orthogonal frequency division multiplexing schemes is the high peak to average power ratio (PAPR) of the output signal. Selecting mapping (SLM) and partial transmit sequences (PTS) are two important techniques for reducing PAPR, but they need to transmit side information to indicate how the transmitter generates the signals. In this paper, we proposed an efficient technique to reduce PAPR in OFDM system. For this technique, circular shifter used to produce K cyclic sequences from the same information sequence. These sequences XOR with K randomly generated keys, the same keys used in receiver side to detect data. The sequence with the lowest PAPR among K sequences is chosen for transmission. Side Information (SI) is coded using Hamming code and embedded into the information sequence. Computer simulation tests have been applied on BPSK and N= 64 subcarriers OFDM system with the proposed method. Moreover, this system will be evaluated under the effect of AWGN channel. The results exhibit the ability of such technique to reduce the PAPR without major effect on the system performance as compared with the conventional OFDM technique. The PAPR of OFDM signal is further reduced by 4–5 dB by this technique.

Keywords: Orthogonal Frequency Division Multiplexing OFDM, Peak to Average power ratio (PAPR), AWGN channel.

المستخلص

التجميع المتعدد بتقسيم التردد المتعامد OFDM تقنية فعالةللاتصالات اللاسلكية المتطورة . ارتفاع نسبة القمة إلى معدل القدرة واحدة من المشاكل الرئيسة في نظام OFDM . اختيار الأنماط الأنسب SLM و إرسال المجزء للنمط PTS تعتبر من أهم الطرق لتقليل PAPR ولكن مثل هذه الطرق تحتاج إلى إرسال معلومات إضافية مما تؤدي إلى تقليل كفاءة هذه الطرقتين. في هذا البحث اقترحت تقنية كفوءة لتقليل نسبة قمة إلى معدل قدرة الإشارة PAPR في نظام OFDM. في هذه التقنية استخدم المزحزح الدائري circular shifter لتوليد K من الأنماط المزحفة بشكل دائري لنفس البيانات .هذه الأنماط تجمع مع K من المفاتيح عن

طريق بوابات XOR ، النمط الذي يرسل هو الذي يمتلك اقل نسبة أقصى إلى معدل قدرة الإشارة Minimum PAPR. المعلومات الإضافية SI لمقدار الإزاحة تشفر باستخدام Hamming code وتدمج مع نمط البيانات المرسلة.تمت محاكاة النظام المقترح لمنظومة OFDM باستخدام الحاسوب حيث اعتمد عدد الحاملات N=64 وبتضمين Binary Phase Shift Keying (BPSK) ,اختبر النظام تحت تأثير ضوضاء الكاوسية للقناة AWGN channel . النتائج أظهرت قدرة النظام المقترح لتقليل PAPR بالمقارنة مع النظام التقليدي Conventional OFDM بحدود 4-5 ديسبل.

1. Introduction

Orthogonal frequency division multiplexing (OFDM) is a promising technique for high speed data rate transmission [1].Moreover, OFDM has also been widely applied to wideband communications over mobile radio channels, high-bit-rate digital subscriber lines (HDSL), and digital audio broadcasting (DAB), etc. However, one of the implementation drawbacks of OFDM is that the transmitted signal has a high peak to-average power ratio (PAPR). A communication system with high PAPR not only decreases the efficiency of a linear high power amplifier but also increases the complexity of an analog-to-digital converter. Therefore, the subject of finding a computationally efficient algorithm to decrease the PAPR in OFDM systems has become an active research.

Recently, many methods have been proposed to reduce the PAPR of the transmitted signal. Clipping is a simple effective technique for PAPR reduction by clipping the peak amplitude of amplification [2]. Since clipping is a nonlinear process, it may cause significant in-band distortion and out-of-band radiation. Several coding schemes that use a special forward error correcting code set that excludes OFDM signals with a large PAPR, thus they significantly reduce the rate of transmission for large values of N [3]. Selective mapping (SLM) [4] and partial transmit sequence (PTS) [5-6] are based on scrambling each OFDM signal with different scrambling sequences to obtain lower PAPR, and the sequence with the lowest PAPR is transmitted, both of which need to transmit side information (SI) to the receiver to recover the original sequence. In this paper, we proposed an efficient technique to reduce PAPR in OFDM system .The proposed technique depend on generating K pattern of same information sequence by using K circular shifters and K Keys scrambling by XOR gates .The identity of shifting circular registers sent as side information and embedded in data information. The performance of the proposed technique for reducing the PAPR is presented. This paper is organized as follow. Section 2 presents the definition of an OFDM system and the PAPR. Section 3 introduces the proposed system model. Results are presented in Section 4, and finally the paper concluded in Section 5.

2. OFDM system and paper definition

OFDM is a block modulation scheme where a block of information symbols is transmitted in parallel on sub-carriers. The time duration of an OFDM symbol is times larger than that of a single-carrier system. An OFDM modulator can be implemented as an inverse Fast Fourier transform (IFFT) on a block of information symbols followed by an analog-to digital converter (ADC).Consider an OFDM system with N sub-carriers. Each OFDM block(OFDM symbol), x(t), $0 \le t \le T$, consists of N complex baseband data X_0 , X_1,….., X_{n1} carried on the N subcarriers respectively for a symbol period of T. The OFDM symbol $x(t)$ is:

$$x(t))= \begin{cases} \frac{1}{\sqrt{N}} \sum_{n=0}^{N-1} X_n e^{j2\pi n \Delta f t} & 0 \le t \le T \\ 0 & \text{elsewhere} \end{cases} \quad (1)$$

Where Df . **1**/$T$is the sub-carrier spacing and **n** denotes the index in frequency domain and X_n is the complex symbol in frequency domain. Furthermore, equation (1) can be expressed using the IFFT [7].

Figure (1) shows a typical block diagram of a Basic OFDM system. The serial input data stream is converted to N parallel sub channels and mapped with a selected modulation scheme, resulting in N subchannels containing the information in complex number form.

These complex values are then sent to the N channel IFFT. The parallel signals are converted back to a serial sequence by using a P/S converter. A guard interval is inserted to reduce the effect of ISI caused by multipath propagation. Finally, the signal is converted to analogue signal and converted back up to a suitable form for transmission. At the receiver, a reverse procedure is used to demodulate the OFDM signal.

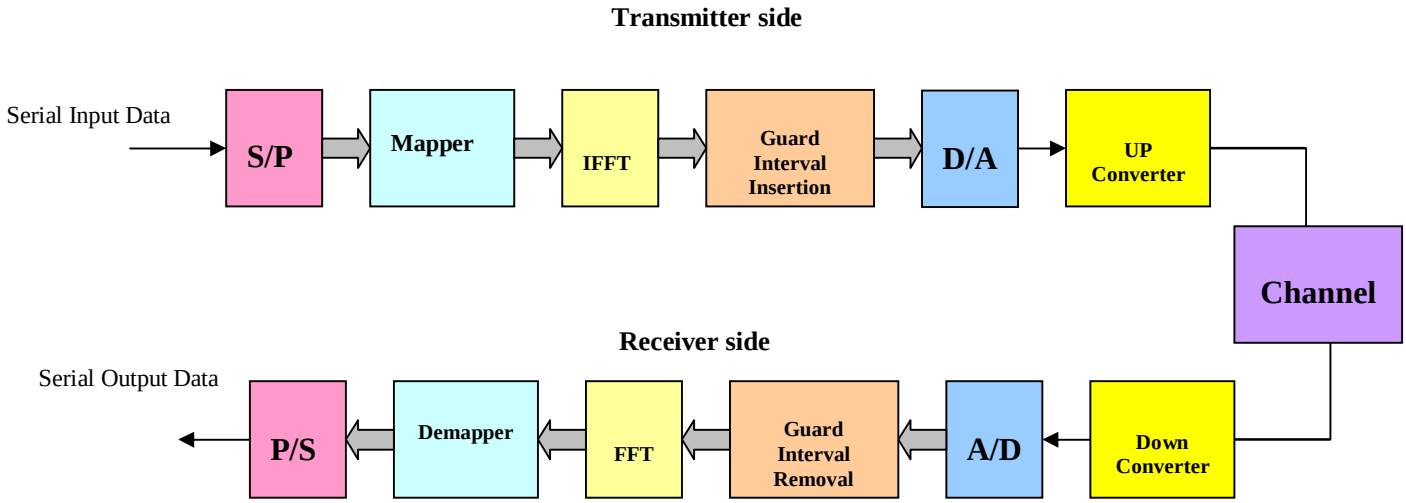

Figure (1). Block diagram of the basic OFDM system.

According to eq. (1), the peak instantaneous power is:

$$P_{max}= \max_{t\in[0,T)} |x(t)|^2 \quad (2)$$

An OFDM symbol sequence can be represented by $x(t)$, $x(t+T),\ldots\ldots,x(t+mT),\ldots$

The average power of OFDM symbol sequence is:

$$Pav(x_1, x_2,\ldots\ldots\ldots, x_{n-1}) = \sum_{k=0}^{N-1} E[|x_k|^2] \quad (3)$$

Where $E[|x_k|^2]$ is the expected value of $|x_k|^2$ .The peak average power ratio (PAPR) of the OFDM symbol $x(t)$ is:

$$PAPR = \frac{P_{max}}{P_{av}(x_0, x_1,\ldots\ldots,x_{n-1})} = \frac{\max_{t\in[0,T)} |x(t)|^2}{\sum_{k=0}^{N-1} E[|x_k|^2]} \quad (4)$$

If the power of the input signal is standard, the $E[|x_k|^2]$ equal to 1.Then:

$$PAPR = \max_{t\in[0,T)} |x(t)|^2 = \max_{t\in[0,T)} \left| \frac{1}{\sqrt{N}} \sum_{n=0}^{n-1} X_n e^{j2p\Delta ft} \right|^2 \le N \quad (5)$$

As a result, the PAPR value is not larger than the number N of sub carriers, e.g. the peak power value of OFDM signals is N times larger than its average power. So, the maximum PAPR equals to N. With the increase in the number N of sub channels, the maximum PAPR increases linearly. This makes high demands on the linear range of the front-end amplifier in sending side.

Although the probability of the largest PAPR is low, in order to transfer these high PAPR of OFDM signal without distortion, all the linearity of the High Power Amplifier (HPA) in sending side, the front-end amplifier and A/D converter should meet the high requirement. But these equipments meeting the high requirement are expensive. Therefore, it is necessary and important to reduce PAPR in OFDM system.

For an OFDM signal with N subcarriers, the PAPR can be defined as [8]:

$$PAPR = \frac{\max|x(t)|^2}{E|x(t)|^2} \quad (6)$$

In particular, a base band OFDM signal with N sub channels has maximum PAPR equal to :

$$PAPR_{max}=10\log_{10}(N) \quad (7)$$

For M-PSK modulation, there are only M^2 sequences having maximum PAPR equal to 10log (N) as described in [9].This means, the number of sequences that gives very high PAPR is small. If the number of sub channels increases, the ratio of the sequence (**R**) that gives so much PAPR and all distinct sequences decreases rapidly. The overall number of distinct sequences for the N subcarriers OFDM system with M-PSK is M^N. Thus the ratio can be obtained by:

$$R = \frac{M^2}{M^N} = M^{2-N} \quad (8)$$

From the central limit theorem, it follows that for large values of N (N>64), the real and imaginary values of x(t) become Gaussian distributed. Therefore the amplitude of the OFDM signal has Rayleigh distribution, with a cumulative distribution given by $F(z)= 1- e^{-z}$. The probability that the PAPR is below some threshold level can be written as:

$$P(PAPR \leq z) = (1 - e^{-z})^N \quad (9)$$

In fact, the Complementary Cumulative Distribution Function (CCDF) of PAPR of an OFDM is usually used, and can be expressed as:

$$P(PAPR > PAPRo) =1- (1 - e^{-PAPRo})^N \quad (10)$$

This theoretical derivation is plotted against simulated values in Figure (2) for different values of sub carriers N.

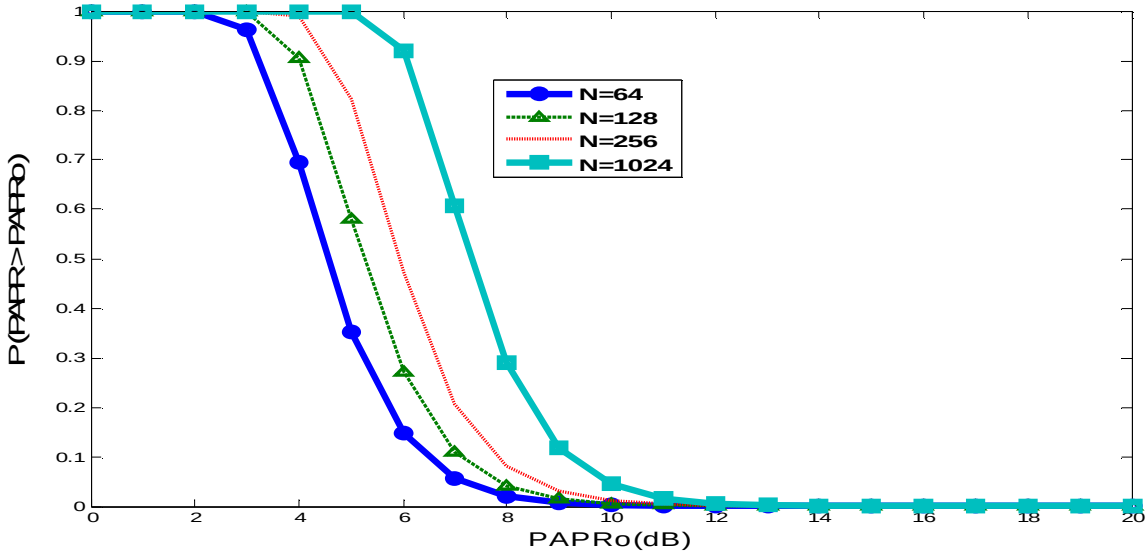

Figure (2). CCDF for different values of Sub carriers.

3. The proposed OFDM system model

The main idea in this research is to generate multiple and different patterns of the same information. Generation of these patterns leads to increasing the likelihood that the pattern which will have the least PAPR among the various patterns will be sent. A number of circular shift registers is used to generate different patterns so that each pattern is different from the other in the amount of offset in circular shift registers as shown Figure (3). Additional information that describes the amount of offset in the shift register is mixed with data. Therefore; the proposed method will not need to send the side information separately from data as in the case of SLM method. The error in the amount of shifting in the receiver side leads to an error that occurs in all the collected data, leading to increasing the BER. Hamming code method has been adopted to encrypt the amount of the offset to reduce the BER.

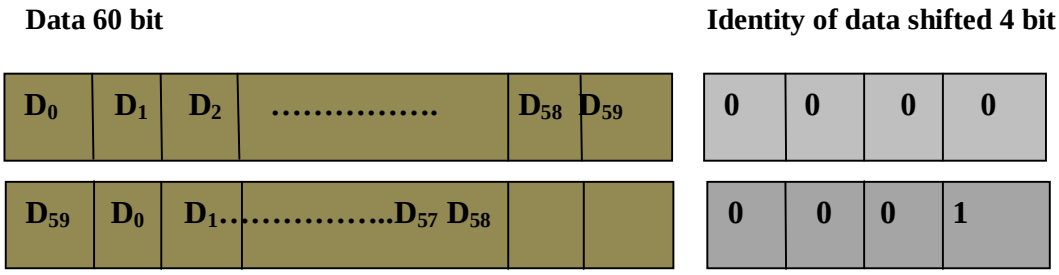

Figure(3). Generation of the different patterns by using circular shifters.

Figure (4) depicts the block diagram of the proposed transmitter TX-OFDM system, circular shifters are used to produce K cyclic sequences from the same information sequence where the n^{th} circular shifter shifts the sequence data by n bits (n=0 to K-1). These sequences XOR with randomly generated keys (K=16). Identity of Shifted Data is embedded as side information. The information (Data & Identity of Shifted Data) are modulated by using BPSK. An inverse Fourier transform converts the frequency domain information (Data & Identity of Shifted Data) set into samples of the corresponding time domain representation of this information. The sequence with the lowest PAPR, among K sequences, is chosen for the transmission. At the receiver RX-OFDM, a reverse procedure is used to demodulate the OFDM signal.

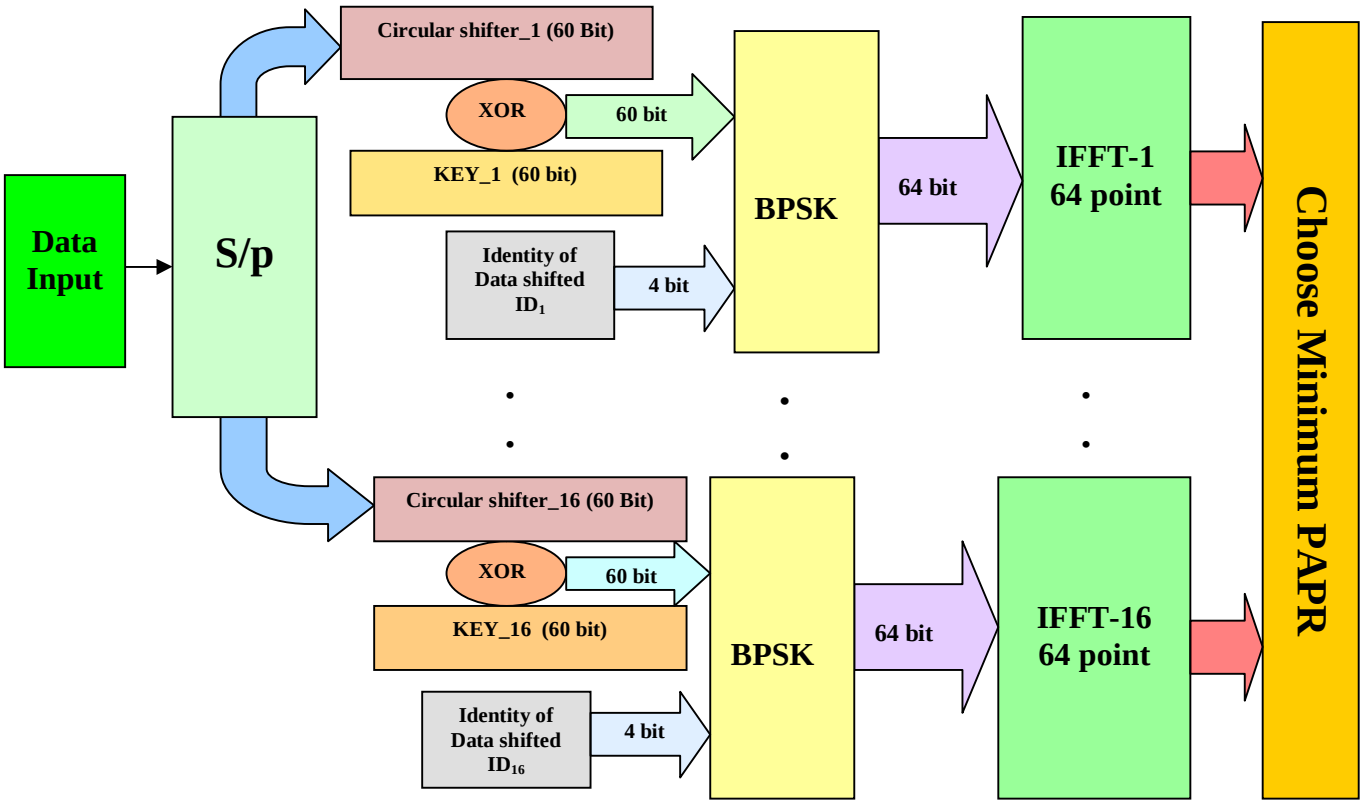

Figure (4).Block diagram of TX-OFDM proposed system.

4. Results and discussion

The proposed model of transmitter and receiver OFDM was realized in MATLAB **7.6 (R2008a)** octave codes, BPSK modulated and N=64 sub-carriers are considered. Figure (5) shows the normalized output power of the OFDM system with and without proposed technique. From the Figure (5-a), wide variation in the instantaneous power of the conventional OFDM system which leads to large PAPR can be easily observed. Comparing with Figure (5-b), we can observe that the instantaneous power variation is reduced when we used the proposed technique.

Figure (**6**) depicts the (**CCDF**) of PAPR for the proposed OFDM system for different No. of circular shifters. The PAPR statistics improved with increasing No. of circular shifters. When No. of circular shifters are equal to 16, the PAPR can be reduced by 4-5dB as compare with the conventional OFDM system.

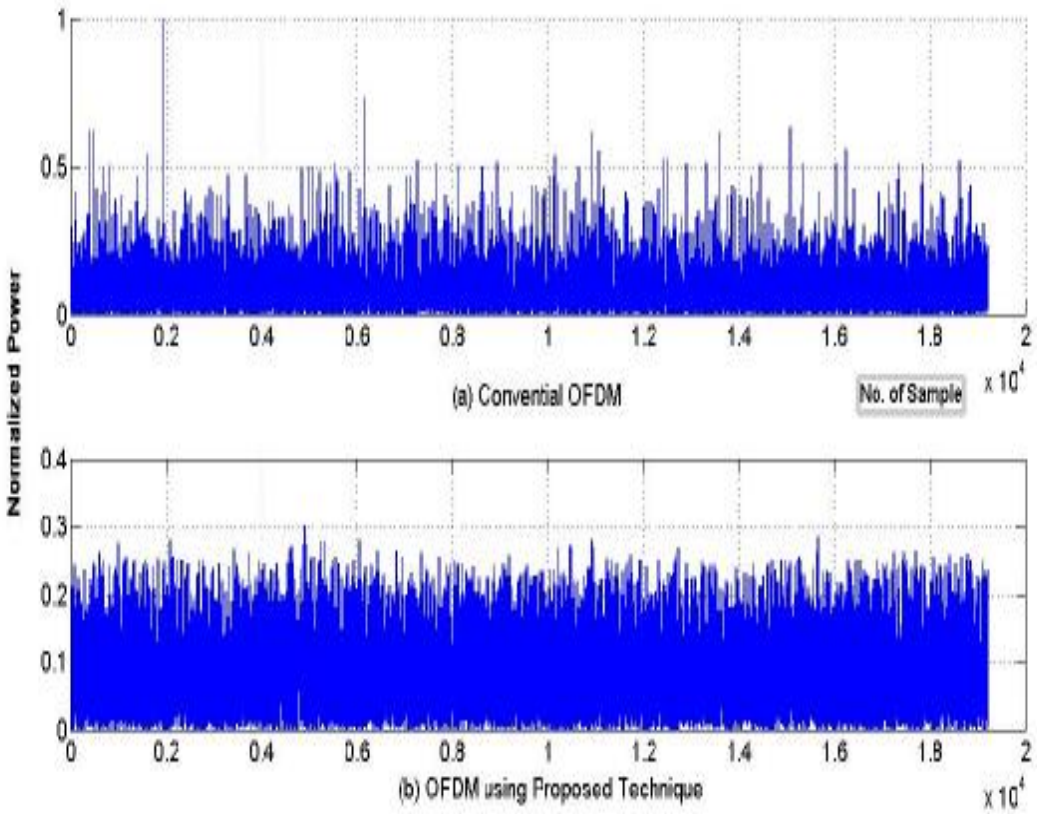

Figure (5).Normalized power of proposed OFDM system in time domain.

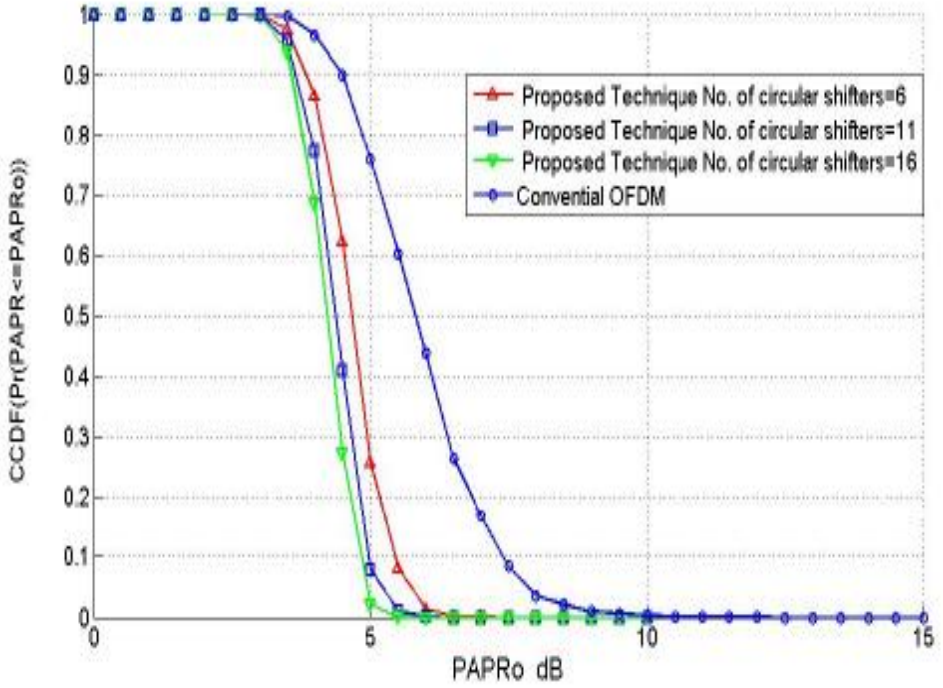

Figure (6). CCDF of papr for the proposed system.

The used Keys and XOR gates in the proposed OFDM system description in Figure (**4**) played a key role in obtaining a wide variation patterns for the same information and thus become to get the lowest PAPR possible.

The proposed system has been tested in the presence of noise in channel (AWGN) so as to measure the Bit Error Rate (BER). Results showed that the proposed system with K=16 circular shifters gave Bit Error Rate higher than the conventional system .The error occurs in one of the bits of Identity of Data shifted (ID) lead to crash whole the data frame which leads to increased Bit Error Rate. Error correction method is used for ID in order to reduce the error in the data frame in receiver side. Hamming code (7,4) method is used to detect the error of ID in receiver side. Results showed that the proposed coded OFDM system showed quite similar performance to the convention system, as in Figure (**7**).

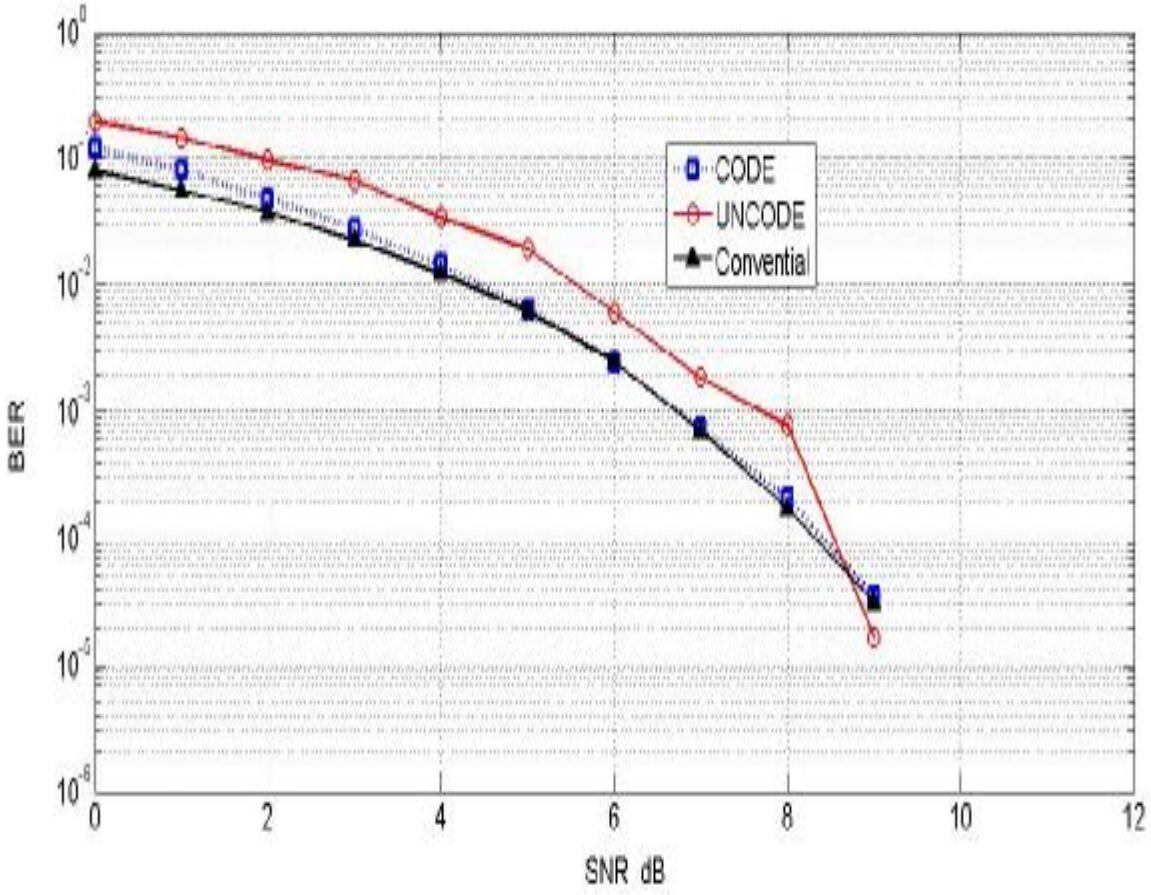

Figure (7).BER performance of the propose OFDM system.

5.Conclusions

A new Technique is proposed for the PAPR reduction in OFDM system, based on K circular shifters to shift data symbol by n^{th} bit and XOR each with K keys. Then the sequence with minimum PAPR is chosen for transmission. The proposed technique minimizes the variation in the instantaneous power of the conventional OFDM system as well as reduces PAPR. The PAPR reduction is forward proportionally to the number of circular shifter. PAPR is reduced by 4-5 dB when compared with conventional OFDM. The proposed technique offers a higher BER performance compared with conventional OFDM. The BER performance for the proposed scheme can be improved by using appropriate coding technique for ID such as Hamming code (7,4). The use of Hamming code makes the BER for the proposed OFDM system very close to that of conventional OFDM system. However, one of the difficulties in the new technique is the large number of IFFT. The proposed method is similar to SLM method, but the proposed technique doesn't require any side information as in SLM method.

6.References

[1] Han S. H. and Lee J. H., Apr. 2005,“An overview of Peak-To-Average Power Ratio Reduction Techniques For Multicarrier Transmission”, IEEE wireless Commun., vol. 12, no. 2, pp. 56.65.

[2] Wu L.J. and Li Y.W., Aug.2007,"Reducing the PAR In OFDM Systems by Clipping Scheme". Natural Computation, 2007. ICNC 2007. Third International Conference on, vol.5, pp: 63 – 68,.

[3] Davis J. A. , Jedwab J., 1997, "Peak-to-Mean Power Control and Error Correction for OFDM Transmission Using Golay Sequences and Reed-Muller Codes ". Electronics Letters, vol.33, no.(4),pp 267-268.

[4] Chin-Liang W. and Yuan O. , Dec. 2005,"Low-Complexity Selected Mapping Schemes For Peak-To-Average Power Ratio Reduction In OFDM Systems" ,IEEE Transactions on Signal Processing, vol. 53, pp. 4652-4660.

[5] Tao J. , Weidong X., Paul C. Richardson, Jinhua Guo, and Guangxi Zhu.,Sept.2007,"PAPR Reduction of OFDM Transmission Using Partial Transmit Sequences With Low Computational Complexity", IEEE Transactions on Broadcasting. vol.53, no.3,.

[6] Dae-Woon L., Seok-Joong H., Jong-Seon N. and Habong C.., March 2006, "A New PTS OFDM Scheme with Low Complexity For PAPR Reduction”, IEEE Transactions on. Broadcasting,vol.52, pp:77-82.

[7] Jayalath A. D. S.,Australia2002,"OFDM for Wireless Broadband Communications (Peak Power Reduction, Spectrum and Coding)" , Phd thesis, Monash University, Clayton, VIC 3800.

[8] Van Nee R. J., and Prasard R.,1999,"OFDM for Wireless Multimedia Communications", Artech House,Boston.

[9] Ochiai H., March 2001,"Analysis and Reduction of Peak to Average Power Ratio in OFDM System", PhD Thesis, The Graduate School of Engineering, The university of Tokyo, Japan.

Finite Element Prediction of Temperature Rise Distribution in Turning Process of AISI 1045 Carbon Steel

Assmaa A. Kawi
Mechanical Engineering Dep.
College of Engineering
University of Basrh

Sana J.Yaseen
Mechanical Engineering Dep.
College of Engineering
University of Basrh

Rana L.
Mechanical Engineering Dep.
College of Engineering
University of Basrh

Abstract

In this paper the code DEFORM-3D V6.1 was used to perform a finite element analysis simulating the turning process of AISI 1045 carbon steel. A series of thermal simulations have been performed, the value and location of maximum temperature have been determined. The comparison of the simulations with earlier works gave promising trend for the presented work with a maximum percentage of error 3.23%. The results of this work show that the maximum temperature exists in the vicinity of the cutting edge. i.e. in the tool-chip contact and then starts cooling immediately when the tool crosses this region. Besides the maximum temperature in the tool-chip interface increases as the cutting time increases until the process reaches the steady-state condition where the temperature is alternating around the mean temperature. Finally the behavior of temperature differs in value and distribution for the same location and time (same boundary conditions) in the cutting direction with the change in depth of cut where the maximum temperature occurs at maximum depth of cut.

تنبؤ نظرية العناصر المحددة بتوزيع ارتفاع درجات الحرارة في عملية الخراطة

المستخلص

في هذا البحث استخدم برنامج Deform-3D V6.1 لإجراء تحليل العناصر المحددة لمحاكاة عملية قطع متعامد لصلب كاربوني نوع AISI 1045. تم تنفيذ سلسلة من عمليات المحاكاة لتحديد قيمة ومكان درجة الحرارة القصوى. تم مقارنة نتائج العمل الحالي مع أبحاث سابقة ولوحظ وجود توافق مقبول بين النتائج حيث كانت أعلى نسبة للخطأ3.23%.نتائج العمل الحالي تؤكد بأن درجة الحرارة القصوى موجود على مقربة من حافة القطع في منطقة تلامس الأداة مع الرايش ثم تبدأ درجة الحرارة بالانخفاض على الفور عندما تتجاوز الأداة هذه المنطقة. بالإضافة إلى ذلك تزاد قيمة درجة الحرارة القصوى في منطقة تلامس الأداة مع الرايش كلما تقدمت الأداة حتى تصل عملية القطع إلى حالة الاستقرار التي تبدأ بعدها درجة الحرارة بالتذبذب حول قيمتها المتوسطة. أخيراً وجد إن سلوك درجة الحرارة يختلف من

حيث القيمة والتوزيع لنفس الموقع والوقت (نفس الشروط الحدية) في اتجاه القطع مع التغيير في عمق قطع حيث لوحظ ان أقصى درجة حرارة تحدث في أقصى عمق قطع.

1. Introduction

During metal cutting, the work of plastic deformation and friction between the cutting tool and workpiece are the main heat sources and can result in a significant temperature increase both in the machine material and the cutting tool. The temperature increase, in its turn, changes material properties such as the yield stress, coefficient of thermal expansion, conductivity and specific heat, thus influencing deformation processes and stresses evolution in the workpiece[1].Generally, increasing temperature decreases the strength of the workpiece material and thus increases its ductility[2] . Besides, analysis of the thermal fields in metal cutting has been the topic of research interest for many years. It is a complex problem, involving many parameters and is too cumbersome to be truly simulated in any mathematical form. The problem zone being too small, any experimental technique would also have definite limitations in practical application and in these cope and reliability of the measurements. Nevertheless, it is undoubted that the thermal phenolmenain metal cutting play a vital role in influencing the tool wear rate. Shear zone temperatures influence the deformation process and in effect the chip–tool interface temperatures[3]. Another added complexity is the characteristic influence of the steep thermal gradients that gives rise to thermal stresses. Furthermore , the combined thermo-mechanical stresses would result in complex stressed states for the cutting tools.

The generation of heat arises from several main sources, namely the primary shear zone at the tool workpiece interface, the secondary shear zone at the tool chip interface, and at the clearance face contact[4].All energy involved in plastic deformation (in the shear zone and at the chip–tool interface) is converted into heat[5].

The temperature in the primary and secondary shear zones are usually very high ,due to the high shear and friction energies dissipated during a machining operation[6].The temperature distribution in the work material and tool-chip is affected by tool material, workpiece material ,cutting speed, feed deep and the tool coating materials. Obviously, it is necessary and significant to establish the nature and distribution of the metal cutting temperatures.

An analyses of the one-dimensional transient temperature distributions in monolayer coated tools and the analytical formulae of the transient temperature distributions for the monolayer cutting tools were obtained using Laplace Transform was presented by[7] .Heat partition and

the temperature rise distribution in the moving chip as well as in the stationary tool due to frictional heat source at the chip tool interface alone in metal cutting were determined analytically .This was studied by[8] using functional analysis. A novel approach to the prediction of cutting temperature in multi-layer coated tools was presented. This approach considers the contact mechanics at asperity level and resulting thermal constriction resistance phenomenon [9].Proposition of an innovative approach, based on a simple inverse procedure, in order to identify both the heat flux flowing into the tool through the rake face and the heat transfer coefficient between the tool and the environment during a typical orthogonal cutting process. It is worth pointing out that the effective determination of such quantities is necessary in order to carry out a reliable prediction of the temperature distribution in the tool during the process [10].The tool-chip interface temperature is measured experimentally during turning of EN-31 steel alloy with tungsten carbide inserts using a tool-work thermocouple technique[6]. The relevance of temperature measurement method to high speed cutting. New temperature measurement results obtained by a thermal imaging camera in high speed cutting of high strength alloys are also presented [2].A study deals with the qualification of the tribe logical system 'work material–coated carbide cutting tool–chip' to achieve a clearer understanding of the heat flow during the turning process in tool substrates, this highlights the advantages offered by certain coatings which combine hardness and self-lubricating properties, for example (Ti,Al)N+MoS2 [11]

The FEM package applied allows the temperature distribution and heat flux intensity to be predicted closer to appropriate measurements and computations [12].Also, chip formation and possibly its breaking can be determined faster than using costly and time consuming experiments. It is especially important that FEM analysis can help to investigate some thermo dynamical effects occurring in the cutting zone which, as so far, cannot be measured directly [13].A study was done to compare two variants of the FEM simulation model of orthogonal cutting process of AISI 1045 carbon steel with uncoated and multilayer-coated carbide tools i.e. standard and Power Law–Temperature Dependent (PL-TD) options by [12].

To check the applicability of various simulation models to obtain finite element solutions of cutting forces, specific cutting energy and adequate temperatures for a range of coated tool materials and defined cutting conditions commercial explicit finite element code Third wave Advantage has been used in simulations of orthogonal cutting processes performed by means of uncoated carbide and coated

tools also studied by [14] using Commercial explicit finite element code Third wave Advantage. Two different approaches were proposed in [15], a former based on a pure thermal simulation once the thermal flow on the tool is properly calculated. The latter, on the contrary, is based on an artificial modification of the heat transfer coefficient at the interface between the chip and the tool in the thermo-mechanical simulation.

2. Finite element model

2.1. Description of the simulated model

In recent years, the finite element method has particularly become the main tool for simulating metal cutting processes. Finite element models are widely used for calculating the stress, strain, and temperature distributions. In consequence, temperatures in the tool, chip and work piece, and possibly its breaking can be determined faster than using costly and time consuming experiments. It is especially important that FEM analysis can help to investigate some thermo dynamical effects occurring in the cutting zone which, as so far, cannot be measured directly.

In this paper the code DEFORM-3D V6.1 was used to perform a finite element analysis simulating the turning process this finite element model used for the plane-strain orthogonal metal cutting simulation is based on the Lagrangian techniques, thermo-mechanically coupled modeling software with adaptive remeshing.The initial arrangement of both the workpiece and the tool in the simulation model shown in Figure (1-a). In simulations with adaptive remeshing the initial mesh becomes distorted after a certain length of cut as shown in Figure (1- b) and is remeshed in this vicinity to form a regular mesh again. In simulations with DEFORM-3D there is no separation criterion defined and then chip formation is assumed to be due to plastic flow. Therefore, the chip is formed by continuously remeshing the workpiece. The upper part of mesh, which constitutes of the removed workpiece material, is finer, to enable the stress, strain, strain rate and temperature in the chip and the tool tip regime to be accurately predicted. In the present work the mesh style of workpiece taken shown in Figure (1-c) which consists of about 9680 three-nodded plane-strain triangular elements. Dimensions of the element size can range from the minimum value of 0.065mm to maximum one of 0.525 mm**.**

The entire cutting process is simulated, i.e. from the initial to the steady state

phase. The workpiece material of choice, AISI 1045 carbon steel, is modeled as thermo elastic-plastic and the friction between the tool and chip is of Coulomb type with the . value of 0.5.The three-dimensional energy equation for the whole cutting domain including workpiece, chip and tool is solved numerically and the model requires the heat generation as an input.

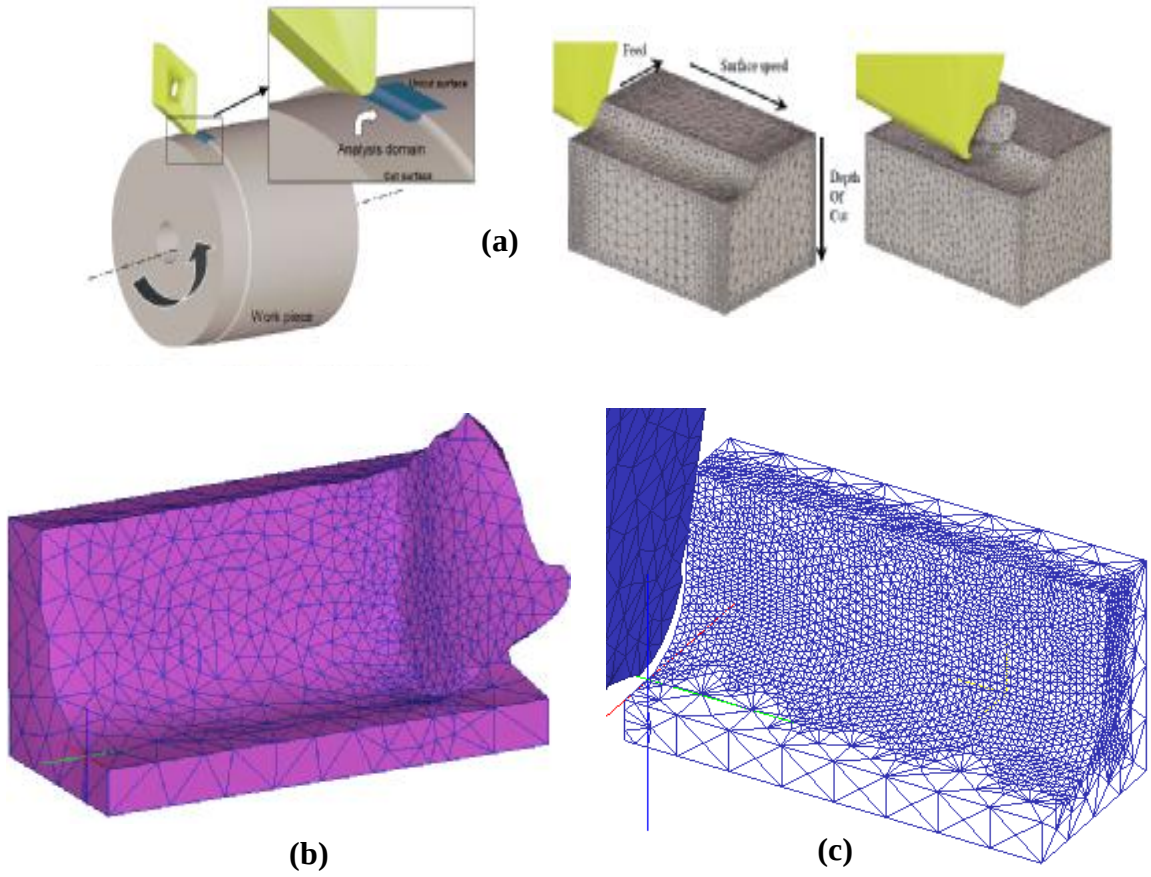

Figure(1).(a) Simulation model of the turning process used .
(b). Shape of the deformed chip after a tool path of 4.01mm .
(c) .Representation of mesh used.

2.2. Heat generation model

As a first approximation, it can be assumed that all of the mechanical energy associated with cutting or chip formation is converted into thermal energy. The heat generation is estimated based on the measured shear stress and shear strain rate relations[16].

Assuming that the work of deformation is the energy converted into thermal energy, the rate of heat generation per unit deformed volume is in primary zone expressed as:

$$\dot{Q} = \tau \dot{\gamma} = \sigma \dot{\varepsilon} \quad (1)$$

where the stress σ and the strain rate $\dot{\varepsilon}$have to be estimated from the experimental data or relations. τ is the shear stress, $\dot{\gamma}$ is the shear strain rate.

While the heat generation rate per unit volume at any point in the secondary zone is [16].

$$q_s = \tau_s \dot{\gamma}_s \quad (2)$$

2.3. Heat Transfer

The heat generated in the shear zones and at the rake face is dissipated in the chips and workpiece by conduction and lost to the ambient by convection. The governing equation for three-dimensional transient heat conduction is given as [17]

$$\frac{\partial^2 T}{x^2} + \frac{\partial^2 T}{\partial y^2} + \frac{\partial^2 T}{\partial z^2} + \frac{q}{k} = \frac{1}{\alpha}\frac{\partial^2 T}{\partial t^2} \quad (3)$$

which is subject to the following boundary conditions:

$$-k\frac{\partial T}{\partial n} = hc(T - T\infty) \quad (4)$$

Where T,q and t are temperature, heat generation per unit volume and time respectively. T_∞ ambient temperature which taken equal to 20℃, κ ,α are the thermal conductivity and the thermal diffusivity values for the workpiece, respectively, and h_c convection film coefficients for the different surfaces have been arrived at by using the standard correlations for free convection and boiling for horizontal, vertical and inclined surfaces. Figure (2)shows the heat generation and different convective conditions used on different surfaces of the model.

2.4. Cutting conditions

The tool geometry and the cutting conditions used for the orthogonal metal cutting simulation are presented in Table (1), based on the data used by[18].

Table (1) . Cutting conditions and tool geometry.

Tool rake angle = -5°	Depth of cut = 0. 5, 1, 1.5, 2, 3 mm
Tool clearance angle = 5°	Cutting speed = 103.2 m/min
Undeformed chip thickness = 0.16 mm	Coulomb friction coefficient = 0.5

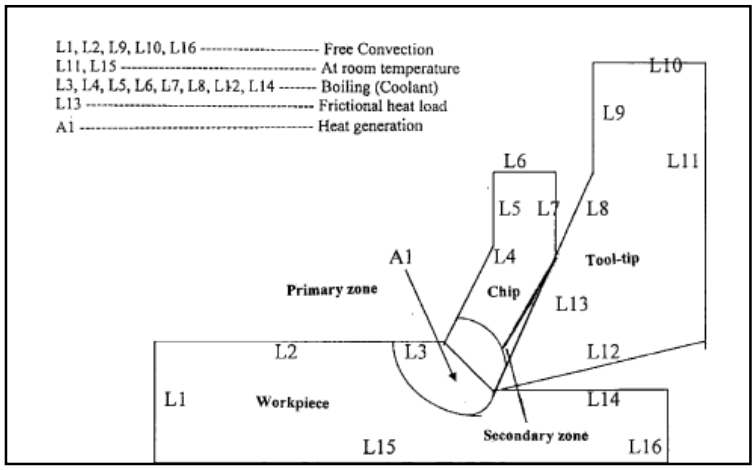

Figure(2). Heat source and boundary conditions for the model [16].

3. Results and discussion

3.1 Verification of the constructed model

To validate the predicted results obtained from the present constructed finite element model, it is necessary to compare these results with those of other authors.

3.1.1 Case 1:Dscribes temperature distribution in the cutting zone

This validation case shows the temperature distribution in the cutting zone i.e the tool-chip interface, were carried out for constant cutting parameters, i.e. cutting speed of 103.2 m/min, feed rate of 0.16 mm/rev and depth of cut of 2 mm. All cutting conditions, including tool's geometrical features, listed in Table (1)were chosen based on the data used in Ref.[18].

The temperature distribution in the workpiece and chip after a tool path of 4.0 mm, is shown in Figure (3). The temperature distribution predicted by present work with a maximum temperature of 702 °C at the tool-chip interface, is shown in Figure (3-a), while Figure (3-b) shows the simulated results predicted by Reference[18] with a maximum temperature of 680 °C,(error 3.23%) which means there is good agreement between the two results.

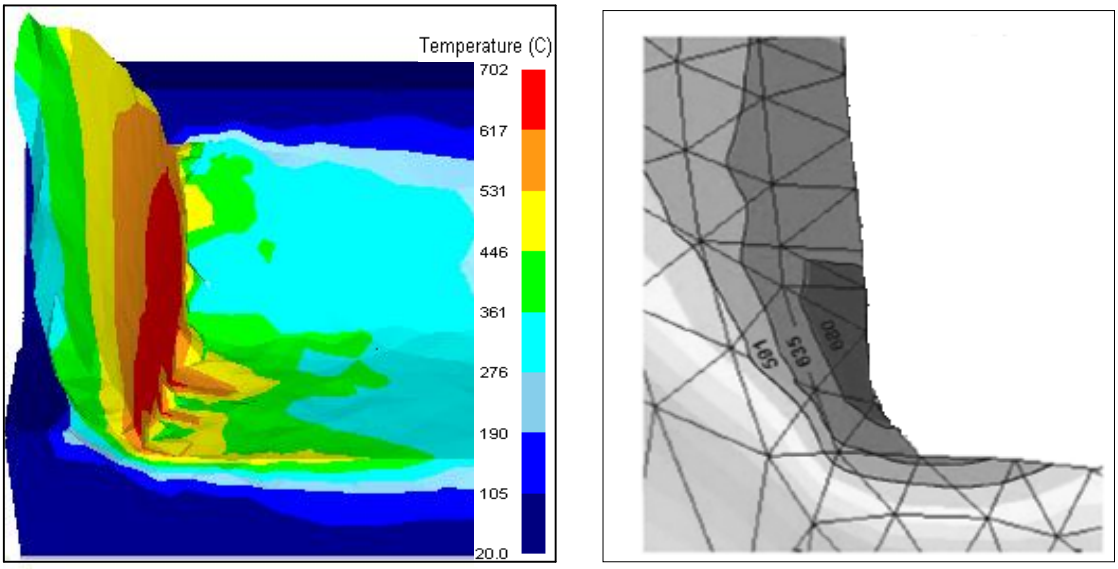

(a) (b)

Figure (3). Comparison between computed values of the interface temperature and reference [18].

3.1.2 case 2: Temperature distribution versus simulation Time

Figure(4) shows the relationship between maximum temperature in the tool-chip interface with time predicted by present work compared with numerical results predicted by Ref.[14] using same conditions given in ref.[14]. The comparison shows that there is good agreement with maximum percentage error of 2.06% in the mean temperature after reaching steady state.

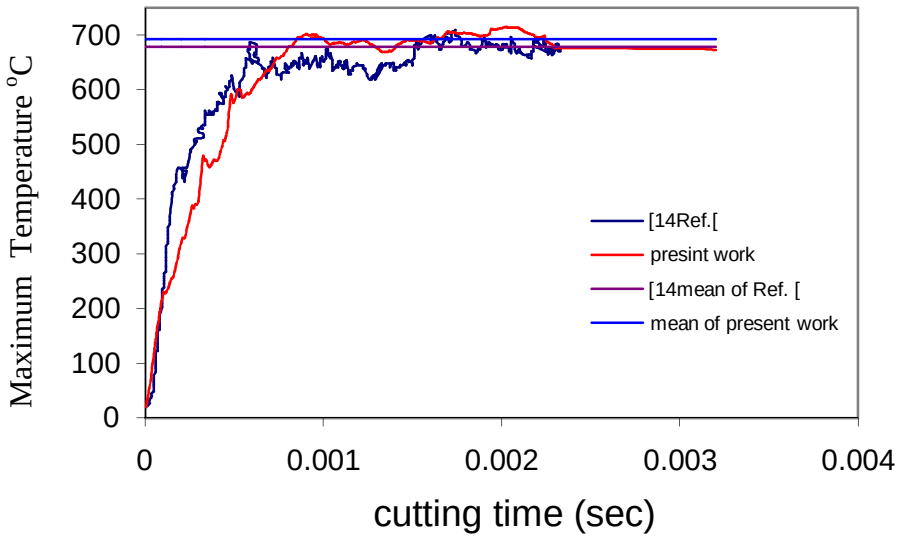

Figure (4). Average interface temperature trace vs. simulation time.

3.2 Temperature distribution

The results obtained from the application of cutting conditions involved in this work refers to the temperature distribution which depends on the depth of cut, cutting time and the position of the nod from the chip. These results can be arranged in the following manner:

3.2.1 Temperature behavior versus time

From the comparison among Figure (5a, b and c) for a depth of cut 2mm, we can be observed that more heat is transferred to the chip and workpiece and areas with the maximum temperatures are localized near the tool-chip interface. In consequence, the maximum interface temperature exists in the vicinity of the cutting edge. i.e. in the first part of the tool-chip contact and then start cooling immediately when the tool across this region. So to study this behavior, different nodes were taken in different position as show in Figure(6), where these nods coordinates are A (-0.917,0.133 ,0.990), B (-0.959 ,1.310 ,0.990), C (-0.970,2.450,1.030) and D(-0.962, 4.5,1.020).

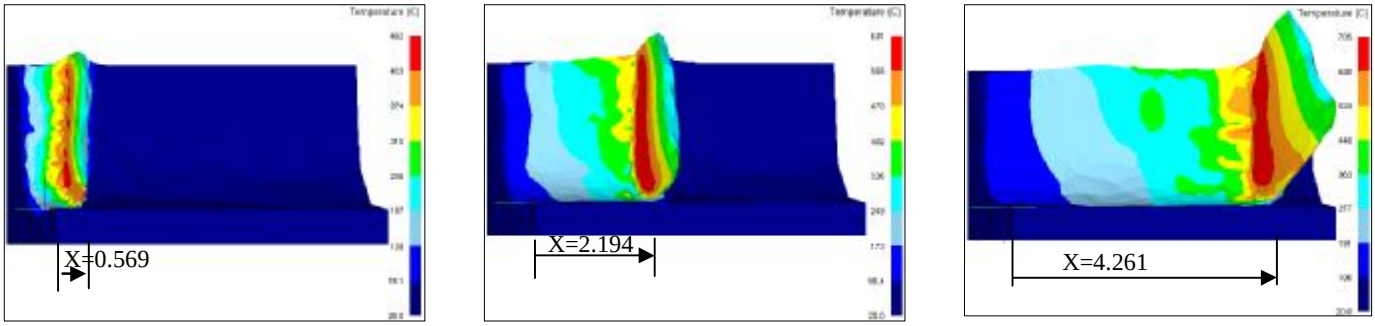

(a) (b) (c)

Figure(5). Temperature behavior with cutting tool progress(a) cutting time 39E-5sec. (b) cutting time 12E-4sec .(c) cutting time 24E-4sec .

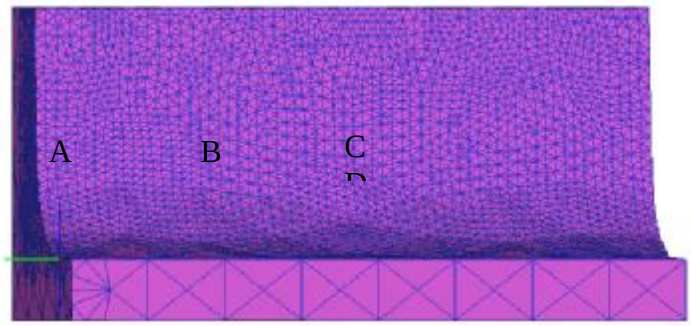

Figure (6). Node position on the work piece.

The temperature variation in these nodes with time during cutting process was illustrated in Figure(7) .It is clear that all nodes obey the same behavior although the maximum temperature at each one not equal. The temperature at node D reach a maximum value 621.4 ̊. C compared with nodes A, B and C. This can be concluded to the heat transfer by conduction through the workpiece at node D, which is accumulated from the other nodes. Figure (8) shows that there are raising in temperatures in the region ahead the chip on the workpiece due to conduction.

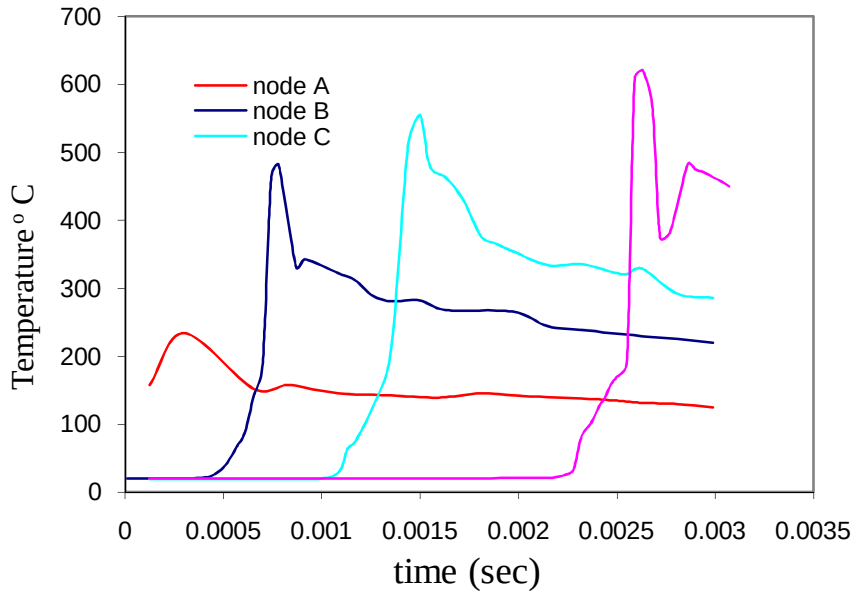

Figure (7) . Temperature distribution with time for different location.

Also the difference in the value of temperature increase among the nodes A, B,C, and D is not constant and reduce with time until reach an alternating range. This result agree with the result shown in Figure (9).

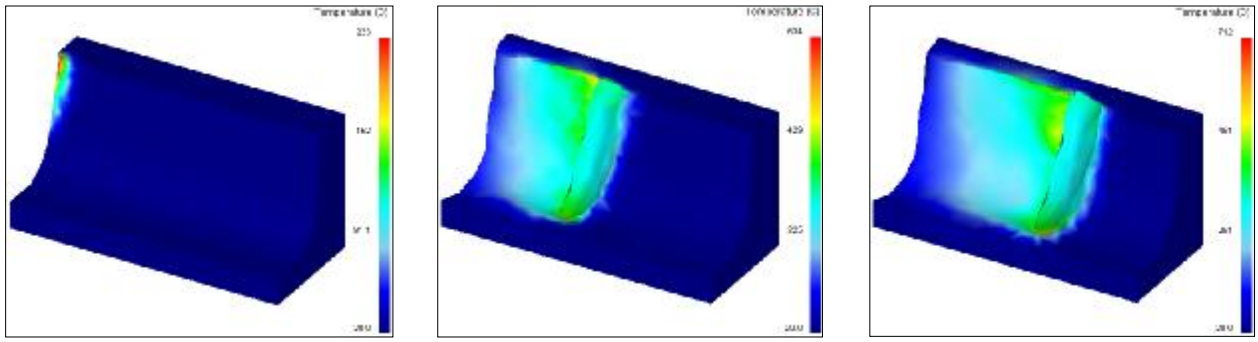

(a) **(b)** **(c)**

Figure (8). Regions of rising tempertures before reach cut to them.

3.3. Cutting temperature

3.2.2 Cutting temperature

The appropriate temperature histories obtained during simulations along with corresponding values of the maximum workpiece temperatures are shown in Figure (9). It was established based on temperature traces with tool travel that the time required to reach the steady-state temperature was approximately 0.65ms. As can be seen from these records, the value of mean temperature are reach to close values (reach steady state) and this explains why the temperature dose not continue to raise.

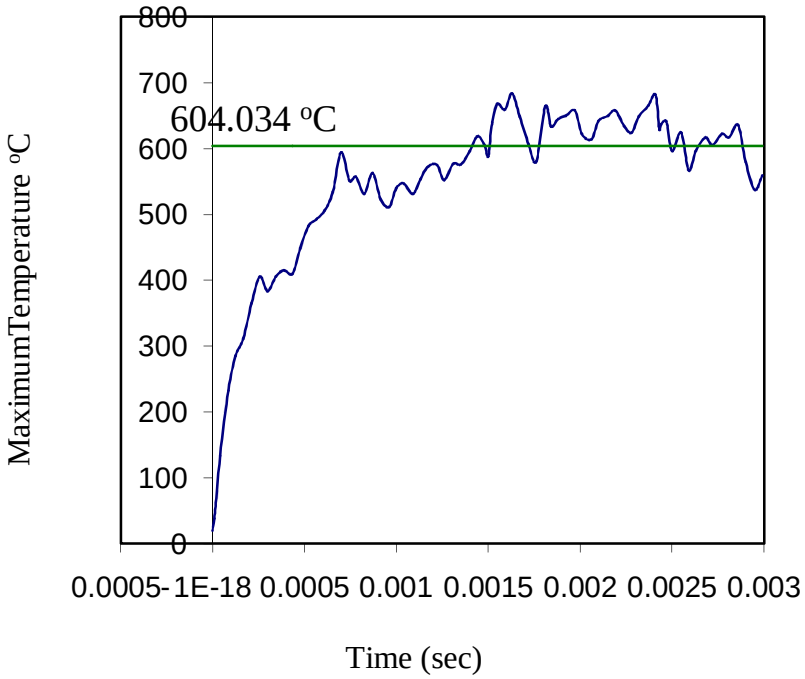

Figure (9) . Relation between maximum temperature and time.

3.3 Temperature variation with depth of cut

Behaviour of temperature differs from the value and the distribution form for the same location and time (same boundary conditions) in the cutting direction with the depth of cut, the maximum temperature for depth of cut 0.5mm reaching a 622˚C while its reaching 708℃ for depth of cut 2mm. As the depth of cut increase the area with high temperature increases, see Figure (10), and the rise of temperature not limited in cutting zone only, but contain the vicinity regions for the cutting depth (at the top of workpiece) that's belongs to heat conducting which the temperature rise from 221°C to 249°C at depths 0.5mm and 2mm respectively.

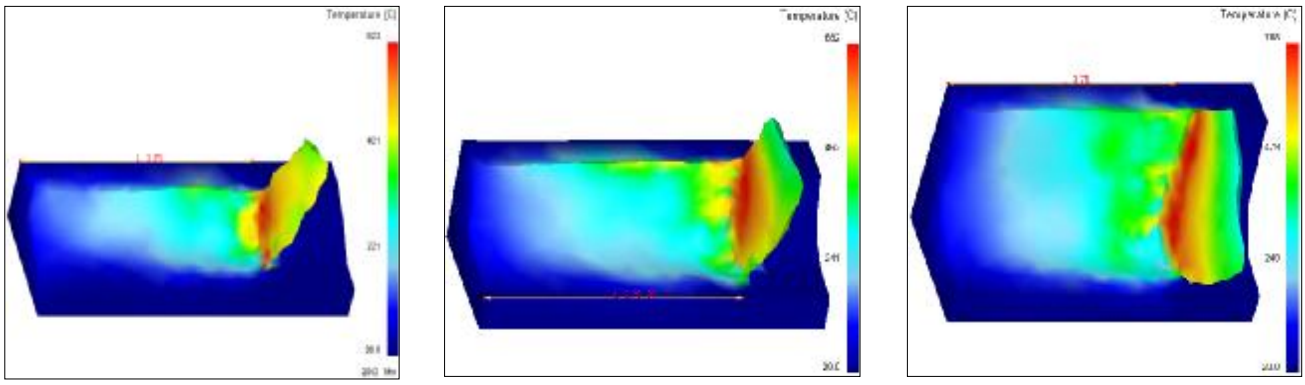

(a) **(b)** **(c)**

Figure(10). Temperature behaviour with different depth of cut. (a) t1=0.5mm, (b) t1=1mm, (c) t1=2mm (c)t1=2mm.

Temperature hysterias obtained during simulations along with corresponding values of the average workpiece temperature for different depth are shown in Figure (11). Based on temperature traces with tool travel that the time required to reach the steady-state temperature was depending on the depth of cut . For 0.5 mm reach to steady faster than other depth approximately at time0.228ms while it was 0.564 and 0.65msec for 1mm and 2mm respectively . As can be seen from these records, the value of mean temperature are reach to close values (reach steady state) in a time has an inverses relation with depth of cut. Figure (12) shows temperature course for same nod has a position of (-0.96, 2.51,0.95) with time for different depth of cut ,this figure insure the relation between temperature and depth of cut. That temperature increasing with increase depth of cut , this belong to increase the cutting force cutting (cutting work) to overcome the friction ,since with increasing depth of cut means cutting more amount of the cutting metal and all this work convert to heat.

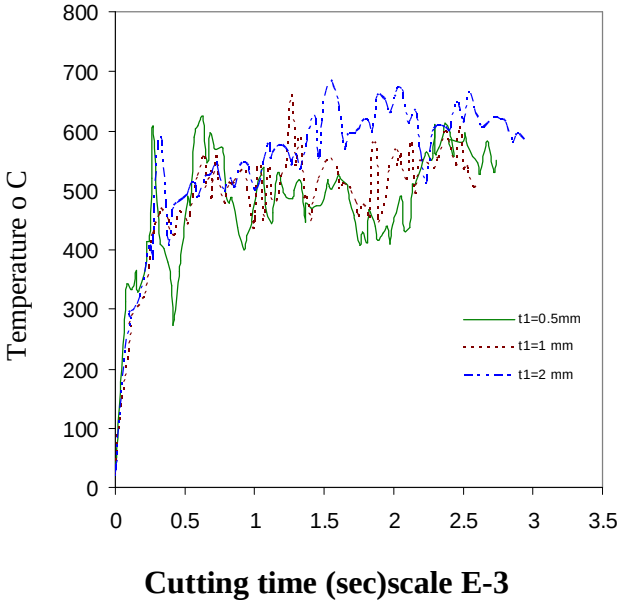

Figure (11). Interface temperature trace vs. cutting time for different depth.

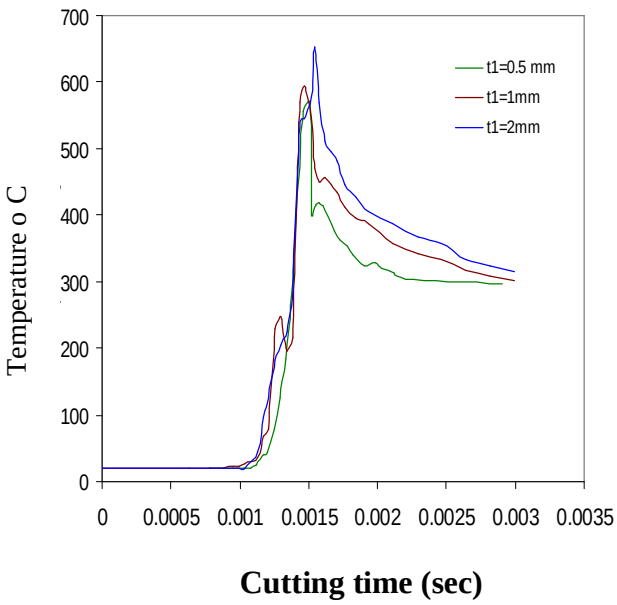

Figure (12) . Temperature vs. time at different depth of cut for the same position.

Temperature distribution in a direction perpendicular to the cutting direction at different depth of cut and 4mm distance from the cutting edge was illustrated in Figure (13). The region ahead the cutting edge which represented in Figure (13- a), it can be noticed that region is small at depth t1=0.5mm and increase with increasing the depth of cut, this mean that the region which expose to heat transfer by conduction increase with the depth of cut. The cooled region areas reduce with increase the depth of cut see Figure (13-b). Also the results show that the regions with high temperature in all depths appears at distance 0.1 to 0.25 mm from the cutting edge .While regions of high temperature (340 to 450) disappear only for depth 0.5mm after 1mm from the cutting edge. The fast reduction in temperature leads to increase the area of low temperature region (101 to 182)˚C for depth 0.5, and (103-186)^{o}C for depth of cut 1mm as shown in Figure(13- f) and Figure (13- g) .

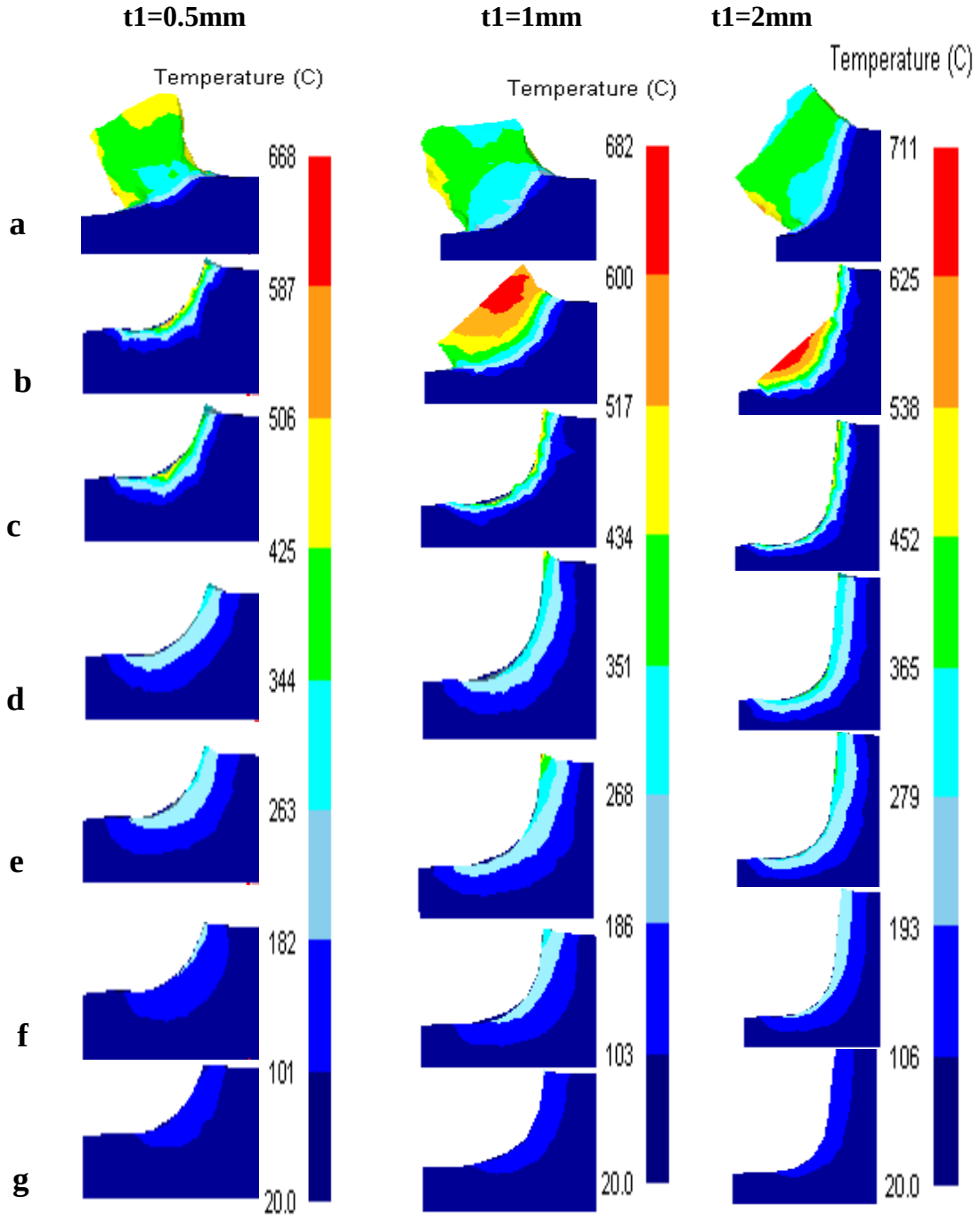

Figure(13). Magnification of temperature distribution on the depth of workpiece after a tool path of 4.0mm for t1=0.5mm ,t1=1mm ,t1=2mm and different positions a)4.3mm b)3.93mm c)3.75mm d)3mm e)2.5mm f)1.5mm g)0.57mm from starting cutting.

4. Conclusions

The aim of this finite element modeling was creating a FEM simulation model in order to obtain and research: numerical solutions of cutting forces, temperature in the contact region and workpiece material and plastic strain during turning the steel.

The following conclusions may be drawn from the results of this work:

1. The results obtained from the present work verify that the cutting process could be numerically estimated using the finite element method with a reasonable degree of accuracy.
2. The maximum temperature exists in the vicinity of the cutting edge. i.e. in the workpiece then start cooling immediately when the tool across this region.
3. The maximum temperature in the workpiece increases as the cutting time increase until process reach the steady-state condition where the temperature alternating around the mean temperature.
4. Behaviour of temperature differs in value and distribution for the same location and time (same boundary conditions) in the cutting direction with the change in depth of cut. The maximum temperature occurs at maximum depth of cut certainly this belong to increase the cutting force (cutting work) to overcome the friction.
5. The temperature for all nodes obey the same behaviour through cutting processes, although the maximum temperature (when the tool reach to theses nods) at each one not equal.
6. Temperature histories obtained during simulations along with corresponding values of the maximum workpiece temperature for different depth. based on temperature traces with tool travel that the time required to reach the steady-state temperature was depending on the depth of cut, as well as the value of mean temperature are reach to close values (reach steady state) in a time has an inverses relation with depth of cut.
7. Temperature distribution inside workpiece (perpendicular on the cutting direction) at different depth of cut represent by regions(which previous the cutting , region which expose to heat transfer by conduction) which limited at depth t_1=0.5mm and increase with increasing the depth of cut.
8. It can also be important for practice that the maximum interface temperatures predicted can support the choice of depth of cut for defined machining parameters in order to avoid excessive thermal loading on the workpiece.

5.Acknowledgements

The authors wish to thank Prof. Dr. ABDUL KAREEM FLAIH HASSAN, Department of Mechanical Engineering of the University ofBasrah for his continuous and qualified support in the preparation and development for this research.

6. References

[1] Mitrofanov A.V., Babitsky V.I. , and Silberschmidt V.V., 2004,"Finite Element Analysis of Ultrasonically Assisted Turning of Inconel 718", Journal of Materials Processing Technology,153–154,233–239 .

[2] Abukhshim N.A., Mativenga P.T. , and Sheikh M.A. , 2006,"Heat Generation And Temperature Prediction in Metal Cutting: A Review and Implications For High Speed Machining", International Journal of Machine Tools & Manufacture 46 , 782–800.

[3] Sarat B. S., 2005,"A Mixed Solution for the Three-Dimensional Temperature Distribution in Turning Inserts Using Finite and Boundary Element Techniques “,Journal of Materials Processing Technology, 166, 98–106.

[4] Chung-Shin C.,2007," Prediction of the Cutting Temperatures of Stainless Steel with Chamfered Main Cutting Edge Tools ", Journal of Materials Processing Technology 190 , 332–341.

[5] Vincent D. , Shreyes N. M. and Christophe L., 2004," Modeling and Verification of Cutting Tool Temperatures in Rotary Tool Turning of Hardened Steel", International Journal of Machine Tools &Manufacture 44, 1463–1470.

[6] Abhang L.B. , Hameedullah M.,2010,"Chip-Tool Interface Temperature Prediction Model for Turning Process", International Journal of Engineering Science and Technology Vol. 2(4), 382-393.

[7] Shijun Z. , Zhanqiang L.,2008,"An Analytical Model for Transient Temperature Distributions in Coated Carbide Cutting Tools", International Communications in Heat and Mass Transfer 35,1311–1315.

[8] Ranga K., Zhen B. H., 2001,“Thermal Modeling of the Metal Cutting Process Part II: Temperature Rise Distribution Due to Frictional Heat Source at the Tool-Chip Interface”, International Journal of Mechanical Sciences, 43, 57-88.

[9] AttiaM. H., Kops’ L. (1) "A New Approach to Cutting Temperature Prediction Considering the Thermal Constriction Phenomenon in Multi-layer Coated Tools" ,Institute for Aerospace research, National Research Council Canada.

[10] Yvonneta J., Umbrellob D., Chinestaa F., and Micaric F. ,2006," A Simple Inverse Procedure to Determine Heat Flux on the Tool in Orthogonal Cutting", International Journal of Machine Tools & Manufacture 46 , 820–827.

[11] Recha J., Kusiakb A. , and Battaglia J.L., 2004," Tribological and Thermal Functions of Cutting Tool Coatings", Surface & Coatings Technology ,186,364– 371.

[12] Grzesik W., Niesony P., February 2008," FEM–Based Thermal Modelling of the Cutting Process Using Power Law Temperature Dependent Concept", Archives of Materials Science and Engineering , 29,No. 2,Pages 105-108.

[13] Bunga G., Gutakovskis V., Niemi E. and Laakso S. ,"Finite Element Method Modeling of the Stainless Steel Cutting Process Using Different Machining Parameters"

[14] Grzesik W., Bartoszuk M. and Nieslony P.,2005,"Finite Element Modelling of Temperature Distribution in the Cutting Zone in Turning Processes with Differently Coated Tools", Journal of Materials Processing Technology 164–165,1204–1211.

[15] Umbrello D., Filice L., Rizzuti S., Micari F. and Settineri L., 2007," on the Effectiveness of Finite Element Simulation of Orthogonal Cutting with Particular Reference to Temperature Prediction", Journal of Materials Processing Technology 189 , 284–291.

[16] Majumdar P., Jayaramachandran R. and Ganesan S.,2005," Finite Element Analysis of Temperature Rise in Metal Cutting Processes", Applied Thermal Engineering 25 , 2152–2168.

[17] Abukhshim N.A., Mativenga P.T. and Sheikh M.A., 2005,"Investigation of Heat Partition in High Speed Turning of High Strength Alloy Steel", International Journal of Machine Tools & Manufacture 45, 1687–1695.

[18] Grzesik W., Bartoszuk M. and Niesłony P., 16th- 18th May,2005,"Finite Element Modelling of Temperature Distribution in the Cutting Zone in Turning Processes with Differently Coated Tools", worlawide congress on materials and manufacturing engineering and technology,Gliwice- Wista, Poland.

Temperature Rise in Al 7075 Cold Wire Drawing Using Finite Element Method

Hassanein I. Khalaf
Mechanical Engineering Dep.
College of Engineering
University of Basrah

Zainab K. Radhi
Mechanical Engineering Dep.
College of Engineering
University of Basrah

Sanaa M. Shrama
Mechanical Engineering Dep.
College of Engineering
University of Basrah

Abstract

In this work the temperature rise in AL7075 wire drawing is predicted numerically using a 3D finite element model. The commercial code Deform-3D was used to construct the model and simulate the wire drawing process. Aluminum wire of 46.38mm was drawn at room temperature through a conical die with semi-die angle $\alpha=5^{\circ}$ and percentage reduction in area equal to 10%. This case was run for different values of friction coefficient (μ=0.05, 0.075, 0.1, 0.125, 0.15, 0.175, 0.2). The result shows that as the coefficient of friction increases, the temperature rises in linear form. The behavior of temperature rise distribution is studied in details for μ=0.1, for this case the temperature rise in wire during the drawing process is ($22.3C^{o}$) less than in die ($28.7C^{o}$), also the location of maximum temperature in the die occurs at the contact area before wire exit from the die.

المستخلص

في هذا البحث تم دراسة توزيع ارتفاع درجات الحرارة عدديا" لسلك من الألمنيوم نوع (AL 7075) . تم بناء نموذج عناصر محددة ثلاثي الأبعاد باستخدام الحقيبة البرمجية الجاهزة Deform-3D لسحب سلك من الألمنيوم ذو قطر (46.38 mm) داخل قالب مخروطي نصف زاويته ($\alpha = 5°$) وبنسبة تقلص في المساحة (10%). هذه الحالة نفذت عند قيم مختلفة من معاملات الاحتكاك (μ=0.05, 0.075, 0.1, 0.125, 0.15, 0.175, 0.2). أظهرت النتائج بأن زيادة معامل الاحتكاك يؤدي إلى زيادة الارتفاع في درجات الحرارة بصورة خطية. سلوك توزيع درجات الحرارة خلال عملية السحب درس بصورة تفصيلية عند قيمة معامل احتكاك (μ= 0.1). أوضحت نتائج هذه الحالة أن أقصى ارتفاع لدرجة حرارة السلك أثناء عملية السحب بلغ (22.3°C) وهو اقل من القالب الذي كان أقصى ارتفاع لدرجة حرارته (28.7°C). أن موقع درجة الحرارة العظمى كان في القالب وبالتحديد في المنطقة القريبة من منطقة الخروج.

1. Introduction

In the wire-drawing process, the cross-section is reduced by pulling it through a conical die, as shown in Figure (1-a). The major variables affecting the drawing process are reduced in cross-sectional area, die angle, friction along the die–work piece interfaces and drawing speed. For a successful drawing operation, careful selection of process parameters should be carried out. The drawing speed depends on the wire material as well as the required reduction in area [1].

There have been many investigators who studied the wire drawing process. Vega et al.[2] investigated the effect of the process variables such as semi die angle and reduction in area, and the coefficient of friction on the drawing force value. For the wire, elasto-viscoplastic behavior is considered, while the die material is assumed to be elastic. Two types of dies have been used in this work: crystal mono diamond core (MD) and crystal poly diamond (PCD). They indicate that friction has significant effects on the drawing force which decrease with the decrease of area reduction. The optimum die angle for wire drawing is assumed to be obtained when the plastic strain distribution across the diameter of the wire becomes uniform. H. Verstam [3] studied the influence of bearing geometry on the residual stress-state in cold drawn wires. The material used was a high carbon steel for roller bearings, 100Cr6. He found that the geometry of the bearing has a large influence of the residual stress-state. Hoon Cho[4] considered the reduction ratio with the size of an inclusion, application of back tension and distance between inclusions in order to investigate the effect of back tension on wire breaks. The size of an inclusion varies 5, 7 and 10 mm, the reduction ratio varies 10, 13 and 16%, the distance between inclusions is set to be 0.25 and 0.5 mm, respectively. Conical dies with a half angle a of 78, which is the value generally used in commercial production. As the FEM code, the commercially available software DEFORM-2D is used. Copper is used for fine wire drawing process that initial diameter is 1 mm and final diameter is up to 50 mm. They found that the damage value rises because the tensile stress in deformation zone increases by applied back tension. The distance between inclusions would not affect wire breaks because the distance is expanded excessively through multistage wiredrawing.

Lucca and Wright [5] discussed the assumptions which might be taken into consideration in predicting the temperature rise resulting from frictional heating in wire-drawing.

The magnitude and the distribution of temperature in the wire-drawing process depends on the initial temperature of the material and die, heat generation due to plastic deformation and friction at the die-material interface and heat transfer between the deforming material, the die and the surrounding environment, such as lubricant and air. The frictional heating however, is concentrated near the wire die interface at the die exit and results in the development of a severe temperature gradient. McAllen[6] and Vega [7] studied the influence of forming conditions and show that , the smaller the die angle, the longer is the contact length, and the size and depth of the deformation zone increase with increasing contact length . Die wear, which occurs at the approach and bearing surfaces due to frictional and heating effects, can rapidly diminish tool life as the work piece is frequently formed at an elevated temperature, superior lubrication is required at the die-wire interface [8].

In this work the commercially available finite element method code software DEFORM-3D is used to obtain the stresses, strains, strain rates and temperature distribution in wire during the drawing process. The material selected to carry out this analyses was an aluminum alloy Al7075, the properties of wire materials at room temperature is given in Table (1). The main object of the present study is to simulate the temperature distribution in wire and die

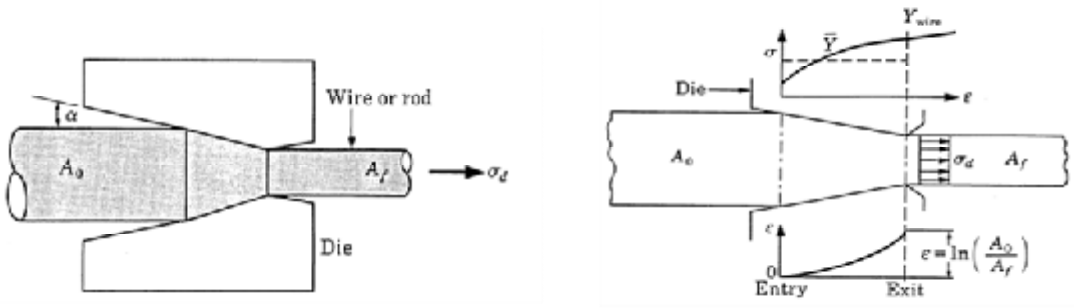

(a (b

Figure(1). Parameters in the Wire-Drawing, [1].

during the drawing process.

2.Theory of wire drawing

Assuming that plastic deformation work is completely converted into heat and that no heat loss occurs, the temperature rise in the wire is given by[1]:

$$\Delta T = \frac{W_{tot}}{\rho c} \quad (1)$$

The temperature rise given by Eq. (1) is for an ideal situation, where there is no heat loss. In the actual wire-drawing process, heat is lost to the environment, tools and dies, as well as to lubricants and coolants. The total energy per unit volume W_{tot} can be calculated as [1]:

$$W_{tot} = \int_0^{\varepsilon_{1f}} \frac{K\varepsilon_1^n}{(n+1)} f(\mu,\alpha,r)d\varepsilon_1 = \frac{K\varepsilon_{1f}^{(n+1)} f(\mu,\alpha,r)}{(n+1)^2} \quad (2)$$

$$f(\mu,\alpha,r) = \left\{\left(1+\frac{\tan\alpha}{\mu}\right)\left[1-\left(\frac{A_f}{A_o}\right)^{\mu\cot\alpha}\right] + \frac{4\alpha^2}{3\sqrt{3}}\left(\frac{1-r}{r}\right)\right\} \quad (3)$$

The drawing stress,(σ_d) is given by:

$$\sigma_d = \bar{Y} f(\mu,\alpha,r) \quad (4)$$

The temperature rise at the exit section of the die can be calculated:

$$\Delta T = \left[\frac{K}{\rho c(n+1)^2}\right]\left[\left\{\ln\left(\frac{1}{1-r}\right)\right\}^{n+1}\right] f(\mu,\alpha,r) \quad (5)$$

Where:

$\varepsilon_{1f} = \ln\left(\frac{1}{1-r}\right)$,$r = \frac{A_o - A_f}{A_O}$

3. Finite element modeling of wire drawing

The code DEFORM-3D V6.1 is used to perform finite element analysis of wire drawing process in this research. This software is specifically designed to analyze bulk plastic deformation, and is especially suited for the present analysis. It takes advantage of the fact

that plastic deformation is usually highly localized. It assigns rigid elements to the regions of the part that are not deforming, thereby reducing the number of the calculations performed at each step of the simulation. It also updates nodal coordinates using a higher order scheme. This special algorithm accurately takes into account the rotation of the object when calculating new location of the draw part [9]. A 3D finite element drawing model has been constructed to simulate a single pass of wire drawing through a conical die. Due to symmetry only one quarter of the die and wire is simulated, see Figure (2). Aluminum wire of 46.38mm diameter was used as the simulated material in this work. The mechanical properties of wire material at room temperature are given in Table (1) and the valued parameters are given in Table (2).

Table(1). Mechanical properties of Al 7075, [1].

Material	***K (MPa)***	***n***	***Density ρ (Kg/m^3)***	***Specific heat c (J/Kg.K)***
Al 7075	400	0.17	2700	900

Table(2). Drawing parameters.

Wire	
Material	Al 7075
Origenal diameter	46.38mm
Final diameter	44mm
Length	160 mm
Reduction in area%	10%
Die	
Material	Rigid
Sime – die Angle	5^o
Exit Angle	3^o
Outer Diameter	80
Inner diameter	44mm
Coefficient of friction between die and wire (μ)=0.1 Drawing speed=111.7mm/s	

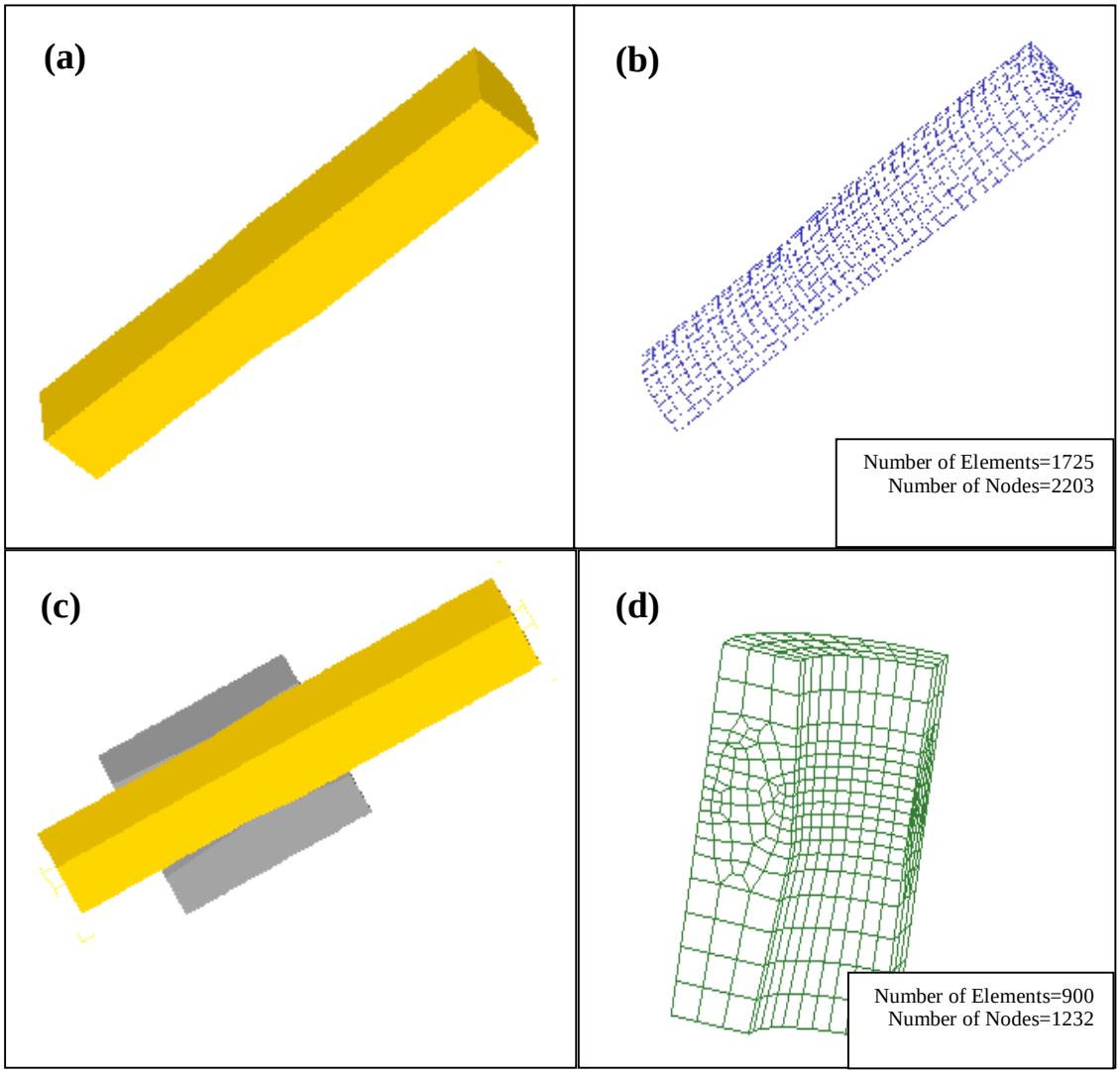

Figure(2). (a) Wire before drawing . (b) Meshed wire.
(c) Arrangement wire and die. (d) Meshed die.

4. Results and discussion

To validate the predicted results obtained from the constructed finite element model, it is necessary to compare these results with analytical or experimental data of other authors. The analytical data of El-Domiaty and Kassab,[1] was chosen to achieve this comparison.

The relationship between the temperature rise and coefficient of friction is shown in Figure (3). It is clear that the temperature rises with increase in friction coefficient. This can be concluded to the excess in the frictional work. Also it can be seen from this figure there is a good agreement between the analytical result of [1] and the finite element result of the present work with a maximum percentage error of 5.55%.

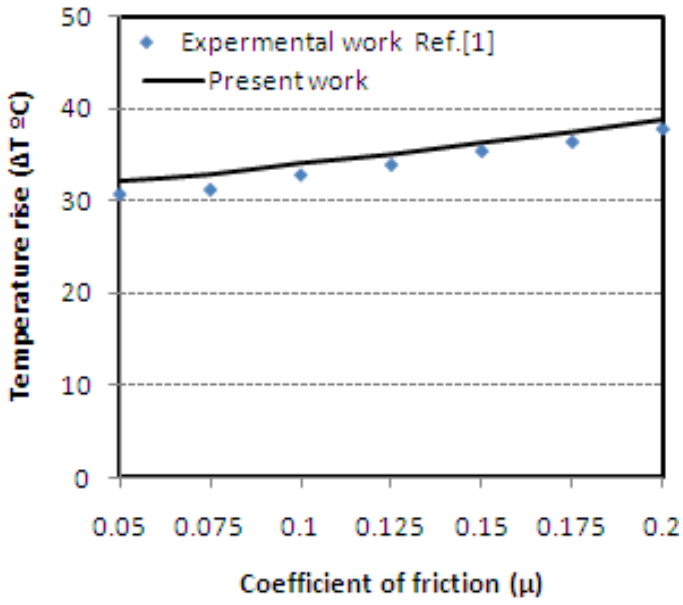

Figure (3). Comparison results of temperature rise as a function of coefficient of friction .

4.1 Distribution of effective stress, strain and strain rate

During cold wire drawing, there will always be a stress of different signs and magnitude. The effective stress, created by material flow, is one of the important types. The effective stress distribution on cross and longitudinal sections in the wire must be in equilibrium. The stress analyses can be conducted to determine stress variation in the material during the wire drawing process. These analyses are very important in the wire drawing process optimization considering low possible contact force. Figure(4) shows the stress distribution in the wire when it passes through the die. The maximum stress value is found near the surface layer of the die-bearing section and maximum stress value is 256 MPa.

A complete distribution of strain along the wire axis when its passes through the die can be observed in Figure (5).Distributions of the strain shows that the maximum value of strain occurs at the exit from the die with a value of 0.235.

Figure (6) shows the distribution of strain rate along the wire axis when its passes through the die. The maximum value of the strain rate in the deformed wire during a temperature change from 25 °C to 53.7 °C was found to be 1.67 s^{-1}.

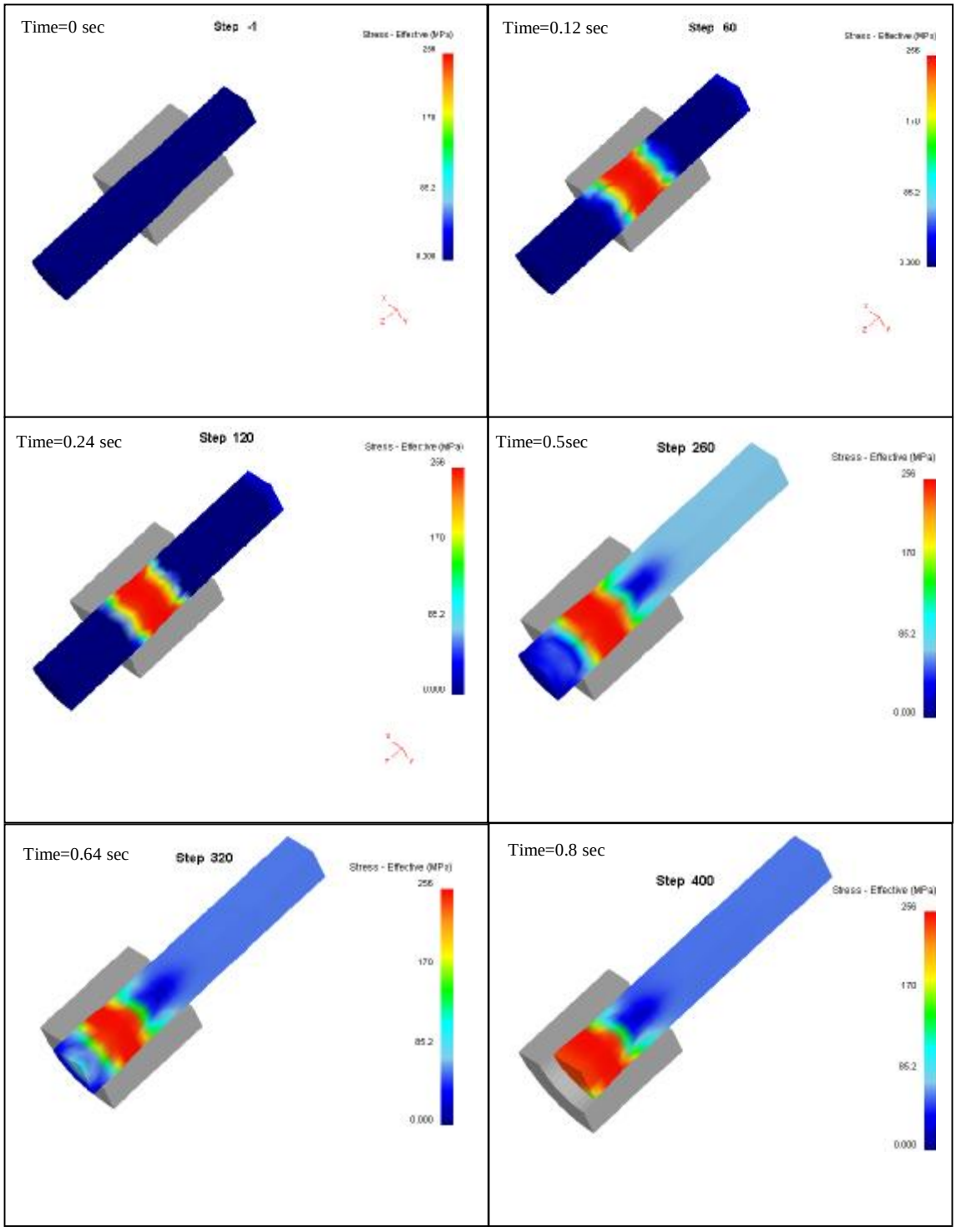

Figure(4). The contour plot of the effective stress during the drawing process.

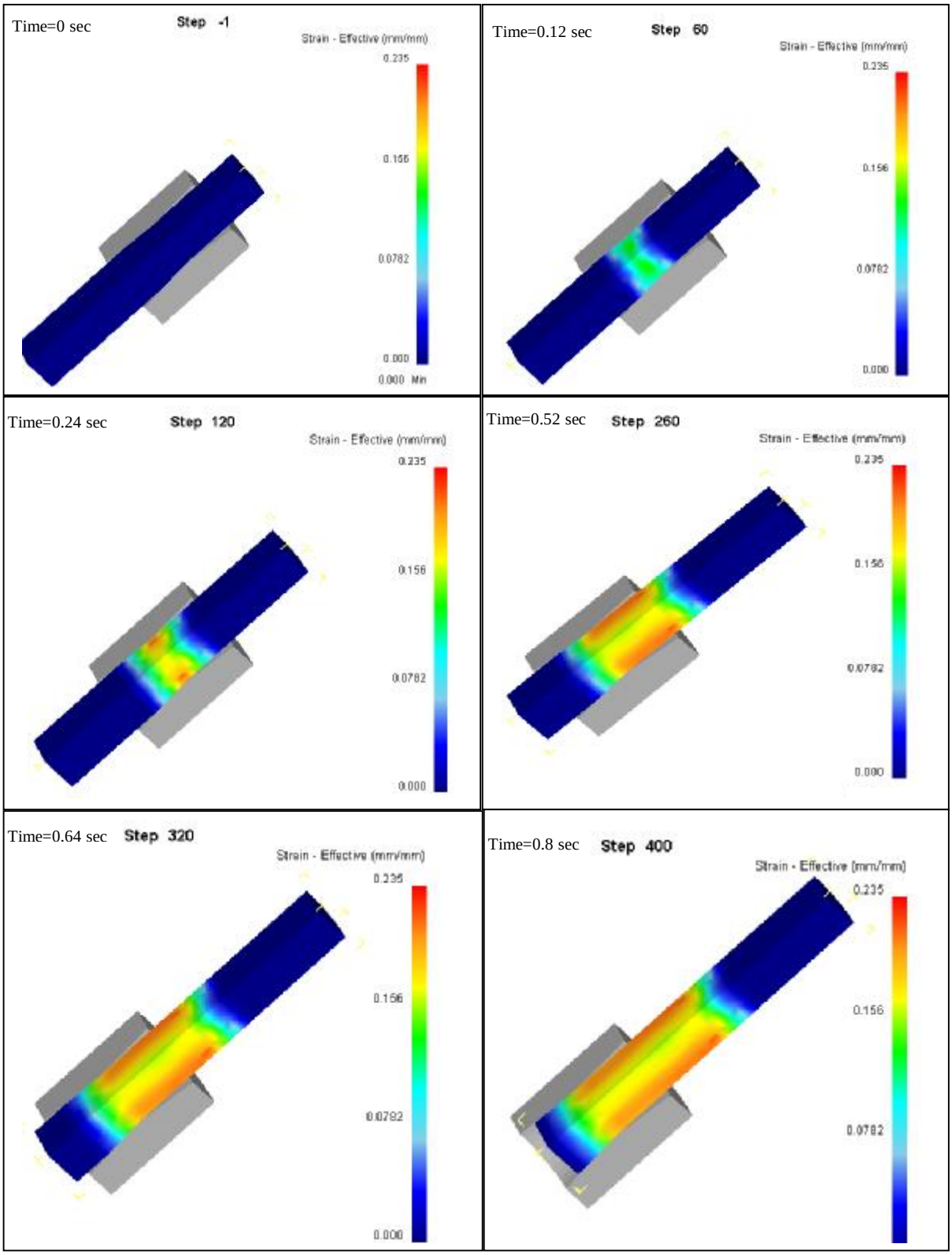

Figure (5). The contour plot of the effective strain during the drawing process.

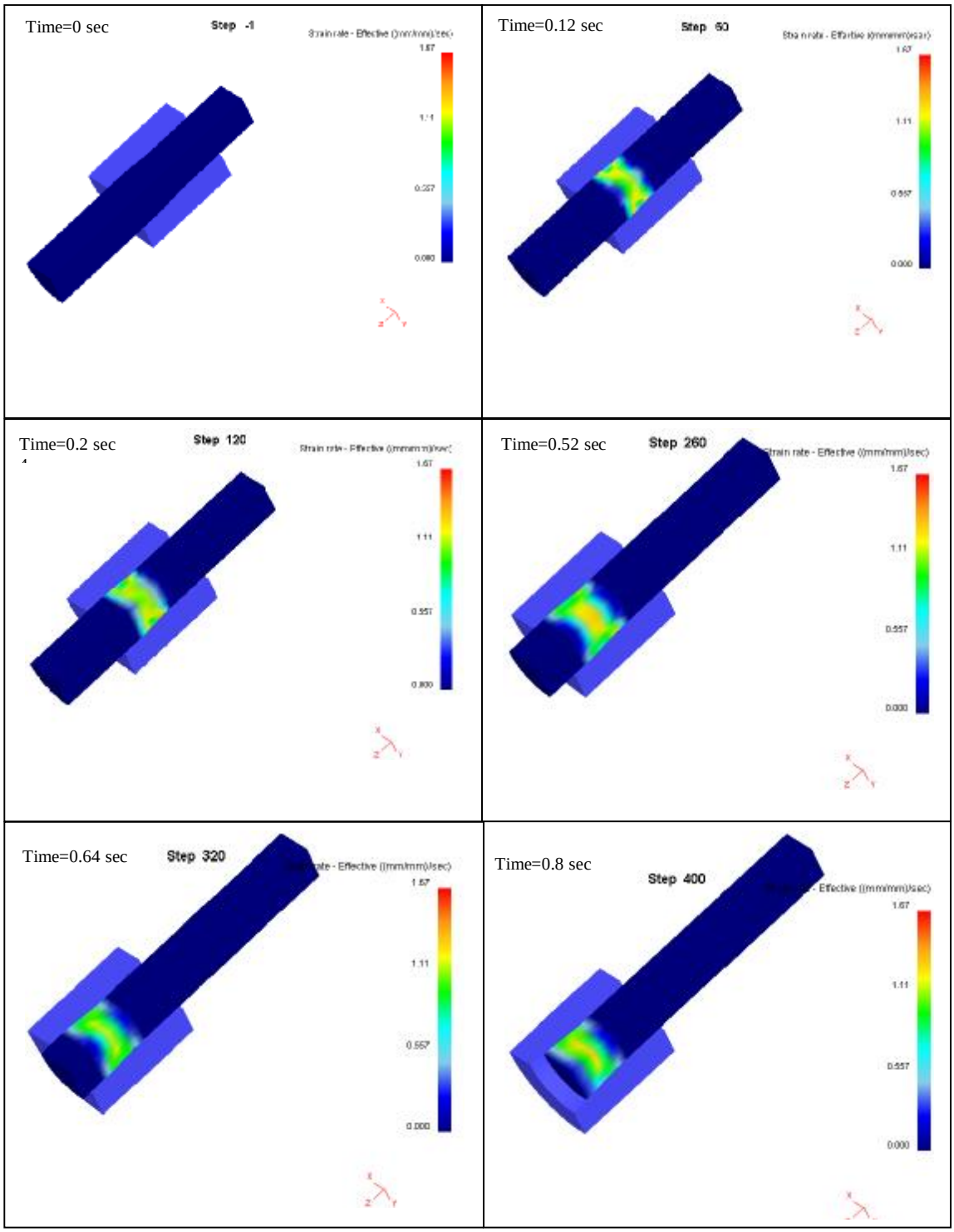

Figure (6). The contour plot of the effective strain rate during the drawing process.

4.2 Temperature evolution during cold wire drawing process

Figure (7) shows the distribution of the temperature on the aluminum *Al* 7075 wire knowing that the temperature of die and wire at the beginning of process is 25°C then the temperature rises during the process and reaches its maximum value 53.7°C in the contact area between the die and wire.

The maximum temperature rise in the wire is at the surface equal to 47.3°C, the heat transfer toward the center of the wire by conduction causes an increase in temperature at this region until it reaches to almost 35°C as shown in Figure (8). Figure (8-b) presents the temperature distribution at the center line of the wire that has been divided into three regions as shown in Figure (8-a). This figure shows that the temperature rise from room temperature at point (P1) (region after deformation) until it reaches to the maximum value almost 35° C at region (II)(during deformation) then temperature reduces until it reaches to the room temperature again at point (P12) which represents the region before deformation .

Figure (9) shows the temperature distribution from the center of the wire towards the wire surface. The temperature at the centre of the wire be almost (35°C) increases as we get closer to the surface of the wire where the highest temperature is 47.3°C

The die temperature distribution, see in Figure (10), refers to the maximum temperature which occurs in contact region between wire and die which reach 53.7 ^{o}C . The location of this value at the contact area before the wire exits from the die . This attributed to the increase in the redundant work in this region.

In order to study the temperature change with time on the wire surface, one node on the wire surface is chosen and the temperature change in this node was predicted, see Figure (11). It was noticed that as soon as the wire enters the die the temperature would be raised until it reaches its maximum value at a point close to exit zone then decreases when this point gets far from the exit zone . This behaviour was plotted in time-temperature graph as shown in Figure(12).

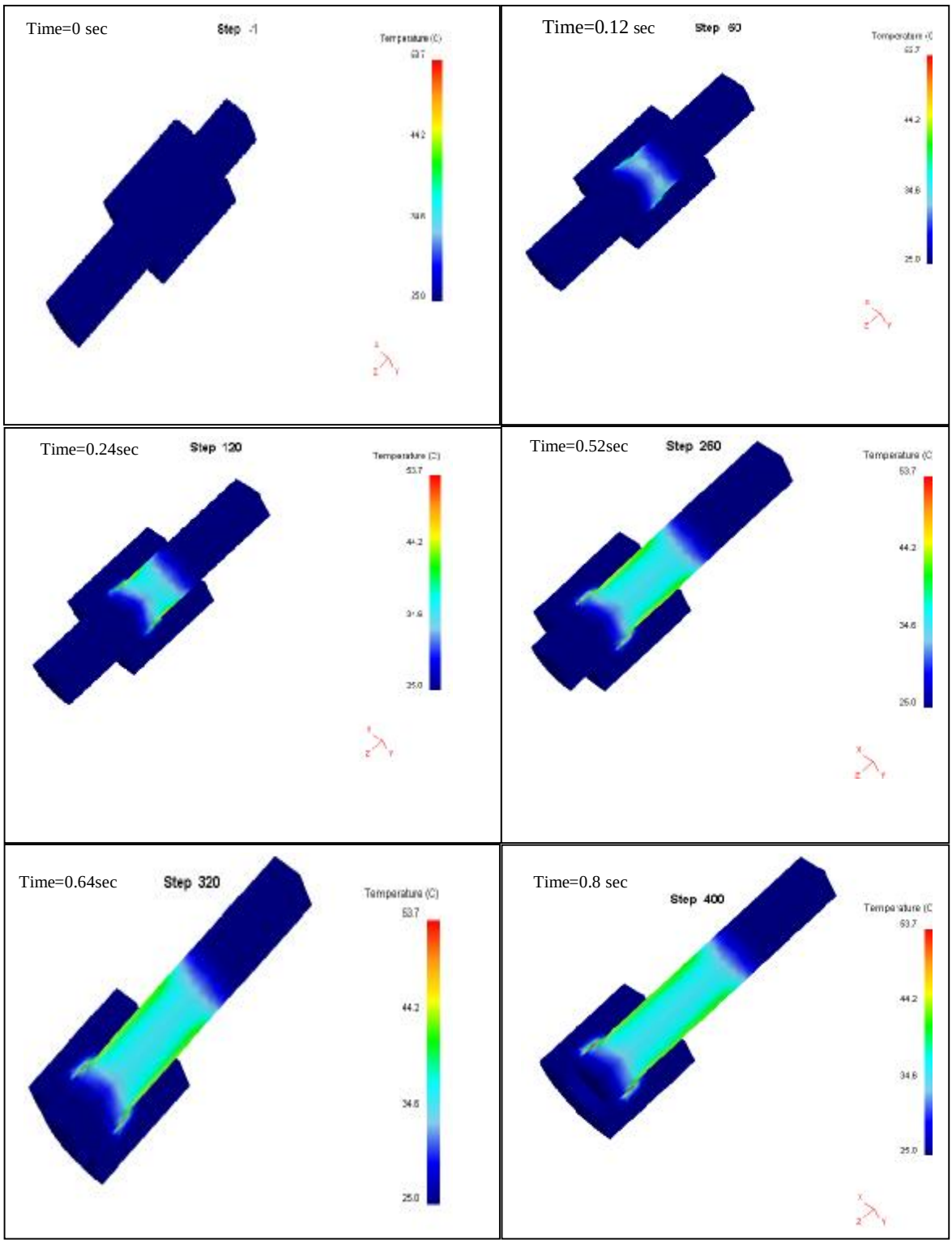

Figure(7). Temperature evolution during cold wire drawing process.

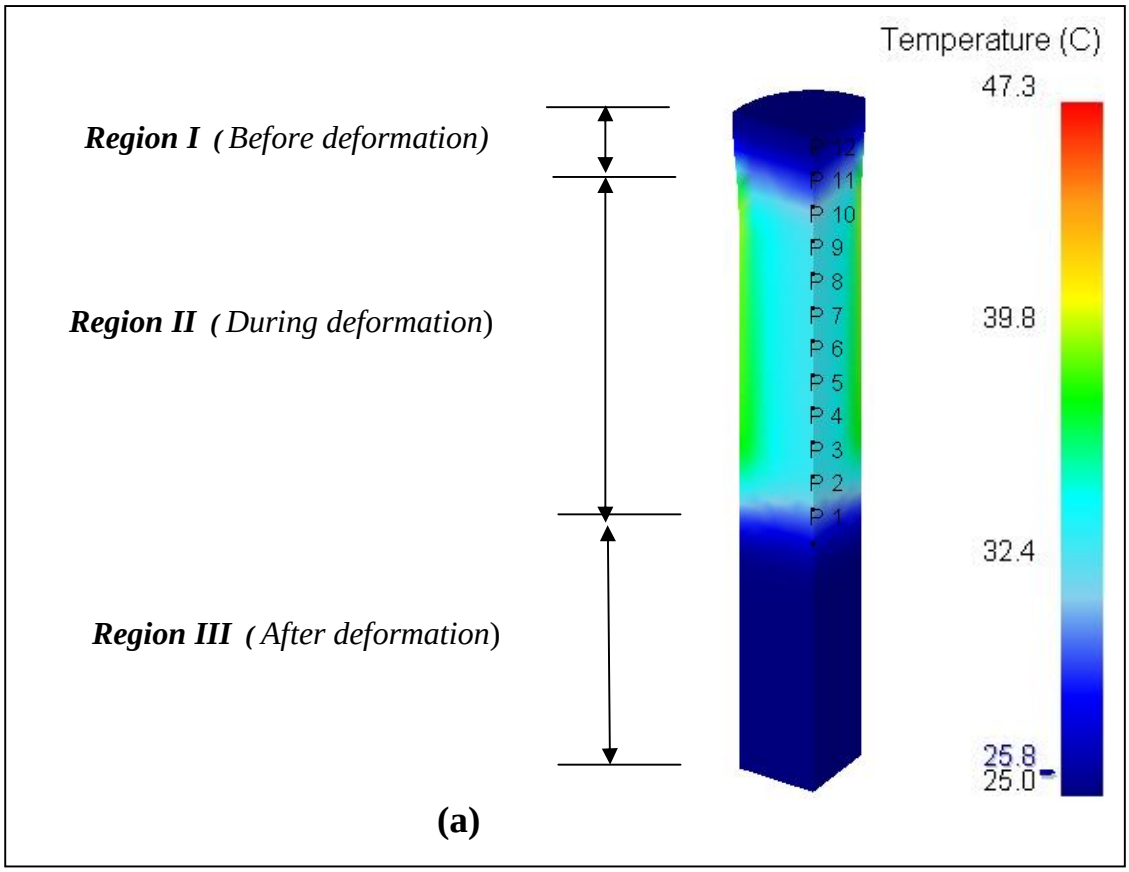

Figure(8). Distribution of the temperature at the centerline in three regions of wire.

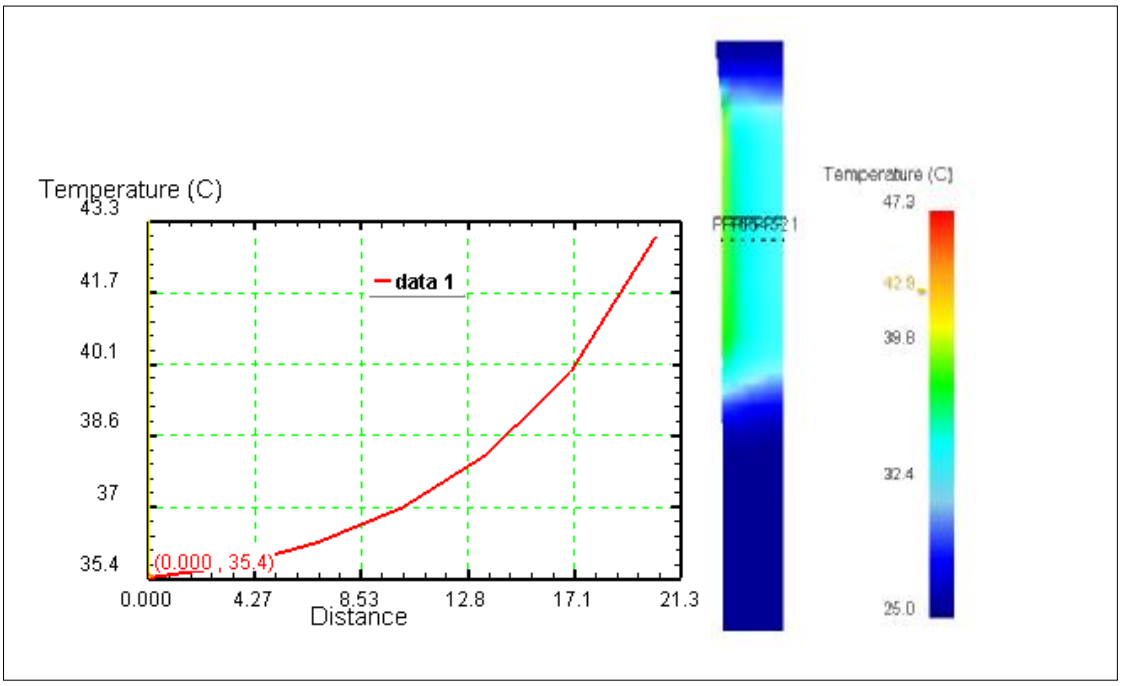

Figure(9) . Distribution of temperature rise from the center of the wire towards the wire surface.

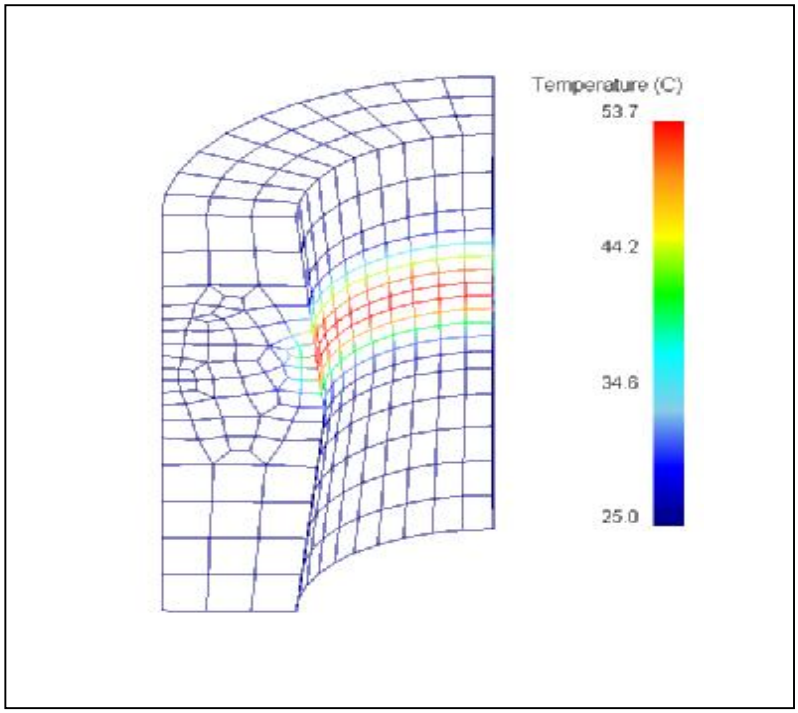

Figure(10). Distribution of temperature in die.

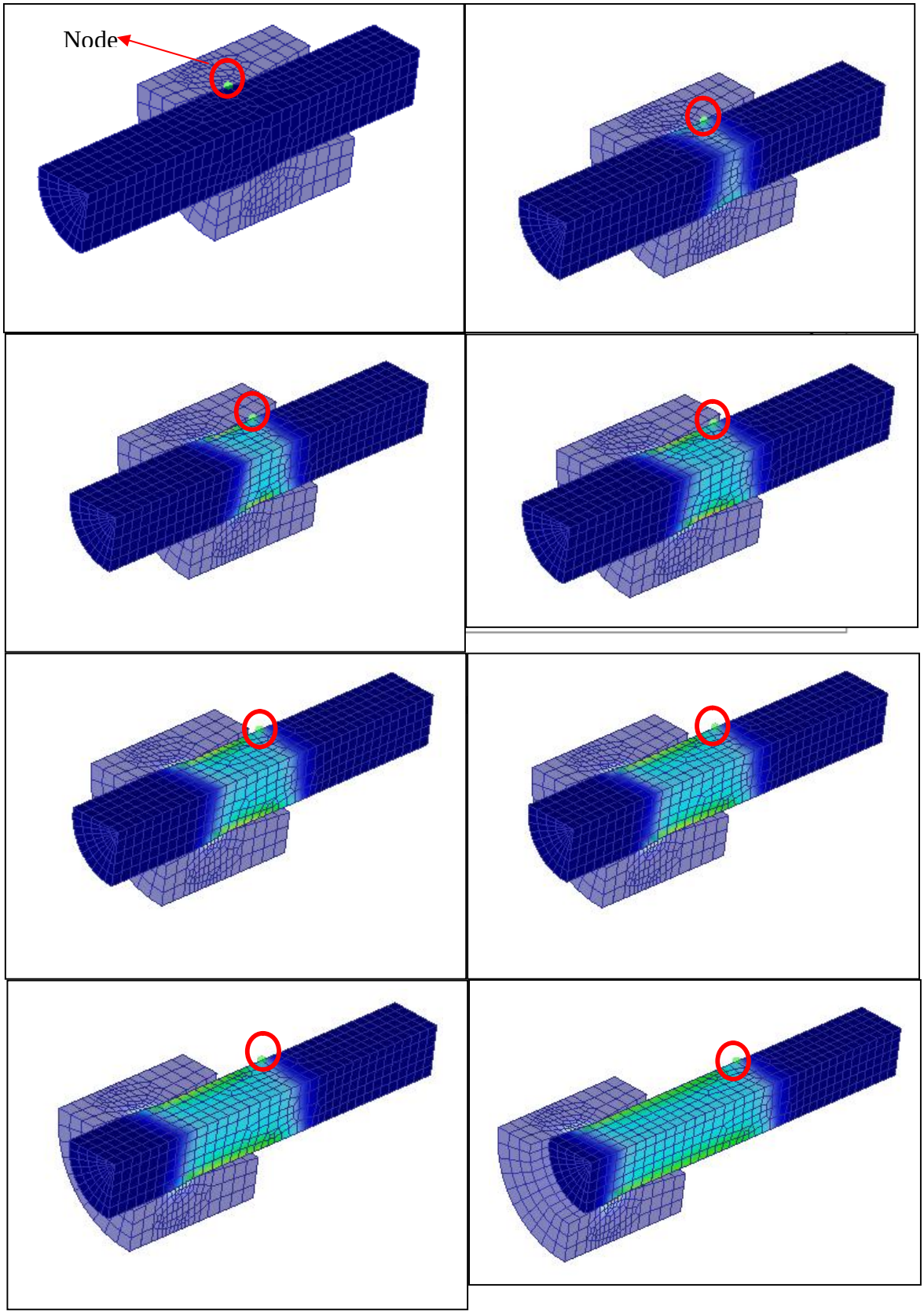

Figure(11). Nodal temperature change with change in its location relative to die during the wire drawing process.

5. Conclusions

The following conclusions may be achieved from the results presented in this paper:

1. The results obtained from the present work verify that the process of wire cold drawing could be theoretically estimated using the finite element method with a reasonable degree of accuracy.
2. Temperature rise during the cold drawing process for known conditions could be estimated.
3. The temperature rise in wire during the drawing process is less than in die.
4. The location of maximum temperature in the die occurs at the contact area before wire exits from the die.

6. References

[1] Aly El-D. and Sadek Z. K., 1998,"Temperature Rise in Wire-Drawing", Journal of Materials Processing Technology, No. 83,pp.72-83.

[2] Vega G., Haddi A. and Imad A. ,2009,"Investigation of process Parameters Effect on the Copper-Wire Drawing" .No. 30, pp.3308-3312.

[3] VerstamH.,2006,"The Influence of Bearing Geometry on the Residual Stress State in Cold Drawn Wire, Analysed by the FEM", No. 171,pp.446-450.

[4] Hoon C., Hyung H. J., Sang G. L., Byung-M. K. and Young-J. K.,2002,"Effect of Reduction Ratio, Inclusion Size and Distance Between Inclusions on Wire Breaks in Cu Fine Wiredrawing". 130–131, pp.416-420.

[5] Lucca D.A., Wright R.N., 1991"Heating Effect in the Drawing of Wire and Strip Under Hydrodynamic Lubrication Conditions", PED. vol. 54:TRIB. vol. 2, Tribological Aspects in Manufacturing, ASME, New York, pp. 291– 313.

[6] McAllen P.J., PhelanP.,2007," Numerical Analysis of Axisymmetric Wire Drawing by Means of a Coupled damage Model", Journal of Materials Processing Technology, No.183, pp.210–218.

[7] Vega G., Haddi A., Imad A.,2009," Investigation of Process Parameters Effect on the Copper-Wire Drawing", Materials and Design,No.30, pp.3308–3312.

[8] Tiernan P., Hillery M.T.,2008," An Analysis of Wire Manufacture Using the Dieless Drawing Method", Journal of Manufacturing Processes,No.10, pp.12-20.

[9] Deform-3D V6.1user manual ,2007,“ Design Environment for Forming”.

7. Nomenclature

English Symbols		Units
A_o	initial cross-sectional area of the wire material	m^2
A_f	final cross-sectional area of the wire	m^2
c	*specific heat of the wire material*	$J/Kg.K$
K	*strength coefficient of the material*	MPa
n	strain-hardening exponent	
r	fractional reduction ratio	
$\bar{Y}$	the average flow stress	N/m^2
ΔT	temperature rise at the die exit	^oC
W_{tot}	energy required for drawing per unit volume of the wire	W/m^3
Greek Symbols		**Units**
α	Half die angle in radians	degree
μ	Coefficient of friction	
σ_d	the drawing stress	N/m^2
ε_{1f}	Final axial strain	
ε_1	Axial strain	
ρ	density of the material	Kg/m^3

Partial Transmission Sequence of Multi-Carrier Modulation

Abdulgaffar S. M.

Electrical & Electronic Department

College of Engineering

Thi-Qar University

Abstract

Partial Transmission Sequence (PTS) method proposed is one of the methods to reduce the Peak to Average Power Ratio (PAPR) of Orthogonal Frequency Division Multiplexing (OFDM) system. In which each symbol of OFDM in the frequency domain is divided into sub blocks and each one, multiplied by a phase factor to rearrange the origin symbol to a version with the lowest PAPR. This method is based on changing the phase of each sub blocks to reduce the probability of occurrence high PAPR. The nonlinear behavior of the phase affect's the accuracy of reduction which makes it different as compared with this method.

In this paper, a proposed method is suggested to reduce the complexity of such method .

Keywords :Partial Transmission Sequence, multi-carrier Modulation, Orthogonal Frequency Division Multiplexing (OFDM) system.

المستخلص

تعد طريقة الإرسال الجزئي المتسلسل (PTS) إحدى الطرائق المعتمدة لتقليل نسبة القمة إلى المعدل للقدرة في نظام التجميع المتعدد بتقسيم التردد المتعامد (OFDM). تتلخص الطريقة المذكورة بتقسيم كل رمز من رموز نظام OFDM في حيز التردد إلى مجموعات جزئية تضرب كل واحدة منها بمعامل طور الغرض منه تقليل PAPR قدر المستطاع وبذلك تكون اللبنة الأساسية لهذه الفكرة هي تقليل احتمالية حدوث الـ PAPR العالية من خلال التلاعب بأطوار المجاميع الجزئية المذكورة. السلوك اللاخطي للطور المستخدم يعمل على زيادة الدقة في تخفيض PAPR مقارنة مع السلوك الخطي المتبع بطريقة PTS التقليدية. في هذا البحث تم اقتراح طريقة لتقليل التعقيد في بناء المنظومة المذكورة.

1. Introduction

Orthogonal frequency division multiplexing (OFDM) has been receiving considerable attention for high-speed wireless communication system. One of the major drawbacks of OFDM is, however, the high peak-to-average power ratio (PAPR) of the transmission signal [1]. OFDM with high PAPR requires high linear amplifiers. Otherwise, performance degradations occur and the out-of-band power will be enhanced [1,2].

Several methods have been proposed to reduce the problem of PAPR. These methods deal with different approach's in interpretation of spurious high peaks. Partial transmission sequence (PTS) can be classified as one of the these methods. Let us consider an OFDM system with N subcarriers. Each OFDM symbol $y(n)$, consists of N complex baseband data $x_0, x_1, ..., x_{N-1}$ carried on the N subcarriers respectively. Then the OFDM signal may be represented by:- [3].

$$y(n) = \frac{1}{\sqrt{N}} \sum_{k=0}^{N-1} X_k \exp\left(2jp \frac{nk}{N} \right) \quad (1)$$

where X_k is the complex baseband data, k is index for subcarrier and n is index for the discrete time OFDM symbol.

The complementary cumulative distribution function (CCDF) of the PAPR denotes the probability that the PAPR of a data block exceeds a given threshold [4,5]. The CCDF of the PAPR of a data block is derived as:

$$P(PAPR > l) = 1 - F(l) \quad (2)$$

Where l is threshold value, $F(l)$ is the cumulative distribution function (CDF).The mathematical form of the cumulative distribution of the PAPR is :

$$F(l) = (1 - \exp(l))^N \quad (3)$$

2. Partial transmission sequence method

The partial transmission sequence type is shown as in Figure (1).

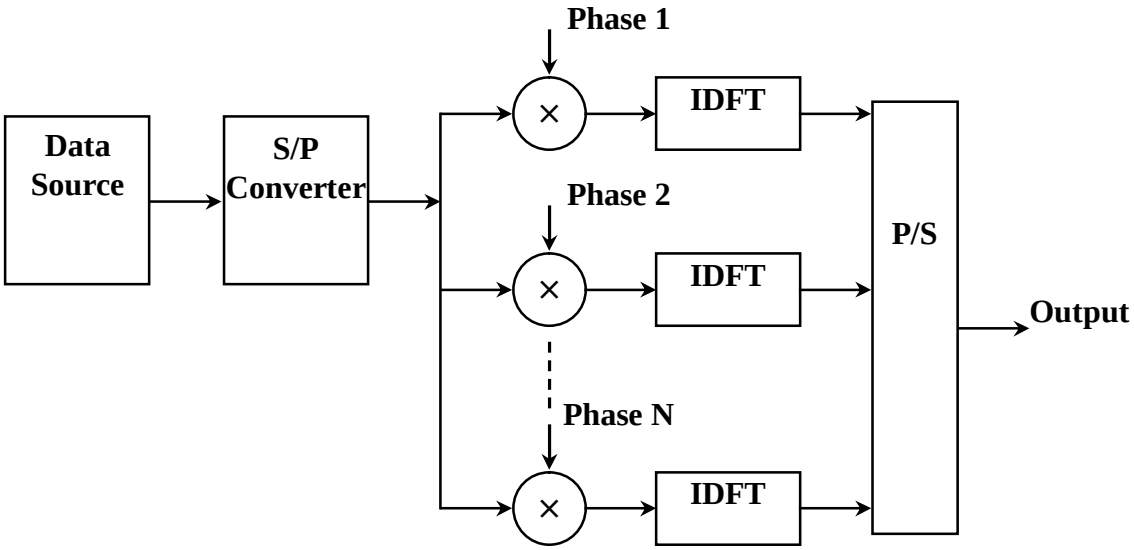

Figure(1). Partial transmission sequence method.

then each sub-block of subcarriers is multiplied by a constant phase factor $\exp(jf^{(d)})$, and these phase factors are optimized to minimize the PAPR [4,6].

$$y = \sum_{d=1}^{D} IDFT\{X^{d}\} \cdot \exp\left(jf^{(d)}\right) \tag{4}$$

The phase may be calculate by the following equation [7]:-

$$\left\{f(d)\right\}_{d=1}^{D} = \underset{\left[\exp\left(jf^{(1)}\right),\ldots,\exp\left(jf^{(d)}\right)\right]}{\arg\min} \left(\max \left| \sum_{d=1}^{D} IDFT\left\{X^{(d)} \cdot \exp\left(jf^{(d)}\right)\right\} \right| \right) \tag{5}$$

However, the calculated phases may reduce the peak to average power ratio as a result of increasing the average power.

3.Proposed method

The idea of this paper may be concluded by suggesting a method to calculate the phase of the partial transmission sequence this method. This method depends on the adaptation of the phase to a value which reduce the peak to average power ratio. Firstly the phases are assumed to have constant values and according to the peak to average power ratio, the phase values are changed. The deference between the peak to average power ratio in $i^{th}$and $(i+1)^{th}$ iteration represents the error signal, then the phase values are taken to reduce this error signal.

4. Results

Computer simulation tests have been taken to show the performance of the traditional and the suggested method in these test, the number of subcarrier(N) are assumed to have a values of 16 and 32. Figure(2) shows the performance of the suggested system for N=16, while Figure (3) shows the performance for N=32. The value of the peak to average power ratio of the traditional and the suggested methods are shown in Table (1) and Table (2). Table (1) shows the PAPR for N=16 while Table (2) shows the PAPR for N=32.

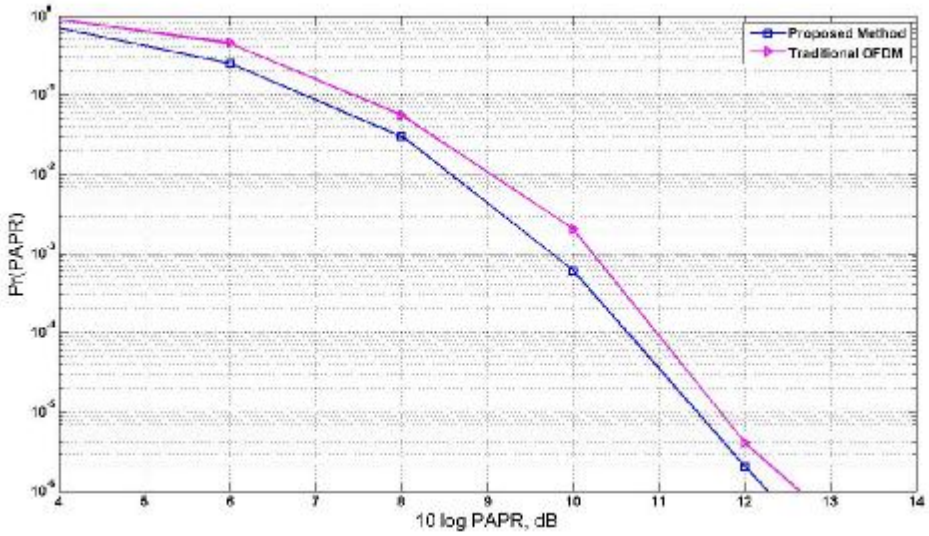

Figure (2). Performance of traditional and suggested systems for N=16.

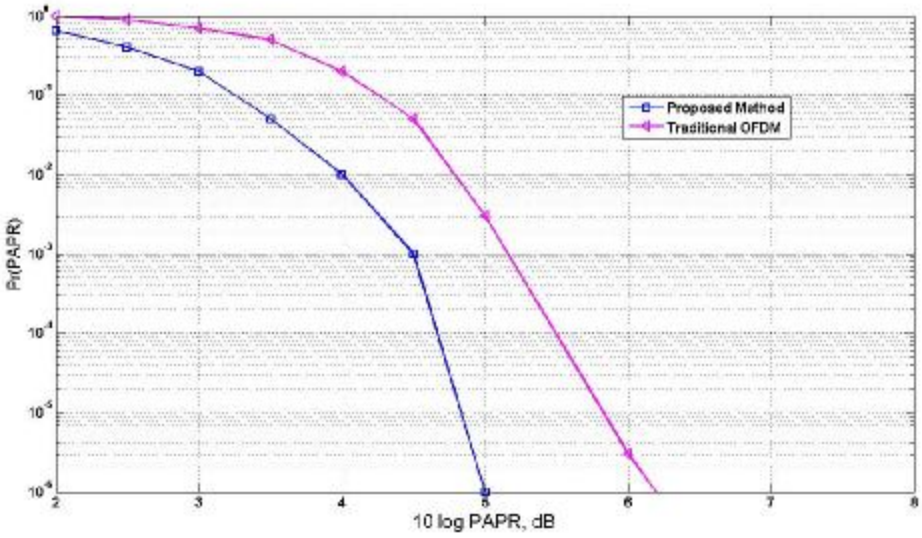

Figure (3). Performance of traditional and suggested systems for N=32.

Table (1). Peak to average power ratio for the traditional and suggested system N=16.

Traditional	11.0412	10.4999	9.463	7.8224	3.4484
Proposed	4.3329	3.9959	3.6771	2.9224	1.185

Table(2). Peak to average power ratio for the traditional and suggested system N=32.

Traditional	12.2736	11.9142	8.0309	6.9588	6.7263
Simulated	5.4223	5.1278	3.8416	3.6376	3.4401

5. Conclusions

In this paper, a method for calculating the phase of partial transmission sequence of the multicarrier modulation system is suggested. The performance of the suggested method shows the ability of the system to reduce the PAPR as shown in Tables (1) and (2) with acceptable performance as shown in Figures (1) and (2). The phase of the partial transmission sequence is calculated according to the error signal for two iterations of the peak to average power ratio of the output signal.

6.References

[1] Wu and Zou W. Y., Aug. 1995,"Orthogonal Frequency Division Multiplexing: A Multi-Carrier Modulation Scheme", IEEE Transactions on Broadcasting Vol. 41, PP. 392-399.

[2] Fazel K., and Kaiser S., 2003,“ Multi-Carrier and Spread Spectrum Systems “,, John Wiley & Sons Ltd.

[3] Kang D.S. and Chao L.M., May 2005,“ OFDM PAPR Reduction Using Clipping with Distortion Control “, IEEE International Conference on Communications, vol. 4, pp. 2563-2567.

[4] Mobasher A. ,and Khaandani A. K., 2005,“ Integer-Based Constellation Shaping Method for PAPR Reduction in OFDM System “, Department of Elec. and Comp. Engineering, University of Waterloo, Ontario, Canada.

[5] Y-H, You, Jeon G. ,and Paik J-H., Dec. 2003,"A Simple Construction of OFDM-CDMA Signals with Low Peak to Average Power Ratio," IEEE, Trans. Vol. 49, pp. 403-407.

[6] Müller S. H. and Huber J. B., February 1997,“ OFDM With Reduce Peak-to-Average Power Ratio by Optimum Combination of Partial Transmission Sequences ”, Electronic Letters, vol. 33, no. 5, pp. 368-369.

[7] Müller S. H., Bäuml R. W., Fischer R. F. H., and Huber J. B., February 1997,“ OFDM with Reduction Peak-to-Average Power Ratio by Multiple Signal Representation “, In Annals of Telecommunications, vol. 52, no. 1 & 2 , pp. 58-67.

Prediction of Power Chimney Parameters Influenced the Operation at Nassiriya City

Rafid M. Hannun
Elect. Eng. Dept.
College of Engineering
Thi-Qar University

Adnan A.A.
Mech. Eng. Dept.
College of Engineering
Thi-Qar University

Ghassan Adnan Abd
Mech. Eng. Dept.
College of Engineering
Thi-Qar University

Abstract

The power chimney tower is one of modern promised energy which may be developed by low losses, simple and has high facilities.

In this paper, many parameters were studied for prediction of system operation. Velocity distribution is the important parameter which gives the first prediction to put the position of erection of power turbine, made or not. The numerical analysis was presented by using GAMBIT and FLUENT 6.3 to predict that high velocity at the expansion of chimney near the solar collector place. This position is very suitable for promoting and building the power turbine since the velocity range was between (33 - 54 m/s) for different solar flux 200W/m^2, 400W/m^2, 600W/m^2 and 800W/m^2. So, the other factors, temperature and pressure were studied to coincide with previous papers in this field.

المستخلص

إن مدخنة القدرة واحدة من أهم الأساليب الحديثة في توليد الطاقة لسهولتها وقلة مفاقيدها وتعقيداتها.

في هذا البحث, تمت دراسة عدة عوامل لها تأثيراً على عمل المنظومة. واهم هذه العوامل هو توزيع السرعة الذي ينبئ أولاً بموقع تنصيب تربين القدرة, يوضع في هذا أو في غيره. تم تقديم تحليل عددي وباستخدام برنامج الكامبتوالفلونت للتنبؤ بمكان أعلى سرعة قرب توسع المدخنة في مركز قاعدة غطاء المجمع الشمسي. حيث إن هذا المكان هو الأكثر ملائمة لبناء تربين القدرة ودعمه لكون سرع الهواء قد وصلت إلى مديات تتراوح بين (33 و 54 م/ثا) عند تسليط إشعاع شمسي بمعدل (200, 400, 600, 800) واط/$م^2$. كذلك تمت دراسة العوامل الأخرى المؤثرة على كفاءة المنظومة مثل درجة الحرارة وفرق الضغط وتبين إنها متوافقة لما تم دراسته سابقا من قبل الباحثين في أدبيات الموضوع.

1- Introduction

Solar energy is an abundant renewable and clean source free of green house gases emissions. Solar power plant is very important use of this energy. Solar chimney technology is a promising large scale of power generation. This technology was first described by Gὺnter in 1931 and tested with the 50 kw Manzanares prototype plant since 1980. There are three components for the combination of this prototype: solar collector, turbine connected with electrical generator.

The installation of solar chimney power plant at Nassiriya city (31.036˚N, 46.21˚E) is suitable to get high energy generated as a result to high rate of solar flux incident as high as flux in the world regions [1].

The incident solar flux on the inclined circular frame of glass layers passes through to black ground at the floor. The air near the ground absorbs the heat to decrease its density. The hot air particles move up to hit the glass ceiling continuously and go to chimney vent. This series heating generates continuous movement of air, then, generates electrical energy by installing turbine connected to electrical generator. The height of chimney causes high pressure difference between the upper and lower points. This pushes increasingly the movement of air particles between the lower points of chimney to up.

Main features of a solar chimney power plant area circular green house type collector and a tall chimney and its centre. Air flowing radial inwards under the collector roof heats up and enters the chimney after passing through a turbo generator [2].

Backstrom and Fluri [2] developed two analyses for finding the optimal ratio of turbine pressure drop to available pressure drop in a solar chimney power plant to be 2/3 for maximum fluid power and using the power law model for this prediction. Haaf et al. [3] , Haaf [4] and Schlaich [5] described the operation and presented results for a prototype solar chimney power plant built in Manzanares, Spain in 1982.

Pretorius and Kröger [6] evaluated the influence of a recently developed convective heat transfer equation, more accurate turbine inlet loss coefficient, quality collector roof glass and various types of soil on the performance of a large scale solar chimney power plant. This simulation of study concluded that the new heat transfer equation reduce the annual plant power output by 11.7%, but , the more realistic turbine inlet loss coefficient only accounts for a 0.66˚rise in annual power production , while utilizing better quality glass increases the annual plant power output by 3.4%.

Tingzhen et. al. [7] carried out numerical simulations on the solar chimney power plant system which divided into three regions: the collector, the chimney and the turbine, and the mathematical models of heat transfer and flow had been setup for these regions. Ming et. al. [8] performed to analyze the characteristics of heat transfer and air flow in the solar chimney power plant system with an energy storage layer. They used different mathematical models for the collector, chimney and the energy storage and the effect of solar radiation on the heat storage characteristic of the energy storage layer. Nizetic et. al. [9] analyzed the feasibility of solar chimney power plants for small settlements and islands of countries in the Mediterranean region; they used 550 m height of chimney with collector roof diameter of 1250 m to produce 2.8 – 6.2 MW of power.

Ninic and Nizetic [10] developed and use of the availability of warm, humid air via the formation of up draft "gravitational vortex column" situated over turbine with numerical solution for solar chimney power plant. Petela [11] used a simplified model of solar chimney power plant which consists of a heating air collector, turbine and chimney to interpretate a thermodynamic based on the derived energy and energy balances. Zhou et. al. [12] analyzed the suitable chimney height of solar chimney power plant using a thermodynamic model validated with the measurements of the only one prototype in Manzanares.

2- Numerical model

2-1 Physical model

In this study, some practical prototype from literature depended on as shown in Figure 1 is selected as a physical model for simulation. The chimney height is 100 m and radius 2.5 m, the collector of 120 m radius and 2m height Figure1.

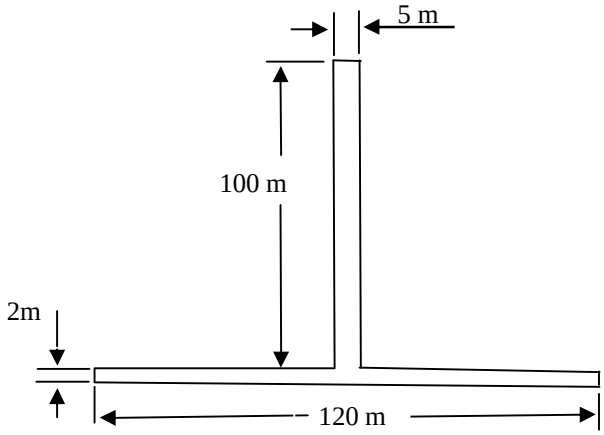

Figure (1). Physical prototype.

2-2 Mathematical model

There are many prototypes in the world have large different heights up to 500 m , with different radii of chimney but with low heights for collector (up to 3m) with wide radii. The model of 100m height of chimney and 2.5 m its radius and the collector of 60m radius and 2 m height are used. The storage layer of energy such as soil or graved coated by asphalt is the solid matrix of this collector.

The buoyancy induced as natural convection is measured by Rayleigh number (Ra):

$R_a = g\beta(T_h-T_C)L^3/a\upsilon$

Where T_h,T_C is the maximum and minimum temperature of the system respectively. The Ra in this system analysis shows that Ra> 10^10, therefore the flow is turbulent. The continuity, Navier – Stokes, energy equations and k-ε equation are shown below[9]:

$$\frac{\partial r}{\partial t}+\frac{\partial(ru)}{\partial x}+\frac{\partial(ry)}{\partial y}=0 \tag{1}$$

$$\frac{\partial(ru)}{\partial t}+\frac{\partial(ruu)}{\partial x}+\frac{\partial(rvu)}{\partial y}=rgb(T-T_\infty)+m\left(\frac{\partial^2 u}{\partial x^2}+\frac{\partial^2 u}{\partial y^2}\right) \tag{2}$$

$$\frac{\partial(rv)}{\partial t}+\frac{\partial(ruv)}{\partial x}+\frac{\partial(rvv)}{\partial y}=-\frac{\partial p}{\partial y}+m\left(\frac{\partial^2 v}{\partial x^2}+\frac{\partial^2 v}{\partial y^2}\right) \tag{3}$$

$$\frac{\partial(rcT)}{\partial t}+\frac{\partial(rcuT)}{\partial x}+\frac{\partial(rcvT)}{\partial y}=l\left(\frac{\partial^2 T}{\partial x^2}+\frac{\partial^2 T}{\partial y^2}\right) \tag{4}$$

$$\frac{\partial}{\partial t}(rK)+\frac{\partial}{\partial x_i}(rKu_i)=\frac{\partial}{\partial x_j}\left(\left(m+\frac{m_t}{s_K}\right)\frac{\partial K}{\partial x_j}\right)+G_K+G_b-re+S_K \tag{5}$$

$$\frac{\partial}{\partial t}(re)+\frac{\partial}{\partial x_j}(reu_i)=\frac{\partial}{\partial x_j}\left(\left(m+\frac{m_t}{s_K}\right)\frac{\partial e}{\partial x_j}\right)+C_{ie}(G_K+C_{3e}G_b)-C_{2e}r\frac{e^2}{K}+S_e \tag{6}$$

The heat transfer in the energy storage layer may be very complicated [8]. The Brinkman – Forchheimer Extended Darcy model may be used in this paper for storage material as regarded as porous media, as follows:

$$\frac{\partial r}{\partial t}+\frac{\partial(ru_d)}{\partial x}+\frac{\partial(rv_d)}{\partial y}=0 \tag{7}$$

$$\frac{r}{j}\frac{\partial u_j}{\partial t}+\frac{r}{j^2}\left(u_d\frac{\partial u_j}{\partial x}+v_d\frac{\partial u_d}{\partial y}\right)=-\frac{\partial P_r}{\partial x}+\frac{\partial}{\partial x}\left(m_m\frac{\partial u_d}{\partial x}\right)+\frac{\partial}{\partial y}\left(m_m\frac{\partial u_d}{\partial y}\right)-\left(\frac{m}{K}+\frac{rc}{\sqrt{K}}u_d\right)u_d+rgb(T-T_\infty) \tag{8}$$

$$\frac{r}{j}\frac{\partial v_j}{\partial t}+\frac{r}{j^2}\left(u_d\frac{\partial v_j}{\partial x}+v_d\frac{\partial v_d}{\partial y}\right)=-\frac{\partial P_r}{\partial x}+\frac{\partial}{\partial x}\left(m_m\frac{\partial v_d}{\partial x}\right)+\frac{\partial}{\partial y}\left(m_m\frac{\partial v_d}{\partial y}\right)-\left(\frac{m}{K}+\frac{rc}{\sqrt{K}}v_d\right)v_d \quad (9)$$

$$rc\left(\frac{\partial T}{\partial t}+u_d\frac{\partial T}{\partial x}+v_d\frac{\partial T}{\partial y}\right)=\frac{\partial}{\partial x}\left(l_m\frac{\partial T}{\partial x}\right)+\frac{\partial}{\partial x}\left(l_m\frac{\partial T}{\partial y}\right) \quad (10)$$

The heat balance of the storage layer is Shown in Figure(2) with the related equations:

$$Q1+Q2+Q3+\zeta\tau Q4 = 0 \quad (11)$$

Where ……..

$$Q_1=A_1h_1(T_1 - T_2) \quad (12)$$

$$Q_2 = A_2\,б\,(T_1^4 - T_2^4) \quad (13)$$

$$Q_3 = -A_1\,\lambda_m dT/dx \quad (14)$$

The heat balance of the collector glass:

$$Q_5 + Q_6 – Q_2 + Q_7 + \alpha Q_4 = 0 \quad (15)$$

Where :

$$Q_5= A_2h_2(T_g-T_a) \quad (16)$$

$$Q_6 = A_2h_3\,(T_g-T_4) \quad (17)$$

$$Q_7 = A_2\,б\,(T_g^4 – T_5^4) \quad (18)$$

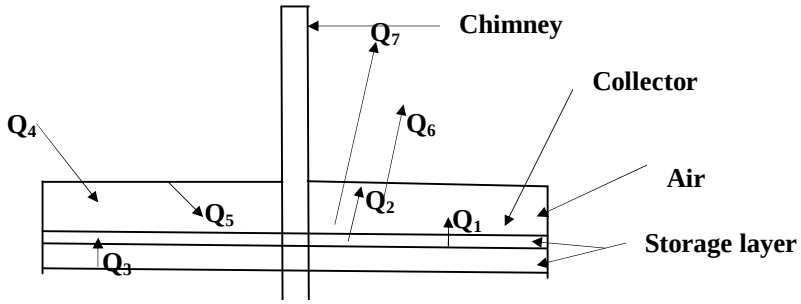

Figure (2).Heat balance of the storage layer and the collector glass.

2-3 Boundary conditions

1. **For chimney**

$$\frac{\partial T}{\partial X} = 0\,, u = 0\,, v = 0 \quad (19)$$

For outside and inside the storage layer

$$\frac{\partial T}{\partial y} = 0\,, u_d = 0, v_d = 0 \quad (20)$$

For outlet conditions:

At $x = \pm\infty$, $T = T_4$, $P = P_{atmosphere}$ (21)

2. Symmetrical axis at chimney centre axis, i.e:

$$u_{(x=+x)} = u_{(x=-x)}\ , v_{(x=+x)} = v_{(x=-x)}, p_{(x=+x)} = p_{(x=-x)} \quad (22)$$

$$m_m\left(\frac{\partial u_d}{\partial y}+\frac{\partial v_d}{\partial x}\right)_{(x=+x)} = m_m\left(\frac{\partial u_d}{\partial y}+\frac{\partial v_d}{\partial x}\right)_{(x=-x)} \quad (23)$$

3- Numerical analysis

The turbulent flow of air inside the system would be analyzed by standard k-ε model, and the energy storage layer can be described by using Brinkman- Forcheimer Extended Darcy model. The SIMPLE algorithm with QUICK Scheme method used to solve the pressure – velocity coupling and momentum and energy equations respectively. These methods were explained by many references such as Ref.[13]. So, the Gambit and Fluent Codes are used to describe the results of this paper Figure3 the study case of chimney system as designed by GAMBIT).

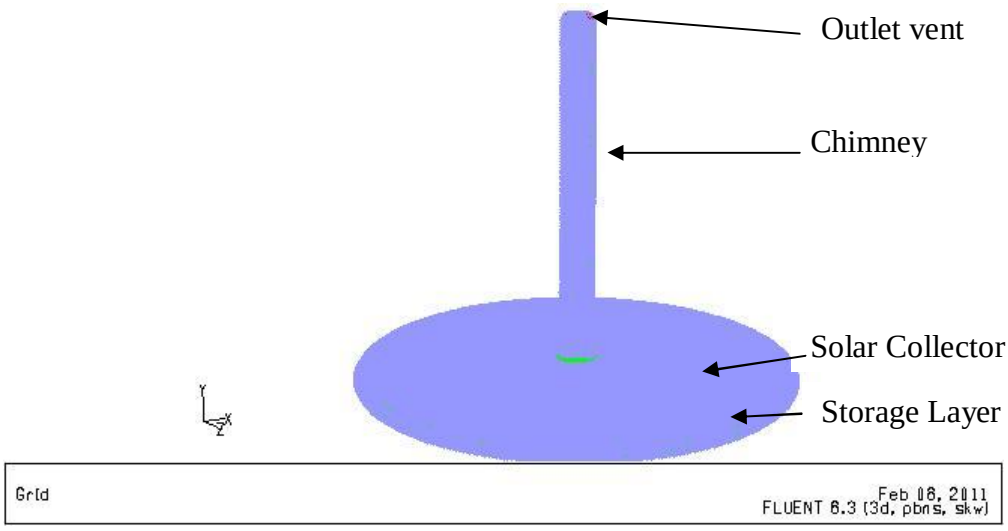

Figure(3) . The domain grid as designed by GAMBIT code on Feb. 8, 2011 .

4- Results and discussion

The heat energy transferred from the solar rays by beam or diffused arrays to glass cover of collector. Then, they transferred to the storage layer depending on high permeability and transmittance, with low reflectance and absorbance of glass cover. In addition to high absorbance low high reflection of storage layer with ability of high convective heat transfer rate.

Many materials and mixtures arranged for storage layers depend on the enhancement of heat transferred from this layer to air inside the collector of solar chimney. Low storage ratio for a lot of materials lies at 600 W/m^2 of solar radiation as mentioned by many researchers [13].

In this paper, four cases of solar radiation fluxes are studied for Al- Nassiriya city case study which lies at 31.036° N, 46.21° E. The cases are 200, 400, 600, 800 W/m^2 of solar flux.

There are many reasons for the selection of turbine erection position inside the chimney requires further discussion. The first factor is the difference in static pressure gradient as shown in Figure (4 and 5).

At a 200 W/m^2 solar flux absorbed by storage layer and transferred as heat to neighbor air inside collector by convective heat transfer shape. The figure arranged by Cartesian coordinates X-Y-Z as shown. High differences in static pressure values(- $1.27x10^{+3}$ to $3.8x10^{-1}$) are measured between the upper point of chimney as low pressure value to high value at the base outer circumference of collector. This high difference is created because of high height of chimney and the heat absorbed by air which accelerates the air velocity cause high relative pressure. It is observed that there are high difference between the gradient of chimney and collector. Therefore, this is one of reasons for turbine installation at this base. Furthermore, from the other shapes of Figure(4 B, C, D), it is seen that the relative static pressure changed significantly with increasing the solar radiation (from 400 W/m^2 to 800 W/m^2) . That is because of increasing the air density inside the collector in comparison with environment of station at the same altitude. This heat transferred with natural convection to increase the pressure gradient which reach the levels between (-1.3×10^{-3} Pa to 3.95×10^{-1}Pa), ($-1.83 \times 10^{+3}$Pa to 5.72Pa) and ($-1.67 \times 10^{+3}$ Pa to $6.68 \times 10^{+2Pa}$) for 400, 600 and 800 W/m^2 of solar radiation intensity.

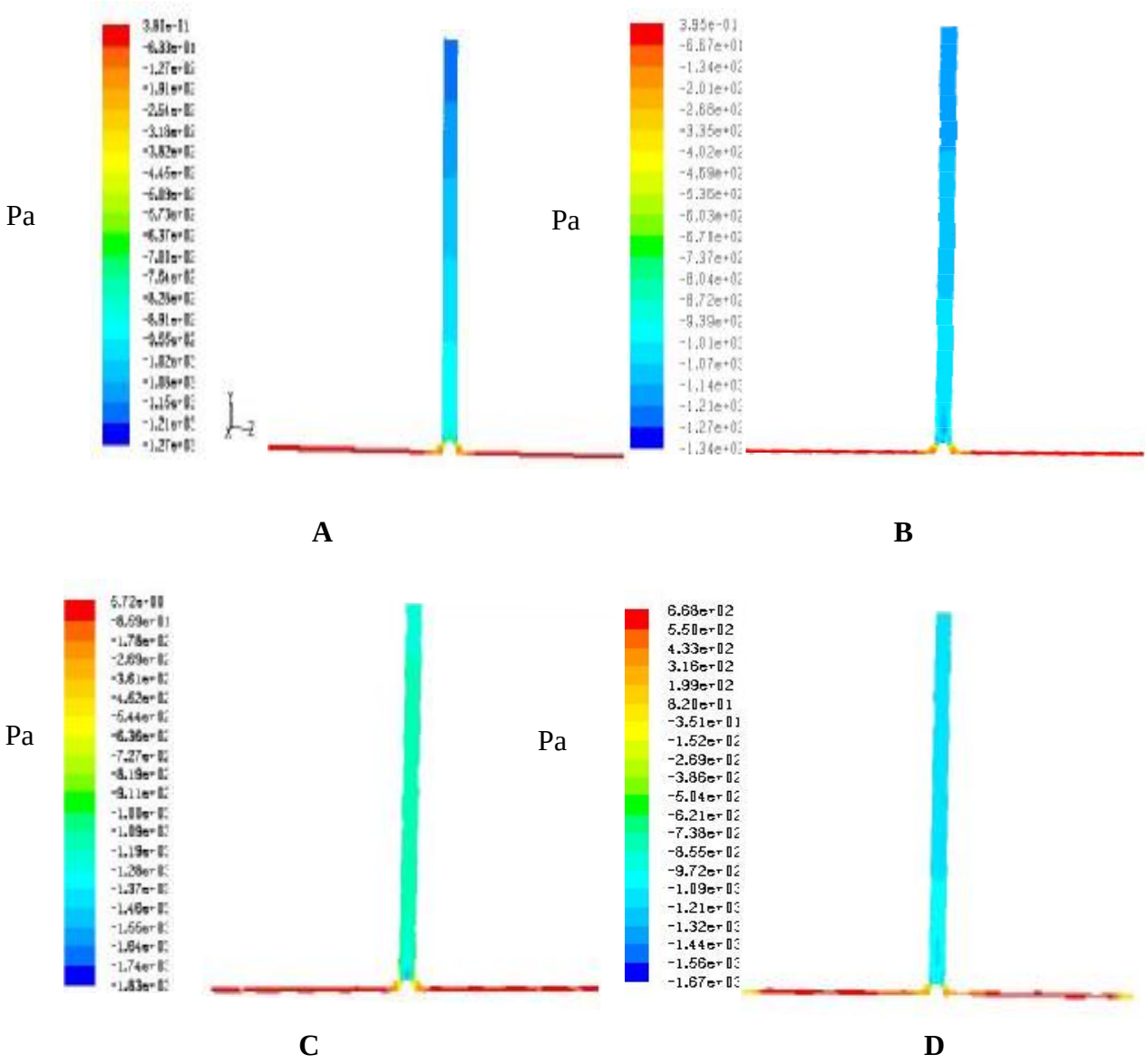

Figure(4). Pressure gradient at A. 200W/m^2, B. 400W/m^2, C. 600W/m^2 and D. 800W/m^2 of solar flux.

Figure(5) shows the static pressure distributions which is calculated from the central section of whole domain as circumferential mean values which be sure the validity of this study and prove the mentioned pressure values. The maximum values of pressure are for 800W/m^2 solar flux, but the minimal values are for 200W/m^2. So, the other values of solar flux lie between the previous lines. The pressure gradient is approached to atmosphere at the inlet vent of the system but it is increased while reach the top of chimney since high difference in relative pressure due to the heat and height of chimney which work as vacuum pressure to increase the air velocity.

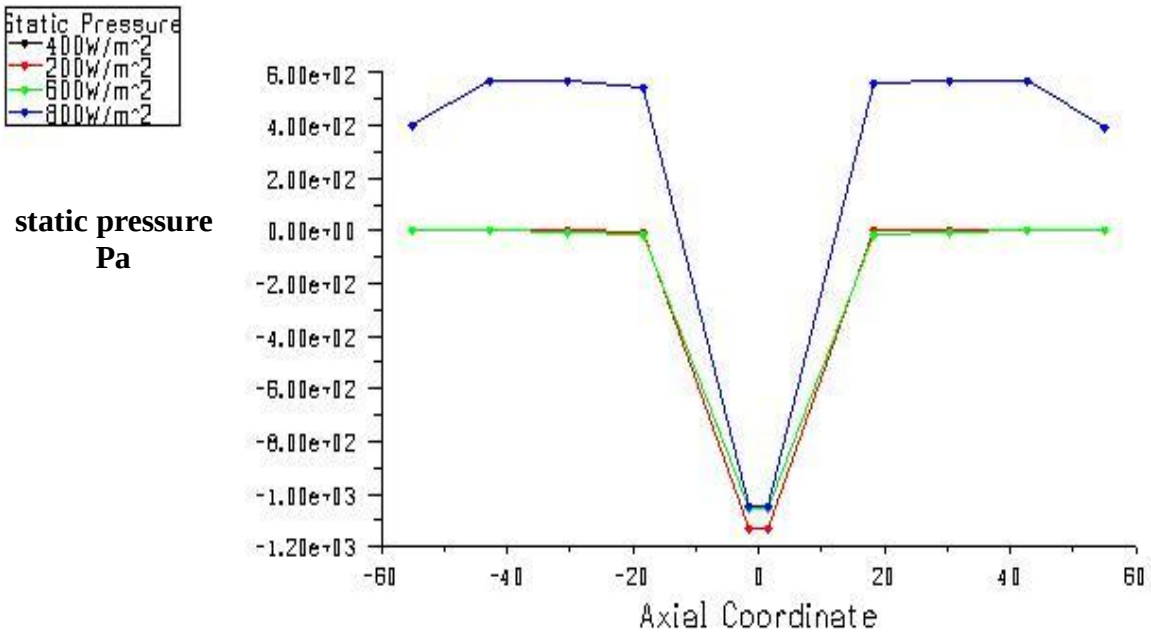

Figure(5). Static pressure of domain calculated for central section plane.

Figure(6) shows the temperature distribution inside the system of solar chimney. Figure (5 A) is an indication of heat absorbed or transferred to different trends of parts chose at 200 W/m^2 of solar radiation intensity. This shape of temperature range (534 K to 299 K) which is at ambient temperature of 308 K.

FLUENT Code demonstrates wide ranges of measurements near the effective domain. The dominated temperature of air inside the chimney is 319K as observed by limited range contour which shown in Figure(6B). The Figure6C denotes to the high temperature recorded at the end edge of circular collector at the base which is corresponded to solar storage layer. It is notably high hot place than collector space because the heat coefficient at the end has low value as a result to low velocity of convicted air. This air speed increases in the direction of chimney centre.

The other shapes of Figure(6 D, E and F)denote to temperature difference at solar flux of 400, 600 and 800W/m^2 respectively. It is normally, there are gradually higher temperature ranges than 200W/m^2 of solar flux mode. This heat forces the velocity magnitude in the direction of chimney centre as a result to natural convection.

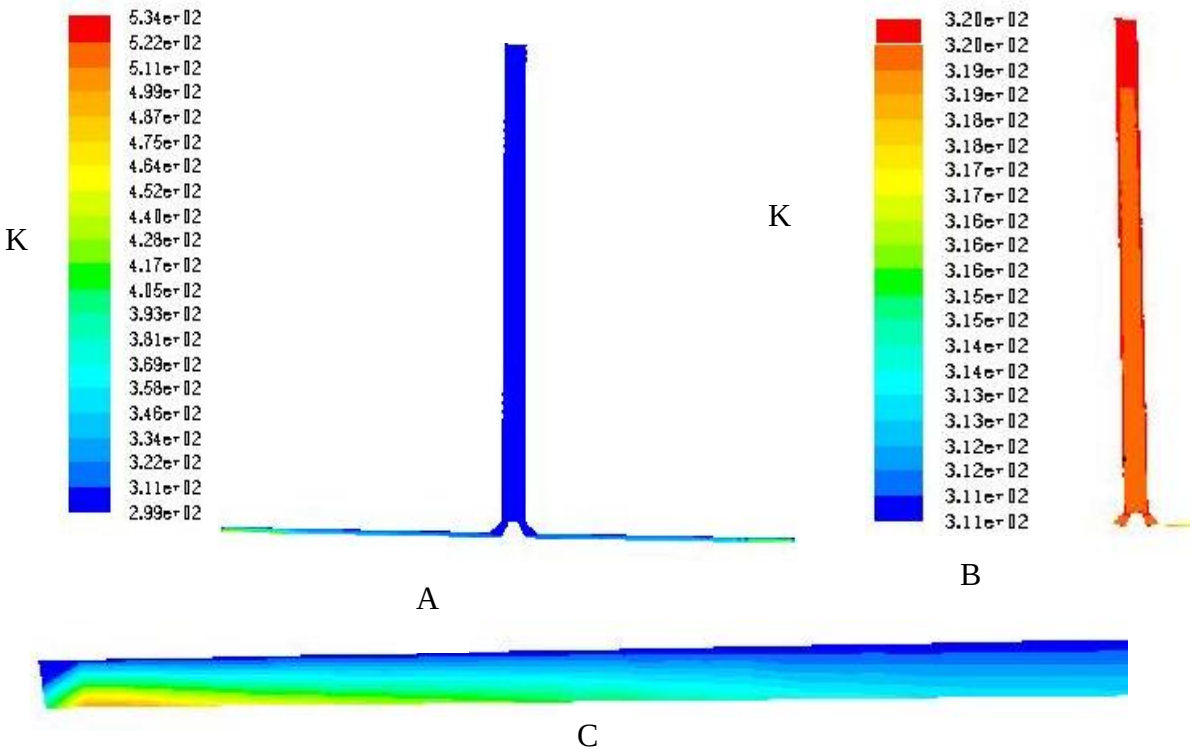

Figure(6). Static temperature at 200W/m^2 solar flux for A. the system, B. chimney and C. collector section.

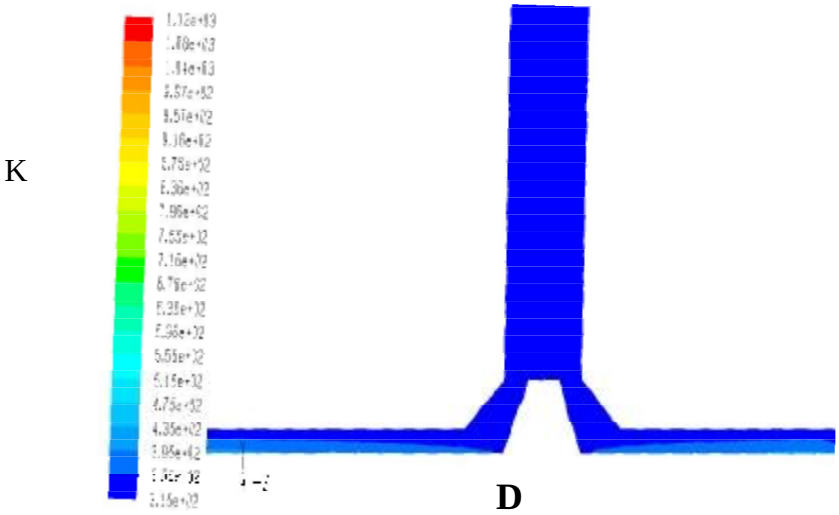

Figure (6). Static temperature at D. 400W/m^2.

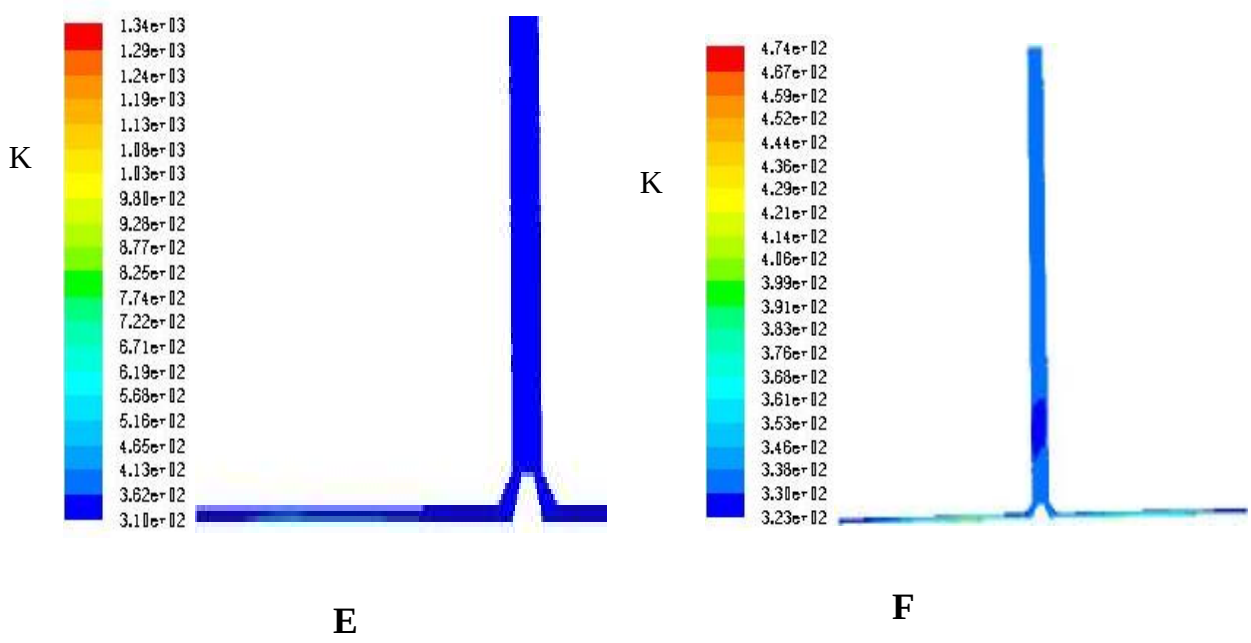

Figure(6). Static temperature at E.600W/m^2, and 800W/m^2 solar flux.

Figure(7) shows the circumferential average static temperature values for 200W/m^2 solar flux radiation and the upper value of it (800W/m^2). This indicated dramatically the previous conclusion that the high flux has high temperature values reverse to lower flux which has low temperature gradient. So, there are some points take different slop from the other points of the curve as a result to turbulent flow of flowing air in this section and all other sections. The maximum values of temperature trend from the free edges in the direction of chimney centre since the continuous solar heating from the outer edge to inner collector parts. This is in agreement with literature.

The velocity vectors of the system are shown in Figure(8) which indicates that high velocity magnitude at concentration of solar radiation flux 200W/m^2 reaches 33m/s at the position of turbine at the lower part of chimney with no load state as shown in A. So, there is a low velocity gradient at the outer end of collector of the base part of system. The velocity notably increases when directed to the chimney centre due to the heat flux increase, narrow area of collector disc and low pressure gradient. The velocity range increases directly with increasing the heat flux of solar array as noted in Figure 8B, C and D. for solar flux 400, 600 and 800W/m^2 respectively.

The velocity ranges reach 39, 42, and 54m/s respectively. These ranges are suitable for using big turbines at lower position of chimney or using multi-stage turbine to have high gain energy.

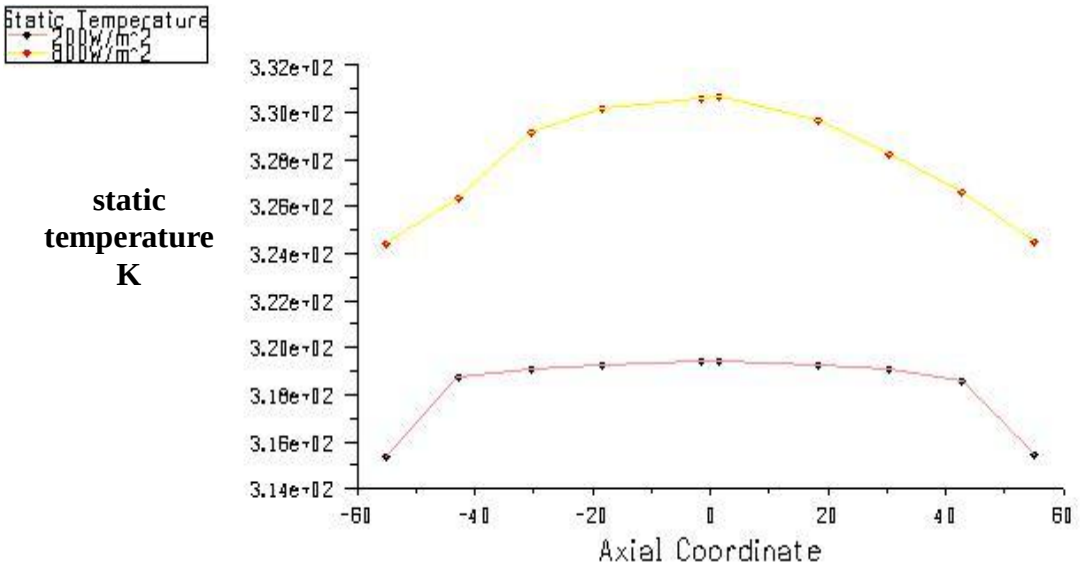

Figure (7). Circumferential average values of static temperature for lower and upper flux.

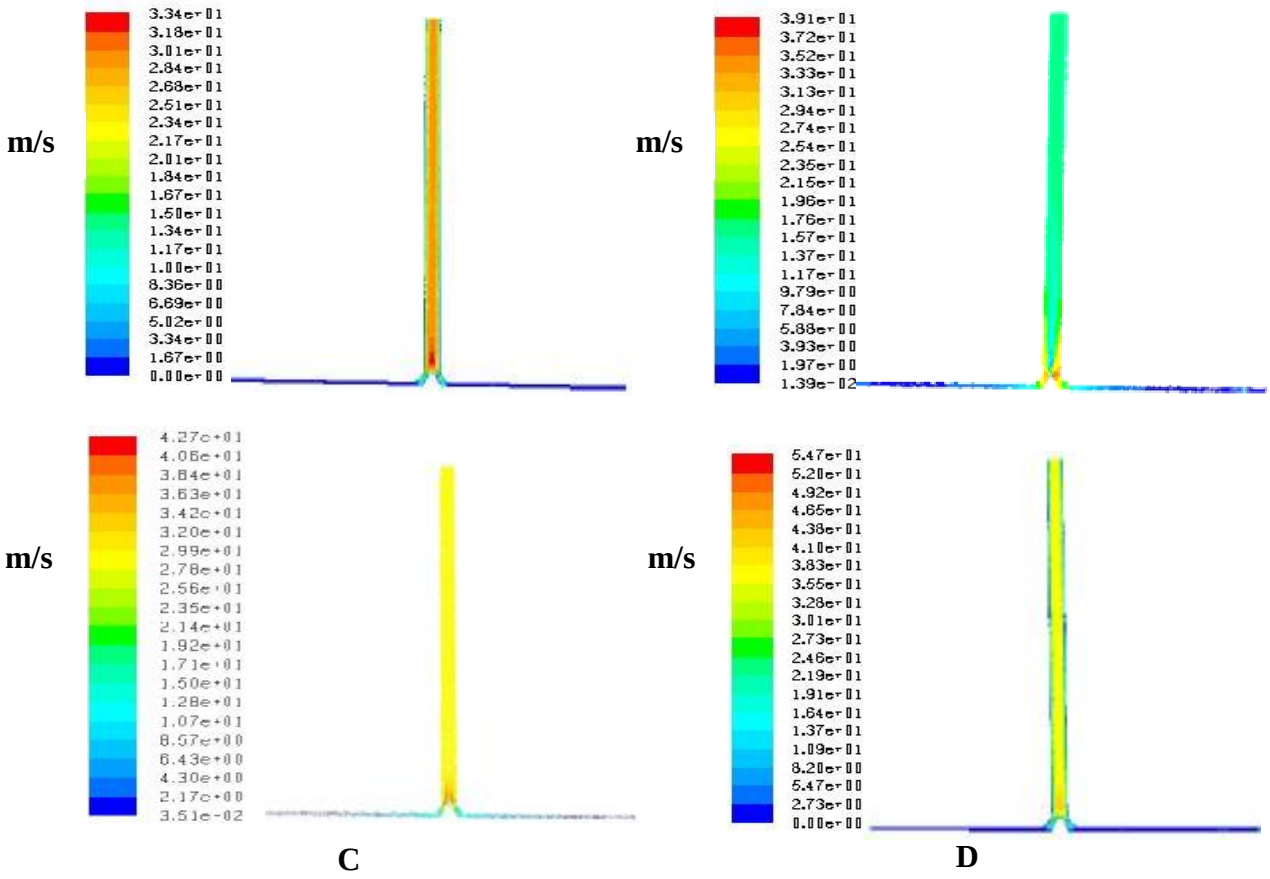

Figure (8). Velocity distribution at A. 200W/m^2, B. 400W/m^2, C. 600W/m^2 and D. 800W/m^2 of solar flux.

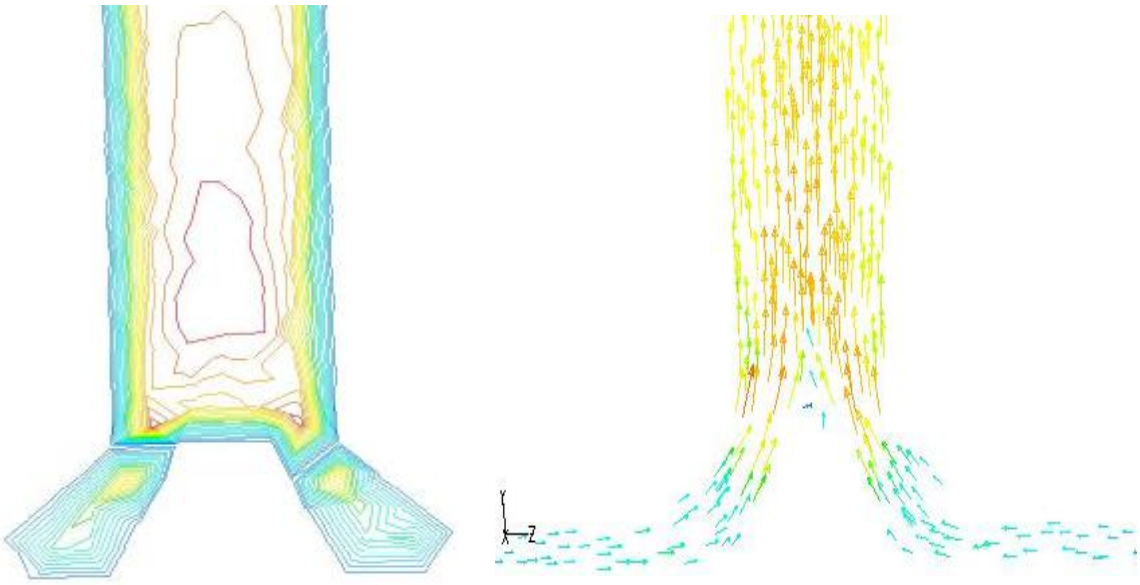

A B

Figure(9). A-Velocity contours and B-Velocity vectors at the turbine position.

The velocity stream line of system is shown in Figure(9 A) which denotes high velocity range at the bottom chimney part in the direction of centre. Also, Figure(9 B) presents the velocity vectors coloured by velocity magnitude which indicates the velocity gradient at the space of system.

The velocity magnitude distribution on the system domain with its position in the centre section for whole system is presented by Figure(10). It is denoted that high velocity values lie at the chimney but low values at the end edges of collector since the reasons mentioned in this paper before.

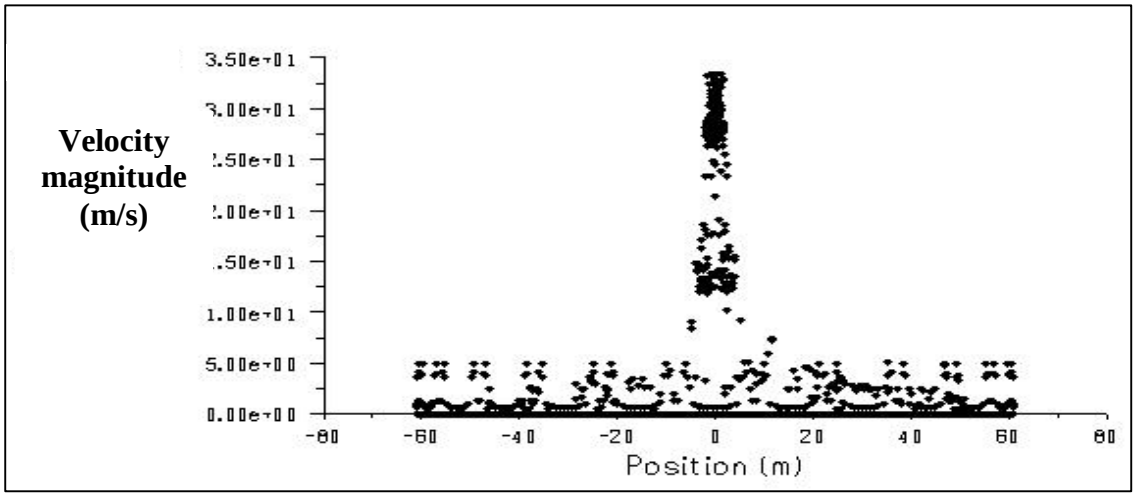

Figure (10). Velocity magnitude points with position of section centre.

The upper yellow curve of Figure(11) denotes the velocity magnitudes in the axial coordinate calculated as average values of the central section of domain. It is observed that higher velocity values trend from the outer edge to the central part of domain (chimney) as mentioned before. The other curves give the same conclusion, but there are some values for collector edge put as higher than the inner because of turbulent flow with axial values at this section which may be made lower at neighbor section.

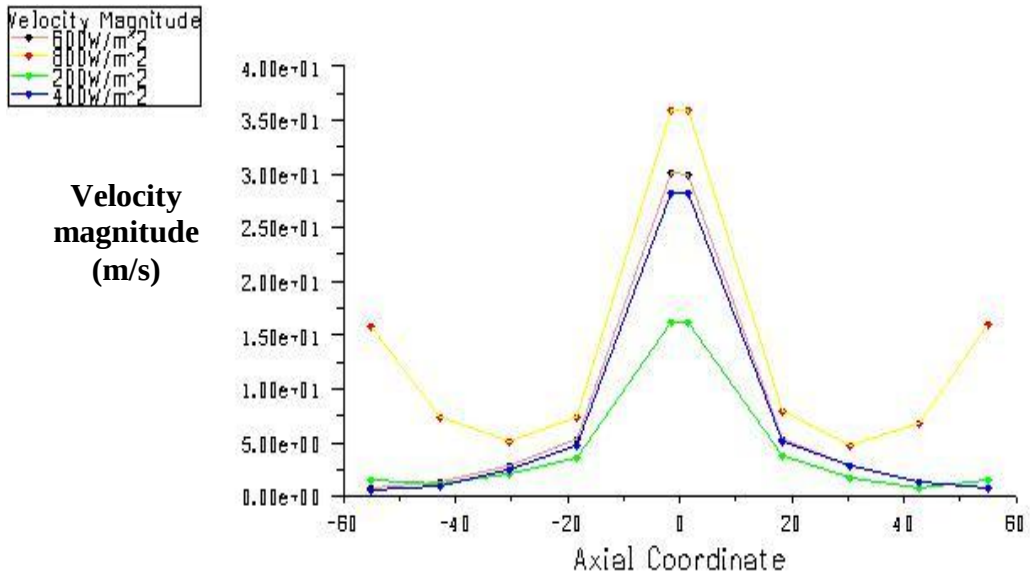

Figure(11). Circumferential average of velocity magnitude for different solar flux.

5- Conclusions

It is noted from the numerical solution and the analysis of chimney tower system for the predicted case study for Nassiriya city, there are some conclusions presented about the circumferential parameters such as:

1. The velocity of air is high at the base section of chimney but it is very low at the outer edge of collector canopy and then converged in developing to the chimney centre.
2. The temperature of storage wall of solar heat flux is highest as a result to heat absorption but it is low in the chimney due to air movement with heat transferred inside the system.
3. The pressure gradient is approached to atmosphere at the inlet vent of the system but it is increased while reach the top of chimney since high difference in relative pressure due to the heat and height of chimney which work as vacuum pressure to increase the air velocity.
4. Due to the high velocity recorded at the expansion of chimney, the turbine power is preferred to built-in.

6- References

[1] Hannun R.M.,2005, " Modeling of Solar Thermal Power Plant" , M.Sc. thesis, University of Technology, Mechanical Engineering Department, Baghdad.

[2] Backström T. and Fluri T. , 2006," Maximum Fluid Power Condition in Solar Chimney Power Plants –An Analytical Approach", Solar Energy 80, pp. 1417-1423.

[3] Haaf W., Friedrich K., Mayr G., Schlaich J.,1983, "Solar Chimneys, Part I: Principle and Construction of the Pilot Plant in Manzanares", International Journal of Solar Energy 2, 3–20.

[4] Haaf W., 1984,"Solar Chimneys, Part II: Preliminary Test Results From the Manzanares Pilot Plant", International Journal of Solar Energy 2, 141–161.

[5] Schlaich J., 1994,"The Solar Chimney: Electricity from the Sun", Deutsche Verlags-Anstalt, Stuttgart.

[6] Pretorius J. P. and Kröger D.G. ,2006,"Critical Evaluation of Solar Chimney Power Plant Performance ", Solar Energy 80, pp. 535 -544.

[7] Tingzhen M., Weil., Guoling X., Yanbin X., Xuhu G. and Yuan P., 2008,"Numerical Simulation of the Solar Chimney Power Plant Systems Coupled with Turbine", Renewable energy 33, pp. 897-905.

[8] Ming T., Liu W. , Pan Y. and Xu G., 2008," Numerical Analysis of Flow and Heat Transfer Characteristics in Solar Chimney Power Plant with Energy Storage Layer", Energy Conversion and Management 49,pp. 2872-2879.

[9] Nizetic S. , Ninic N. and Kalrin B., 2008," Analysis and Feasibility of Implementing Solar Chimney Power Plants in the Mediterranean Region", Science direct, Solar Energy 33, pp. 1680-1690.

[10] Ninic N. , Nizetic S., 2009,"Elementary Theory of Stationary Vortex Columns for Solar Chimney Power Plants", Science direct, Solar Energy 83, pp476-476.

[11] Petela R. , 2009,"Thermodynamic Study Of A Simplified Model of the Solar Chimney Power Plant ", Science direct, Solar Energy 83, pp. 94-107.

[12] Zhou X., Yong J., Xiao B. Hou G., and Xing F., 2009,"Analysis of Chimney Height for Solar Chimney Power Plant" Applied Thermal Engineering 29, pp.178-185.

[13] Tao WQ., 2001,"Numerical Heat Transfer", 2nd ed. Xi'an, China: Xi'an Jiaotong University Press.

7- Nomenclature

Symbol	Definition
A	Thermal diffusivity (m^2/s).
A_1	The area of storage layer surface(m^2).
A_2	Glass area ($m^{2)}$

G	Gravitational body force (m/s^2)
H_1	The heat transfer coefficient between the storage layer and the air inside the collector(W/m^2K).
h_2	Convection heat transfer coefficient between the surface of glass and air (W/m^2K).
h_3	The convective heat transfer coefficient (W/m^2K)
L	Collector height (m) .
Q_1	The heat transfer between the storage layer and the air (W).
Q_2	The radiation heat transfer between the storage and the collector glass (W).
Q_3	The conduction heat transfer from the storage inside the porous media (W).
Q_4	The solar heat flux transferred to the collector (W).
Q_5	The convective heat transfer between the glass surface and the air inside the collector (W).
Q_6	The conduction heat transfer between the collector surface and the ambient (W).
Q_7	The radiation heat transfer between the collector surface and the sky (W).
R_a	Rayleigh number
T_1	The storage layer temperature(K).
T_2	The air temperature inside the collector (K)
T_3	Glass collector temperature (K).
T_4	The ambient temperature (K)
T_a	Air temperature inside the collector(K)
T_g	Glass temperature (K).
T_s	Sky temperature (K).
β	Coefficient of Thermal expansion (1/K)
λ_m	The heat conduction coefficient (W/mK)
μ	Dynamic viscosity (kg/m.s)
ν	Kinematic viscosity (m^2/s)
ρ	Density (kg/m^3)
τ	The transmissivity of the collector glass to the solar radiation.
б	Stefan-Boltzman constant(W/m^2K^4)